Antipodal Receptions in Global Acoustics

J Courtney

Thesis Presented for the Degree of
DOCTOR OF PHILOSOPHY
in the Department of Oceanography
UNIVERSITY OF CAPE TOWN
August 1997

Acknowledgements

- I would like to thank my supervisor, Geoff Brundrit, for his help with this thesis and his concurrent 'life skills training' particularly with regard to parallel parking - I am and many others are eternally grateful.
- I have to thank my husband, Shaun, for his faith in me, for enduring this time and not letting me give up, no matter how convincingly I pleaded.
- Lastly, I am indebted to our baby: 'Piccolino I', for sticking to a schedule and keeping me motivated to finish this work before his/her appearance in September 1997.

Contents

List of Figures

List of Tables

Chapter 1

Introduction

Global Acoustic Propagation is a recently developed scientific discipline within the study of long range underwater acoustic propagation. Acoustic propagation over extremely long ranges involves a combination of effects from earth curvature and the global distribution of oceanographic and geophysical features. Antipodal receptions, that is to ranges of the order of $20Mm$ ($1\ Megameter\ =\ 1\,000\ km$), require underwater acoustic propagation to very long ranges and thus effects due to the form of the earth and the range dependence of the sound speed field within the ocean can not be ignored. The purpose of this thesis is to investigate the nature of antipodal receptions with reference to the form of the earth and horizontal sound speed variations within the ocean and thereby contribute to the new and specialized field of study, Global Acoustic Propagation.

Close to an acoustic source acoustic energy diverges so that local signal strengths decrease with distance from the source. However, as the antipodal region is approached acoustic energy that has not been blocked by bathymetric features will refocus, counteracting the distance loss rule. Thus at antipodal sites there is a good prospect of receiving a focused signal. Even so, the ellipsoidal form of the earth and the horizontal variability within the sound speed field of the ocean means that the re-focusing will result in a region of enhanced signal rather than an exact antipodal point. The precise detail of the advantage of placing receivers in the antipodal region will depend upon the paths taken by the acoustic energy and the characteristics of the acoustic medium encountered along each path.

The proposal for this thesis is to develop an algorithm to determine the nature of the antipodal region under certain physical assumptions. The physical assumptions are referred to as the geometric assumption, which refers to the form of the earth, and the refractive assumption, which refers to the horizontal variability of sound speed within the world oceans.

Now that the principle objective of this thesis is stated it is appropriate to include a brief overview of this thesis, indicating how the objective is achieved and what conclusions are made.

The historical review of Chapter 1 indicates that the two principal factors effecting antipodal receptions are the form of the earth and the horizontal sound speed variability within the ocean. These two effects are considered in Chapter 2 and are referred to as the geometric and refractive assumptions. The geometric assumption corresponds to a spheroidal earth with a range independent sound speed environment, while the refractive assumption refers to a range dependent sound speed environment on a spherical earth. The range dependent sound speed environment is considered in the form of a sound slowness model varying with latitude.

Longuet-Higgins (1990) determined the antipodal region with regard to a spheroidal earth using geometric techniques. In Chapters 3; 4 and 5 the generalized antipodal algorithm is determined in an analytical way, using the methodology of Longuet-Higgins (1990).

In each of the stages of development of the algorithm results associated with the geometric assumption are consistent with those of Longuet-Higgins (1990) and thus verify the antipodal algorithm.

Finally in Chapter 6 the antipodal algorithm is presented in full and theoretical applications to the algorithm are considered. A scale analysis is performed between the antipodal regions under both the geometric and refractive assumptions. In fact, the magnitude of the antipodal region under the refractive assumption is close to ten times that of the antipodal region under the geometric assumption. Finally a case study regarding the Pioneer Seamount source is considered, and the antipodal region is determined under the dominant refractive assumption.

1.1 Historical Review and Motivation

In this section a historical review of previous works regarding antipodal transmissions in underwater acoustics is presented for two reasons: firstly to provide the motivation for this thesis and secondly to place the reader within the context of this topic. Underwater acoustic propagation over very large distances, particularly to antipodal ranges, is a new development in the science of underwater acoustics, consequently very little is available from the literature. Munk, Worcester, and Wunsch (1995) provided "A Brief Historical Review" regarding long range underwater acoustic transmission experiments, in their section 8.3. Because of the limited material available, with reference to underwater antipodal receptions, brief references are made to antipodal receptions in other geophysical disciplines, namely air pressure, radio waves and seismic waves.

Perhaps the first recorded very long range observation in geoscience was on 26 August 1883, when the Krakatau volcano, which is situated in the Sunda Strait between the islands of Java and Sumatra, erupted and nearly destroyed itself in the process. The eruption and collapse produced one of the largest explosions ever recorded on earth. The blast circumnavigated the globe at least three times in air pressure waves which were recorded on barometers worldwide (Simkin and Fiske 1983).

The first suggestion that waves propagating on a spherical earth converge at an antipode was by Marconi in 1922 (Munk, Worcester, and Wunsch 1995), with reference to radio waves in the atmosphere. Gerson, Hengen, Pipp, and Webster (1969) tested the Marconi hypothesis between Perth and Bermuda in 1969, using high frequency radio waves. Interestingly enough, these authors confirmed that receptions at the antipode were superior to two other received signals, which were both closer to the receiver by about 1 700 km. Thus they verified Marconi's theory of antipodal focusing of radio waves.

The discovery of the SOFAR channel by Ewing and Worzel (1948) initiated the study of underwater acoustic propagation to antipodal ranges. The SOFAR channel is a function of the sound speed minimum, which is typically at a depth of 1 000 m below the ocean surface. Sound refracts, according to Snell's law, towards regions of lower sound speed, thus the sound speed minimum acts as a waveguide and sound propagating above or below it is continuously bent towards the minimum. This feature

of the sound speed structure within the ocean enables sound propagation to extremely long ranges to occur, without the high energy losses associated with bottom and surface interactions. The nature of underwater sound propagation about the depth of the sound speed minimum is referred to as axial propagation or SOFAR channel propagation.

Throughout the ocean, in both the vertical and horizontal planes there exists a high degree of variability within the sound speed field. A typical localized study, such as the effects of oceanic features on sound propagation through them would be to consider the refraction to the ray in both the vertical and horizontal plane, both would be important components and necessary to the understanding of the acoustic properties of the particular feature.

In this study the concern is with long range, in fact global, underwater acoustics. There is a distinct geometrical advantage to studying global underwater acoustics, in that the ocean is a thin sharply bounded waveguide, with a thickness of $< \frac{1}{1000}$ of the earth's radius. In this context 'local studies' would refer to sound speed variations in the vertical plane and 'global studies' refer to sound speed variability in the horizontal plane (Dworski and Mercer 1990).

Long range underwater sound propagation is necessarily low-frequency, since the volume absorption of acoustic waves in sea water increases rapidly above $1\ 000\ Hz$. For low frequency sound, $< 100\ Hz$, the absorption coefficient is small enough that for uninterrupted paths, underwater sound propagation over very long ranges appears to certainly be feasible. (Shockley, Northrop, Hansen, and Hartdegen 1982).

In their paper entitled "Long Range Sound Transmission", Ewing and Worzel (1948) described a number of experiments used to demonstrate long range underwater acoustic propagation using the SOFAR waveguide. They proposed that as sound travels from the source a certain amount of energy is lost due to geometrical spreading:

$$Total\ energy\ lost\ per\ unit\ square = (distance\ from\ the\ source)^{-1}.$$

However, at global ranges greater than one quarter of the earths circumference there is a convergence of great circle sound paths as they approach the antipodes, suggesting a refocusing of acoustic energy.

Ewing and Worzel (1948) reasoned that long range SOFAR transmissions, of the order of at least $10\ 000$ Nautical miles, are feasible. Over the following two decades demonstrations at ever increasing ranges were performed but these were mainly cited in classified literature. Those that were publicized have been profiled in the Munk, Worcester, and Wunsch (1995) review. The early experiments were limited to explosive shot tests that were, by their very nature, unrepeatable and thus comparative studies are not possible.

The remarkable long range underwater sound transmission properties of the ocean were only truly verified in the March of 1960, when a noteworthy global range underwater sound transmission experiment, between Perth and Bermuda, was performed using an explosive source. This experiment was inspired, not only by the Ewing and Worzel (1948) paper, but other basin scale experiments described in the Munk, Worcester, and Wunsch (1995) review. One hundred and fifty kilograms of TNT were detonated off the coast of Perth, Australia, and the signal was received clearly by axial hydrophones off Bermuda, U.S.A. This incredible 'first' very long or global range underwater acoustic experiment was very close to antipodal, the range was in fact 178.2^o, where an antipodal range is 180^o.

The Perth-Bermuda experiment was initially noted in the 'Notes and Personalia of the Transactions of the American Geophysical Union' (1960, p670) (Munk, O'Reilly, and Reid 1988). However, this documentation was not available to the general public. Nevertheless, the contribution of this experiment to the science of underwater acoustics was recognized much later when Shockley, Northrop, Hansen, and Hartdegen (1982) provided the first public description of the experiment in the Journal of the Acoustical Society of America. Munk, O'Reilly, and Reid (1988) reconsidered the experiment in more detail, particularly with regard to underwater sound propagation to global ranges. Heaney, Kuperman, and McDonald (1991) provided the final explanation for previously unexplained results regarding the Perth-Bermuda experiment.

Shockley, Northrop, Hansen, and Hartdegen (1982) ignored the effects of the form of the earth and horizontal refraction, they analyzed the variation in the sound speed medium between Perth and Bermuda. In order to achieve this they identified the signal speed of the axial ray path, where the signal speed was defined as the great circle distance between source and receiver, divided by the travel time of the sound ray propagating along the sound speed minimum.

The great circle distance between two points on the surface of the sphere is defined as the shorter arc of the great circle joining the two points, where the great circle is described as the circle on the surface of the sphere whose plane passes through the center of the sphere (Parker 1994). In the context of this thesis the great circle is, at best, a first approximation to the axial propagation path for sound transmission through the world oceans.

Shockley, Northrop, Hansen, and Hartdegen (1982) were concerned that sound propagating, along the great circle path, to antipodal ranges will propagate through a number of oceanographic regions, each with a particular sound speed structure. In fact these authors raised an important problem associated with very long range underwater sound propagation experiments: notably that it is inevitable that sound propagating to such large ranges encounters not only a number of distinct water masses, but other oceanographic features such as fronts, currents and mesoscale eddies.

Oceanic features, such as these, have an environment which contrasts significantly from the background ocean. These sharp gradients indicate that these features affect the sound speed field and thus the propagation path through the sound speed field significantly. The variation in the sound speed field along the range of the propagation path provides one explanation as to why the great-circle path is at best only a first approximation to the actual path that the sound will travel.

Munk, O'Reilly, and Reid (1988) also determined that the great circle path was at best an approximation to the actual axial path and that not only is a correction due to the horizontal sound speed variability within the ocean necessary, but a correction due to the non-spherical form of the earth. These authors concluded that the form of the earth can not be ignored for antipodal ranges, and that a more realistic topology than the sphere is that of an oblate ellipsoid, which takes into account the earth flattening of the poles and the equatorial bulge.

Munk, O'Reilly, and Reid (1988) used the ray tracing technique, which is outlined in Section 1.2, to correct the great circle ray paths of Shockley, Northrop, Hansen, and Hartdegen (1982) for the non-sphericity of the ray paths, and considered sound propagation on the surface of an earth ellipsoid. The shortest distance between two points on the surface of an ellipsoid is that of a geodesic. The

Antipodal Receptions in Global Acoustics

J Courtney

Thesis Presented for the Degree of
DOCTOR OF PHILOSOPHY
in the Department of Oceanography
UNIVERSITY OF CAPE TOWN
August 1997

Abstract

Recent global range propagation studies in the new scientific discipline of long range underwater acoustics have led to enquiries regarding the nature of antipodal receptions. The purpose of this study is to develop an algorithm to determine the nature and characteristics of the antipodal region in global range studies. Acoustic propagation over very long ranges involves a combination of effects such as the form of the earth and the global structure of the acoustic medium, namely the ocean.

The generalized antipodal algorithm is developed using analytical techniques and two model assumptions are used to demonstrate the algorithm. Firstly a geometric assumption is considered, this refers to a spheroidal earth with a range independent sound speed environment. Secondly a refractive assumption is considered, this refers to a range dependent environment on a spherical earth. The range dependent environment was included in the form of a sound slowness function of latitude.

A scale analysis indicated that of the two effects considered the refractive effect produces an antipodal region close to ten times the size of the antipodal region under the geometric assumption. This demonstrates clearly that latitudinal refraction dominates the effects due to the form of the earth on antipodal receptions.

An important factor regarding the derived antipodal algorithm is the generalized form of the algorithm which indicates that an extension to more realistic scenarios could be considered.

Acknowledgements

- I would like to thank my supervisor, Geoff Brundrit, for his help with this thesis and his concurrent 'life skills training' particularly with regard to parallel parking - I am and many others are eternally grateful.
- I have to thank my husband, Shaun, for his faith in me, for enduring this time and not letting me give up, no matter how convincingly I pleaded.
- Lastly, I am indebted to our baby: 'Piccolino I', for sticking to a schedule and keeping me motivated to finish this work before his/her appearance in September 1997.

Contents

List of Figures

List of Tables

Chapter 1

Introduction

Global Acoustic Propagation is a recently developed scientific discipline within the study of long range underwater acoustic propagation. Acoustic propagation over extremely long ranges involves a combination of effects from earth curvature and the global distribution of oceanographic and geophysical features. Antipodal receptions, that is to ranges of the order of $20Mm$ ($1\ Megameter\ =\ 1\,000\ km$), require underwater acoustic propagation to very long ranges and thus effects due to the form of the earth and the range dependence of the sound speed field within the ocean can not be ignored. The purpose of this thesis is to investigate the nature of antipodal receptions with reference to the form of the earth and horizontal sound speed variations within the ocean and thereby contribute to the new and specialized field of study, Global Acoustic Propagation.

Close to an acoustic source acoustic energy diverges so that local signal strengths decrease with distance from the source. However, as the antipodal region is approached acoustic energy that has not been blocked by bathymetric features will refocus, counteracting the distance loss rule. Thus at antipodal sites there is a good prospect of receiving a focused signal. Even so, the ellipsoidal form of the earth and the horizontal variability within the sound speed field of the ocean means that the re-focusing will result in a region of enhanced signal rather than an exact antipodal point. The precise detail of the advantage of placing receivers in the antipodal region will depend upon the paths taken by the acoustic energy and the characteristics of the acoustic medium encountered along each path.

The proposal for this thesis is to develop an algorithm to determine the nature of the antipodal region under certain physical assumptions. The physical assumptions are referred to as the geometric assumption, which refers to the form of the earth, and the refractive assumption, which refers to the horizontal variability of sound speed within the world oceans.

Now that the principle objective of this thesis is stated it is appropriate to include a brief overview of this thesis, indicating how the objective is achieved and what conclusions are made.

The historical review of Chapter 1 indicates that the two principal factors effecting antipodal receptions are the form of the earth and the horizontal sound speed variability within the ocean. These two effects are considered in Chapter 2 and are referred to as the geometric and refractive assumptions. The geometric assumption corresponds to a spheroidal earth with a range independent sound speed environment, while the refractive assumption refers to a range dependent sound speed environment on a spherical earth. The range dependent sound speed environment is considered in the form of a sound slowness model varying with latitude.

Longuet-Higgins (1990) determined the antipodal region with regard to a spheroidal earth using geometric techniques. In Chapters 3; 4 and 5 the generalized antipodal algorithm is determined in an analytical way, using the methodology of Longuet-Higgins (1990).

In each of the stages of development of the algorithm results associated with the geometric assumption are consistent with those of Longuet-Higgins (1990) and thus verify the antipodal algorithm.

Finally in Chapter 6 the antipodal algorithm is presented in full and theoretical applications to the algorithm are considered. A scale analysis is performed between the antipodal regions under both the geometric and refractive assumptions. In fact, the magnitude of the antipodal region under the refractive assumption is close to ten times that of the antipodal region under the geometric assumption. Finally a case study regarding the Pioneer Seamount source is considered, and the antipodal region is determined under the dominant refractive assumption.

1.1 Historical Review and Motivation

In this section a historical review of previous works regarding antipodal transmissions in underwater acoustics is presented for two reasons: firstly to provide the motivation for this thesis and secondly to place the reader within the context of this topic. Underwater acoustic propagation over very large distances, particularly to antipodal ranges, is a new development in the science of underwater acoustics, consequently very little is available from the literature. Munk, Worcester, and Wunsch (1995) provided "A Brief Historical Review" regarding long range underwater acoustic transmission experiments, in their section 8.3. Because of the limited material available, with reference to underwater antipodal receptions, brief references are made to antipodal receptions in other geophysical disciplines, namely air pressure, radio waves and seismic waves.

Perhaps the first recorded very long range observation in geoscience was on 26 August 1883, when the Krakatau volcano, which is situated in the Sunda Strait between the islands of Java and Sumatra, erupted and nearly destroyed itself in the process. The eruption and collapse produced one of the largest explosions ever recorded on earth. The blast circumnavigated the globe at least three times in air pressure waves which were recorded on barometers worldwide (Simkin and Fiske 1983).

The first suggestion that waves propagating on a spherical earth converge at an antipode was by Marconi in 1922 (Munk, Worcester, and Wunsch 1995), with reference to radio waves in the atmosphere. Gerson, Hengen, Pipp, and Webster (1969) tested the Marconi hypothesis between Perth and Bermuda in 1969, using high frequency radio waves. Interestingly enough, these authors confirmed that receptions at the antipode were superior to two other received signals, which were both closer to the receiver by about $1\ 700\ km$. Thus they verified Marconi's theory of antipodal focusing of radio waves.

The discovery of the SOFAR channel by Ewing and Worzel (1948) initiated the study of underwater acoustic propagation to antipodal ranges. The SOFAR channel is a function of the sound speed minimum, which is typically at a depth of $1\ 000\ m$ below the ocean surface. Sound refracts, according to Snell's law, towards regions of lower sound speed, thus the sound speed minimum acts as a waveguide and sound propagating above or below it is continuously bent towards the minimum. This feature

of the sound speed structure within the ocean enables sound propagation to extremely long ranges to occur, without the high energy losses associated with bottom and surface interactions. The nature of underwater sound propagation about the depth of the sound speed minimum is referred to as axial propagation or SOFAR channel propagation.

Throughout the ocean, in both the vertical and horizontal planes there exists a high degree of variability within the sound speed field. A typical localized study, such as the effects of oceanic features on sound propagation through them would be to consider the refraction to the ray in both the vertical and horizontal plane, both would be important components and necessary to the understanding of the acoustic properties of the particular feature.

In this study the concern is with long range, in fact global, underwater acoustics. There is a distinct geometrical advantage to studying global underwater acoustics, in that the ocean is a thin sharply bounded waveguide, with a thickness of $< \frac{1}{1000}$ of the earth's radius. In this context 'local studies' would refer to sound speed variations in the vertical plane and 'global studies' refer to sound speed variability in the horizontal plane (Dworski and Mercer 1990).

Long range underwater sound propagation is necessarily low-frequency, since the volume absorption of acoustic waves in sea water increases rapidly above $1\ 000\ Hz$. For low frequency sound, $< 100\ Hz$, the absorption coefficient is small enough that for uninterrupted paths, underwater sound propagation over very long ranges appears to certainly be feasible. (Shockley, Northrop, Hansen, and Hartdegen 1982).

In their paper entitled "Long Range Sound Transmission", Ewing and Worzel (1948) described a number of experiments used to demonstrate long range underwater acoustic propagation using the SOFAR waveguide. They proposed that as sound travels from the source a certain amount of energy is lost due to geometrical spreading:

$$Total\ energy\ lost\ per\ unit\ square = (distance\ from\ the\ source)^{-1}.$$

However, at global ranges greater than one quarter of the earths circumference there is a convergence of great circle sound paths as they approach the antipodes, suggesting a refocusing of acoustic energy.

Ewing and Worzel (1948) reasoned that long range SOFAR transmissions, of the order of at least 10 000 Nautical miles, are feasible. Over the following two decades demonstrations at ever increasing ranges were performed but these were mainly cited in classified literature. Those that were publicized have been profiled in the Munk, Worcester, and Wunsch (1995) review. The early experiments were limited to explosive shot tests that were, by their very nature, unrepeatable and thus comparative studies are not possible.

The remarkable long range underwater sound transmission properties of the ocean were only truly verified in the March of 1960, when a noteworthy global range underwater sound transmission experiment, between Perth and Bermuda, was performed using an explosive source. This experiment was inspired, not only by the Ewing and Worzel (1948) paper, but other basin scale experiments described in the Munk, Worcester, and Wunsch (1995) review. One hundred and fifty kilograms of TNT were detonated off the coast of Perth, Australia, and the signal was received clearly by axial hydrophones off Bermuda, U.S.A. This incredible 'first' very long or global range underwater acoustic experiment was very close to antipodal, the range was in fact 178.2^o, where an antipodal range is 180^o.

The Perth-Bermuda experiment was initially noted in the 'Notes and Personalia of the Transactions of the American Geophysical Union' (1960, p670) (Munk, O'Reilly, and Reid 1988). However, this documentation was not available to the general public. Nevertheless, the contribution of this experiment to the science of underwater acoustics was recognized much later when Shockley, Northrop, Hansen, and Hartdegen (1982) provided the first public description of the experiment in the Journal of the Acoustical Society of America. Munk, O'Reilly, and Reid (1988) reconsidered the experiment in more detail, particularly with regard to underwater sound propagation to global ranges. Heaney, Kuperman, and McDonald (1991) provided the final explanation for previously unexplained results regarding the Perth-Bermuda experiment.

Shockley, Northrop, Hansen, and Hartdegen (1982) ignored the effects of the form of the earth and horizontal refraction, they analyzed the variation in the sound speed medium between Perth and Bermuda. In order to achieve this they identified the signal speed of the axial ray path, where the signal speed was defined as the great circle distance between source and receiver, divided by the travel time of the sound ray propagating along the sound speed minimum.

The great circle distance between two points on the surface of the sphere is defined as the shorter arc of the great circle joining the two points, where the great circle is described as the circle on the surface of the sphere whose plane passes through the center of the sphere (Parker 1994). In the context of this thesis the great circle is, at best, a first approximation to the axial propagation path for sound transmission through the world oceans.

Shockley, Northrop, Hansen, and Hartdegen (1982) were concerned that sound propagating, along the great circle path, to antipodal ranges will propagate through a number of oceanographic regions, each with a particular sound speed structure. In fact these authors raised an important problem associated with very long range underwater sound propagation experiments: notably that it is inevitable that sound propagating to such large ranges encounters not only a number of distinct water masses, but other oceanographic features such as fronts, currents and mesoscale eddies.

Oceanic features, such as these, have an environment which contrasts significantly from the background ocean. These sharp gradients indicate that these features affect the sound speed field and thus the propagation path through the sound speed field significantly. The variation in the sound speed field along the range of the propagation path provides one explanation as to why the great-circle path is at best only a first approximation to the actual path that the sound will travel.

Munk, O'Reilly, and Reid (1988) also determined that the great circle path was at best an approximation to the actual axial path and that not only is a correction due to the horizontal sound speed variability within the ocean necessary, but a correction due to the non-spherical form of the earth. These authors concluded that the form of the earth can not be ignored for antipodal ranges, and that a more realistic topology than the sphere is that of an oblate ellipsoid, which takes into account the earth flattening of the poles and the equatorial bulge.

Munk, O'Reilly, and Reid (1988) used the ray tracing technique, which is outlined in Section 1.2, to correct the great circle ray paths of Shockley, Northrop, Hansen, and Hartdegen (1982) for the non-sphericity of the ray paths, and considered sound propagation on the surface of an earth ellipsoid. The shortest distance between two points on the surface of an ellipsoid is that of a geodesic. The

non-spherical form of the earth displaced the ray path further south than the great circle path. Clearly the geodesic is the appropriate path if the sound speed environment is uniform, but there are significant differences in propagation paths between warm equatorial waters and cold polar waters. Munk, O'Reilly, and Reid (1988) considered the effects on the axial path due to the mean horizontal sound speed gradients. This path which they referred to as the refracted geodesic path was displaced significantly further north of the original great circle path. The differences between the axial path for the great circle, the geodesic and the refracted geodesic are shown below in Figure 1.1. They noted that there is no axially refracted geodesic path between Perth and Bermuda, because of the bathymetric blocking of Africa.

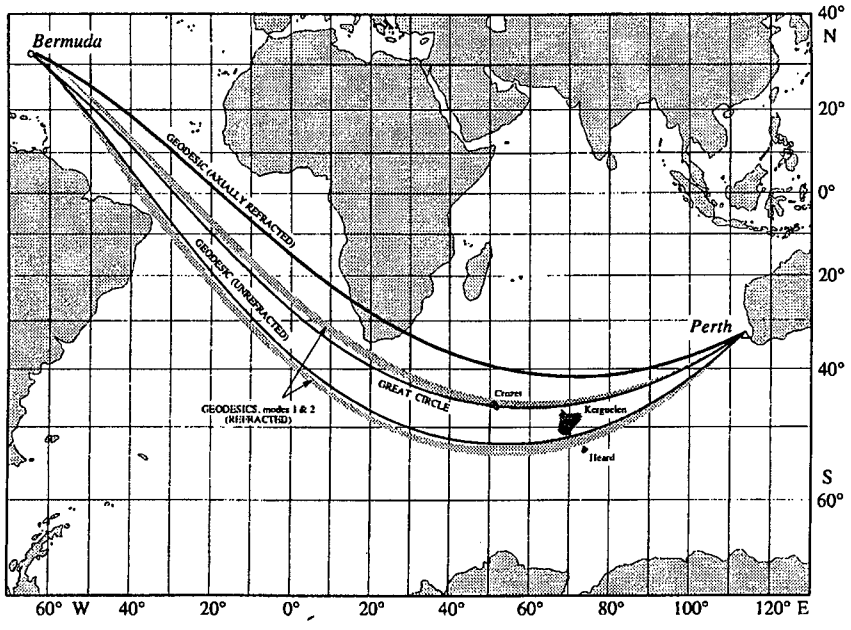

Figure 1.1: This figure was taken from Munk, Worcester and Wunsch (1995). It clearly demonstrates the different propagation paths used in the interpretation of the Perth-Bermuda 1960 experiment results. Firstly, the great circle path, used by Shockley, Northrop, Hansen and Hartdegen (1982); secondly, the geodesic and refracted geodesic paths determined by Munk, O'Reilly and Reid (1988); and finally, the two shaded paths represent the normal mode paths developed by Heaney, Kuperman and McDonald (1991).

The range of the great circle path between Perth and Bermuda was shown to be 19 822.1 km, while that of the geodesic was slightly shorter at 19 820 km. While the geodesic path is shorter it does extend significantly further south of the great circle path, into the cold waters of the Southern Ocean. The cold southern waters affect the travel time of the axial sound ray, retarding it, since sound propagates more slowly through cooler waters. Thus when lateral sound speed gradients are considered the appropriate shortest path is no longer that of minimum range, but rather minimum travel time.

The authors, Munk, O'Reilly, and Reid (1988), attempted to include variation in horizontal sound speed in two ways. Firstly, they included the variability as a simplified one-dimensional function of latitude only. They concluded, however, that a one-dimensional approach was invalid because of the

large oceanographic differences between the Indian and the Atlantic oceans. Secondly, they modeled the horizontal variability as a continuous function of latitude and longitude, by extrapolating (unrealistically) across the African sub-continent, between the Atlantic and Indian Ocean sound speed values. The new refracted path was also blocked by Africa, in fact the path nearest to the continent, that was not blocked by the continent, was predicted to pass 300 km south of Bermuda. The authors suggested that the receptions at Bermuda were the results of indirect paths, which had perhaps grazed the coast of Brazil.

Munk, O'Reilly, and Reid (1988) summarized the effects of lateral sound speed variation and the ellipsoidal form of the earth as follows:

- The appropriate geodesic path curves significantly further south of the great circle path because of the shorter earth radius at the poles.
- The lateral sound speed variation results in the path being refracted northwards away from the cold southern waters.

They concluded that while the effects of earth flattening on the path of the axial sound ray can not be ignored, the effects of lateral variation in the sound speed field dominate these effects.

Heaney, Kuperman, and McDonald (1991) used normal mode theory, which is outlined in Section 1.2, with realistic acoustic and bathymetric data bases to search for viable paths from Perth to Bermuda. These authors derived the ray equations on a generalized curved surface without reference to the perturbation analysis that Munk, O'Reilly, and Reid (1988) used, and they were able to include horizontal refraction due to variations in the modal structure of the ocean waveguide. Heaney, Kuperman, and McDonald (1991) then applied their equations to an ellipsoidal earth form and arrived at equations almost identical to those of Munk, O'Reilly, and Reid (1988). The difference between the two methods was with the use of arc-length rather than phase-velocity based time variables to parameterize the ray paths.

A distinct feature of the 1960 Perth-Bermuda Experiment was the two pulsed arrival pattern of the received signal. Shockley, Northrop, Hansen, and Hartdegen (1982) suggested that this was a multipath problem. Munk, O'Reilly, and Reid (1988) hypothesized that the second arrival was due to an indirect path grazing Brazil or an echo from Bermuda, however their numerical results did not correspond well to the observed experimental results. The normal mode methods used by Heaney, Kuperman, and McDonald (1991) resulted in several viable paths that agreed with the experimental results, they put forward that the double arrival structure was due to two widely separated propagation paths, one just south of Africa and the other close to the coast of Brazil, between Perth and Bermuda. These paths are shown in Figure 1.1, as the shaded paths.

After reconsidering the 1960 experiment Walter Munk and Andrew Forbes suggested that the long range sound propagation properties of the ocean could be used as a measure of global temperature trends (Munk and Forbes 1989). They proposed the Heard Island Feasibility Test (HIFT), which was internationally supported and took place during the early part of 1991. The principal goal of HIFT was to determine the efficiency of the SOFAR channel throughout the worlds oceans.

Previous to HIFT, and in response to Munk and Forbes (1989), Dworski and Mercer (1990) considered bathymetrically viable propagation paths, from Heard Island to the west and east coast of the United States, analytically. These bathymetric "windows of opportunity" have been shown below in

Figure 1.2. The main purpose of their study was to develop modeling software that would not only aid in the preparation for HIFT, but in the interpretation of HIFT results. The authors determined that, certainly, an antipodal geometry exists for underwater paths on earth, but that it would probably only be realizable between the South Indian and the North Atlantic Oceans.

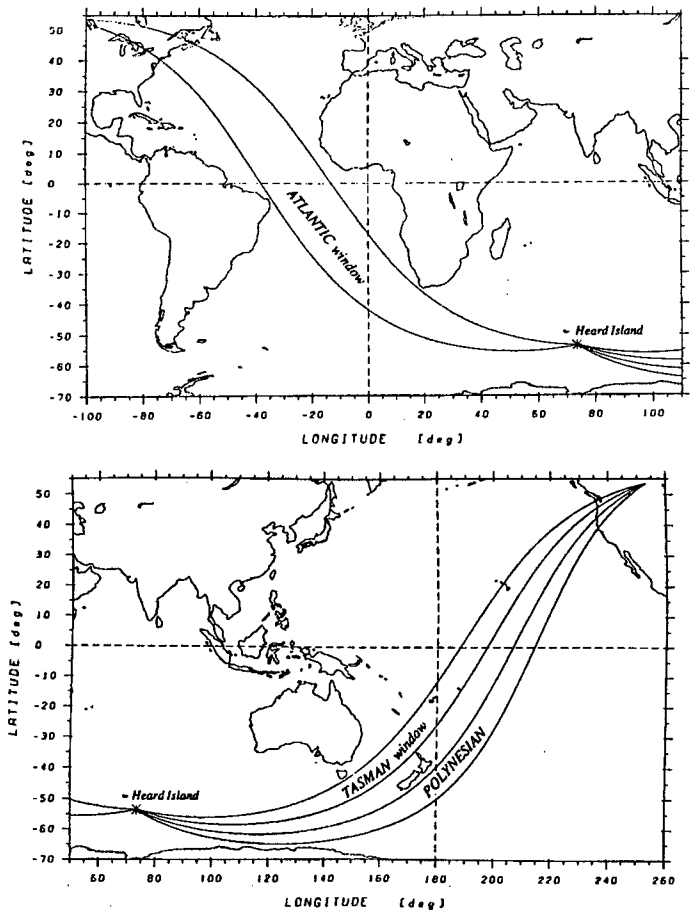

Figure 1.2: Geodesics bounding the westward Atlantic bathymetric window and the eastward Tasman and Polynesian bathymetric windows, from Heard Island (Dworski and Mercer 1990).

In early 1991 a source ship, the R/V Cory Chouest, was stationed off Heard Island in the Southern Ocean and a low frequency sound signal was transmitted over a period of 5 days. The transmitter site was specifically chosen, because it acoustically illuminates much of the worlds oceans. HIFT was considered to be a great success in that coherent acoustic signals were easily detected at very long ranges, up to 18 Mm, so that travel times were accurately determined. Figure 1.3, below, shows the paths between the source and the sixteen successful receiver sites world wide.

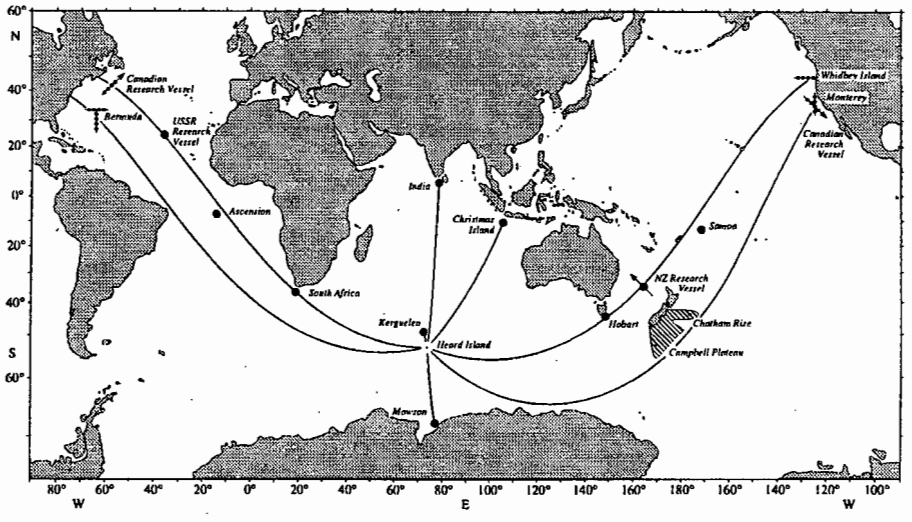

Figure 1.3: Ray paths between the source, close to Heard island, and 16 successful receiver sites worldwide, the vertical and horizontal lines represent vertical and horizontal receiver arrays, respectively (Munk, Spindel, Baggeroer and Birdsall (1994)).

For a complete report and review regarding HIFT the October 1994 Special Issue of the Journal of the Acoustic Society of America consisted of a series of papers referring to the experiment. The first paper of that issue, by Munk, Spindel, Baggeroer, and Birdsall, provided a complete overview of the experiment.

Returning to the principal theme of this thesis, antipodal receptions in global underwater acoustics, as a result of HIFT, Birdsall, Metzger, and Dzieciuch (1994) concluded that at very long ranges there was no fall off in intensity of the received signal. This in itself provides a hint that the refocusing is occurring and is as hypothesized counteracting the geometrical spreading loss experienced at ranges less than a quarter of the earths circumference. In fact Baggeroer, Sperry, Lashkari, Chiu, Miller, Mikhalvsky, and von der Heydt (1994), who considered the 17 Mm range path from Heard Island to Monterey (California), confirmed that antipodal receptions were more complicated than they had anticipated. They advised that substantial investigations regarding antipodal receptions, for future experiments involving such long range propagation, should be carried out.

The previous paragraph concludes the observational studies that have taken place with regard to underwater antipodal receptions. However there is a certain analogy between classical seismology texts and the determination of the antipodal region using underwater acoustics. In seismology, properties of the earths crust are inferred from travel time observations of earthquake waves. The classical seismology texts make a point of referencing relevant material in purely geometrical texts that dwell on the theoretical aspects and nature of the antipodal region. These are discussed below, firstly for historical interest and secondly to introduce terminology that becomes pertinent to the remainder of this thesis.

The antipode to a source on a spherical earth has a simple definition as that point which is diametrically opposite to the source (Parker 1994). This is the point where all the great circles converge. On a non-spherical earth, determination of the antipode is more complex. A geodetic approach is

needed in which the antipode is defined as the region on the far side of the earth where the geodesics refocus. Except for the sphere, there is not one single point in the antipodal region common to all geodesics from the source (Do Carmo 1976).

In these cases use can be made of differential geometry texts (for example Do Carmo (1976) and Koenderink (1990)). The minimum distance path between two points on a general surface is defined as a geodesic. On a sphere the geodesics converge to the antipodal point; also referred to as the conjugate point. For other surfaces the geodesics converge into a specific arrival pattern of overlapping geodesics, which is referred to as the conjugate locus in differential geometry and the caustics in acoustics.

In terms of underwater acoustics to very long ranges there are two types of path to consider, firstly minimum distance paths for constant sound speed environments, which are referred to as geodesics, and secondly minimum travel time paths for variable sound speed environments, which are referred to as refracted geodesics. Consequently, whether one is considering long range sound propagation with regard to the form of the earth or with regard to horizontal sound speed variations, the caustic refers to the envelope of ray paths.

As Munk, O'Reilly, and Reid (1988) suggested, a more realistic form of the earth is that of an ellipsoid. In 1882 A. Braunmuhl proved that the conjugate locus of a generalized ellipsoid was a four-cusped hypocycloid (Do Carmo 1976). Longuet-Higgins (1990) investigated the nature of the antipodal region on a slightly oblate form, with parameters relating to the earth. He found that indeed the antipodal region was a four-cusped hypocycloid centered on the geographical antipodal point. The sides of the hypocycloid represents the caustic curve, which separate the antipodal region from the remainder of the globe. The major axis of the hypocycloid are aligned with a north–south and west–east orientation. The size of the hypocycloid is dependent on the ellipticity of the earth ellipsoid and the latitude of the source.

Longuet-Higgins (1990) extended his geometrical theory beyond those of antipodal receptions, he continued to hypothesize that while geodesics circling the globe to half a circumference yield a four-cusped hypocycloid at the antipode, geodesics propagating yet another half a circumference yield a four-cusped hypocycloid caustic at the source, only this caustic is twice the size of the one at the antipode. Continuing in this way, the caustic curve that is generated by geodesics that travel three half circumferences again generates a four-cusped hypocycloid, this hypocycloid is three times the size of the original caustic and centered on the antipode.

A number of curves arise throughout this study, which are named in classical geometry texts, for example Lockwood (1961). Full references and details are provided as the curves arise in the text.

This thesis builds upon the understanding gained from earlier studies of the geodesics of an oblate spheroidal earth, in particular Longuet-Higgins (1990). It uses a similar methodology to investigate the consequences of horizontal refraction. The variation in sound speed is assumed to be latitudinal and a particular model form is used for illustration. Only axial or SOFAR propagation is considered. Heaney, Kuperman, and McDonald (1991) showed that higher modes may need to be considered in particular situations. The extension of the method to such cases is addressed in the final discussion.

Thus the study of antipodal receptions is made in two relatively realistic environments. The shape of the earth is taken into account and a start is made towards incorporating realistic horizontal refrac-

tion. A comparison of the effects of these two environments on antipodal receptions is made.

The "bathymetric assumption" is also made. Large topographic features interfere with the leading edge of a sound signal (Bryan, Truchan, and Ewing 1963). However as long as the topographic feature does not extend upwards into the sound channel axis the axial contribution to the received signal remains unchanged. Large land masses such as continents result in the blocking and shoaling of sound rays. The interference that topographic features present to antipodal receptions is not addressed in this thesis.

1.2 Necessary Acoustical Theory

In this section the necessary background with regard to global range acoustic propagation studies is introduced. In order to introduce the ideas and techniques necessary for this study, this section begins by describing the ocean as an acoustic medium. This is followed by an introduction to two commonly used modeling techniques, namely: ray tracing and normal mode theory. Both of these techniques are then described in terms of axial propagation which is essential to analytical global range propagation studies. Another useful parameter, defined as the Action, is also introduced, because it provides a link between ray tracing and normal mode theory.

The equation of state for sea water specifies that every physical quantity in the ocean can be related to the three fundamental state variables. For oceanographic studies the fundamental state variables are typically temperature, salinity and pressure. For acoustic oceanographic studies potential temperature (or entropy), salinity and pressure are preferred. Thus

$$\rho = \rho(\eta, Sa, p).$$

Where:
ρ = density
η = potential temperature
Sa = salinity
p = pressure

Sound speed in the ocean, C, is a physical quantity and is therefore, through the equation of state, a function of potential temperature, salinity and pressure. The relationship between sound speed and density is easily derived to be (Urick 1982):

$$\frac{1}{C^2} = (\frac{\partial \rho}{\partial p})_{\eta,Sa}$$

Changes in temperature, salinity and pressure are reflected by relative variations in the sound speed. Thus a positive (or negative) variation in any of the state variables results in an increase (or decrease) in the sound speed.

It is important to notice that actual variations in sound speed, compared to its magnitude, which is typically 1500 $m.s^{-1}$, are small. For example, in a vertical sound speed profile the total sound speed variation is usually within 30 $m.s^{-1}$, which is only 2% of the typical sound speed value. Even though the sound speed variation is small it does have large effects on sound propagation in the ocean. Temperature changes usually dominate salinity changes in their contribution to sound speed variations

(Munk, Worcester, and Wunsch 1995). A guideline to variations in sound speed due to changes in temperature is that sound speed in the ocean increases by $4 - 5m.s^{-1}per^{o}C$ (Baggeroer and Munk 1992).

An important factor in the study of long range underwater sound propagation is that the ocean displays a high degree of stratification with depth in the thermal structure and thus in the sound speed structure. Etter (1991) described fully the relationship between temperature layers and their corresponding acoustic layers, an outline has been provided here.

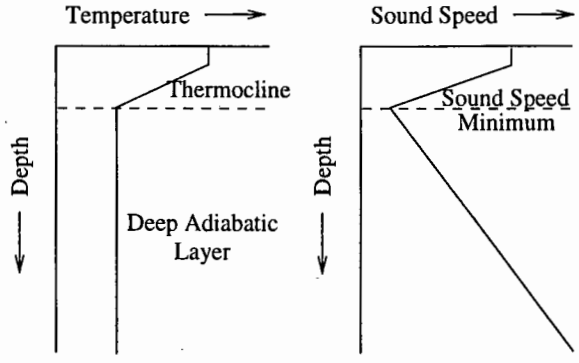

Figure 1.4: Schematic relationship between temperature and sound speed profiles in the ocean, adapted from Etter (1991).

The range of the vertical temperature profile in the ocean consists of a number of recognizable layers, refer to Figure 1.4

- The Surface Layer, which is usually associated with a well mixed layer of isothermal water. In this thesis the concern is with deep ocean propagation only, and therefore the surface layer is only mentioned briefly.
- The Thermocline, beneath the surface layer, which is a section of the water column in which the temperature decreases rapidly with depth.
- The Deep Adiabatic Layer, between the thermocline and the ocean floor, this layer has an almost constant temperature.

Within the surface layer the sound speed structure is influenced by the local temperature variations experienced at the sea surface. In this thesis the primary concern is with deep sound propagation in the ocean and so the sound speed structure at the surface has been mentioned only briefly.

The decrease in temperature in the region of the thermocline results in a decrease in the sound speed with depth. However in the deep adiabatic layer, where the temperature is almost constant, the increase in pressure with depth results in an increase in sound speed with depth. At the interface between the thermocline and the deep adiabatic layer a sound speed minimum is present, shown in Figure 1.4, typically at a depth of $1\ 000\ m$.

Propagating sound is focused into the SOFAR channel, which is in the region of the sound speed minimum or sound channel axis. The sound channel axis is constrained to a spherical or ellipsoidal

surface depending on the form of the earth selected, for a range independent sound speed environment. In a range dependent environment the ray that propagates closest to the sound speed minimum is considered to be the axial propagation path (Dworski and Mercer 1990). Using the geometrical advantage associated with global range propagation, that is the small vertical range in the ocean compared to the very large horizontal propagation ranges, means that for global range propagation studies it is appropriate to consider axial sound propagation.

According to Munk and Wunsch (1993) a more convenient measure of sound speed is sound slowness, $S = \frac{1}{C}$. To remain consistent with later studies, for example Munk, Worcester, and Wunsch (1995), sound slowness has been used as a measure of sound speed in the ocean throughout this thesis.

Acoustic energy propagates away from the source in longitudinal waves. For this reason the theoretical basis underlying all mathematical models of acoustic propagation through the ocean is the acoustic wave equation (Etter 1991). A number of techniques have been derived for predicting acoustic propagation patterns through a known sound speed field. Many texts are available, which refer specifically to sound propagation modeling in far more detail than is included here, such as Etter (1991), Munk, Worcester, and Wunsch (1995) and Jensen, Kuperman, Porter, and Schmidt (1994).

The two most favored modeling methods used to understand underwater sound propagation problems are ray tracing and normal mode theory (Harrison 1989). These two techniques are introduced here and then each of them is discussed in terms of axial sound propagation. More detail regarding these two methods and their duality can be found in Munk and Wunsch (1993) and Munk, Worcester, and Wunsch (1995).

Ray tracing is a geometrical technique used to interpret sound propagation in the ocean. Rays are arcs of acoustic energy, which are always perpendicular to the wavefronts. Rays propagate through the ocean according to Snell's law, which implies that rays will always bend away from regions of higher sound speeds towards regions of lower sound speeds. The 'bending' is known as refraction and is a direct result of changes within the sound speed environment. As a result of Snell's law the sound speed minimum acts as a waveguide and sound propagating through the ocean follows the path of the sound speed minimum, and can thus propagate to great distance unless its path is blocked, by intrusive bottom topography for instance. The ray that propagates along the sound channel axis, referred to as the axial ray, describes the acoustic energy that propagates along the path of the sound speed minimum or sound slowness maximum.

Beginning with the wave equation:

$$(\nabla^2 - S^2 \frac{\partial^2}{\partial t^2})p = 0$$

Select a solution of the form:

$$p = p_0 e^{i\omega t}$$

Substituting this into the wave equation yields the Helmholtz equation:

$$(\nabla^2 + k^2)p_0 = 0$$

Where: k = the local wave number

ω = the local radian frequency

'Subscript 0' refers to a conveniently chosen reference value, which is generally the value of that parameter at the depth of the sound channel axis. The local frequency, ω, and the local wavenumber, k, are connected by a dispersion relationship, here the dispersion relationship is:

$$k = \omega S$$

Substituting an exact solution, for the wave equation, of the form:

$$p = A.e^{i(\omega t - k_0 W)},$$

Where: A = amplitude
W = phase function

into the Helmholtz equation under the adiabatic assumption that the ocean is a slowly varying sound speed medium, reduces the Helmholz equation to the Eikonal equation:

$$\mid \nabla W \mid^2 = (\frac{S}{S_0})^2 = \epsilon^2$$

Where: ϵ = the index of refraction

An advantage of the Eikonal equation over the wave equation is that it does not depend on time (Apel 1987). The propagation it describes is a high frequency asymptote. Constant values of W represent surfaces of constant phase or wavefronts. The normals to the wavefronts, defined as rays, are the paths of energy flux away from the source.

The ray equations arise from the variations of ∇W along the ray path, with distance along the ray path, s, in the direction of the normal. The ray equations parallel the characteristic form of Hamilton's equations for a conservative dynamical system (Lighthill 1978).

∇W is perpendicular to the wavefronts so that the ray trajectory $\underline{x}(s)$ satisfies:

$$\frac{d\underline{x}}{ds} = \frac{S_o}{S} \nabla W$$

Differentiation of this equation yields, after simplification, the ray equations in terms of sound slowness:

$$\frac{d}{ds}(S \frac{d\underline{x}}{ds}) = \nabla S$$

A simple example of ray propagation in a stratified channel such as the SOFAR channel is shown below in Figure 1.5. The refracted-refracted ray in the figure is confined to the neighborhood of the sound axis, penetrating upwards and downwards to the two ray turning depths, $\tilde{z}^+$ and $\tilde{z}^-$.

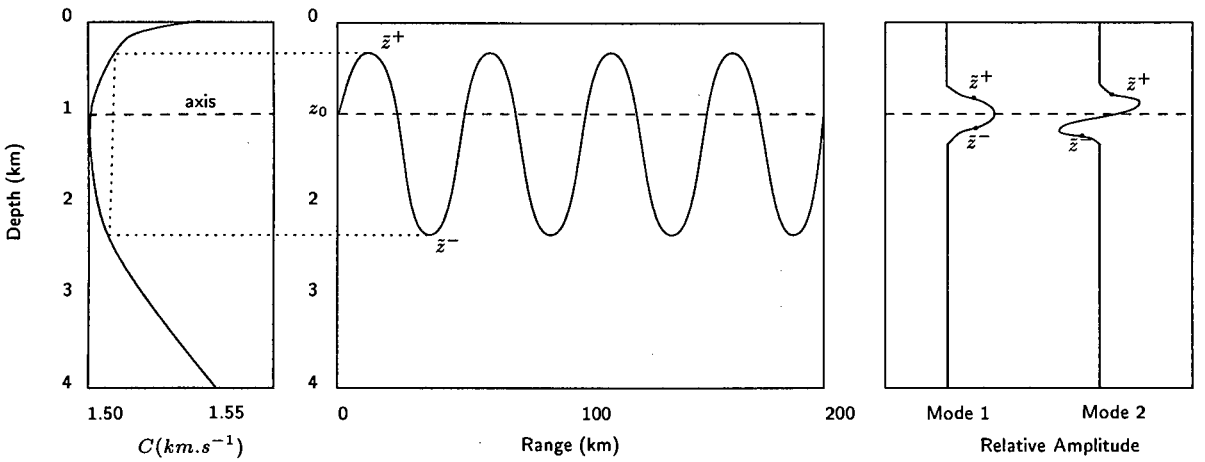

Figure 1.5: The panel on the left shows a typical mid-latitude sound speed profile; the central panel shows the ray path of a ray propagating close to the sound channel axis; finally the third panel contains the mode 1 and mode 2 functions (with frequency ω), corresponding to the sound speed profile. Adapted from Munk, Worcester and Wunsch (1995).

An alternative to ray tracing is that of **Normal mode theory**, which is also derived from the wave equation, using an integral representation of the wave equation. Practical solutions are obtained when cylindrical symmetry in a horizontally stratified medium is assumed. Modes are designated by $m = 1, 2, \ldots$ having $0, 1, \ldots, m-1$ zero crossings of the vertical wave function. The scale of the mode function depends on the frequency, ω. Higher frequencies are more concentrated near the axis.

The inflection points furthermost from the axis are measures of penetration of the modes into the ocean away from the axis, and are often referred to as turning points. An acoustic point source generates all these modes, with amplitudes proportional to the vertical wave function at the depth of the source. Each mode propagates with group velocity c_g (group slowness s_g), which is a known function of mode number m in frequency ω.

Derivations of normal mode theory, as with ray tracing are based on the wave equation:

$$(\nabla^2 - S^2(z)\frac{\partial^2}{\partial t^2})p = 0$$

has a separable solution in cylindrical coordinates, written as the product of a depth function, P, and a range function, Q.

$$p(r, z, t) = Q(r).P(z).e^{\imath\omega t}$$

The radial wave function, $Q(r)$ must satisfy the range equation, which satisfies the traveling wave portion of the solution, and is known as a zero order Bessel Equation:

$$\frac{1}{r}\frac{d}{dr}[r\frac{dQ}{dr}] + k_H^2 r = 0$$

The appropriate solution is a zero-order Hankel function ($H_0^{(1)}$):

$$Q(r) = H_0^1(k_H r) = r \to \infty \sqrt{\frac{2}{\pi k_H r}} e^{\imath(k_H r - \frac{\pi}{4})} \; for \; r \to \infty$$

Where: H_0^1 is a zero order Hankel function of the first kind
k_H is the horizontal wave number

The depth function, $P(z)$, must satisfy the depth equation also known as the normal mode equation, which describes the standing wave portion of the solution:

$$\frac{d^2P}{dz^2} + (\omega^2 S^2(z) - k_H^2)P = 0$$

Recognize that $\omega S(z) = k(z)$ is the scalar wave number and the local vertical wave number is:

$$k_V(z) = (\omega^2 S^2(z) - k_H^2)^{\frac{1}{2}}$$

Where: $k_V(z)$ is the vertical wavenumber which changes from a real to an imaginary value at the depth $\tilde{z}$. This depth $\tilde{z}$ is referred to as the modal turning depth and the sound slowness at that depth is represented by $\tilde{S}$.

The discrete values of k_H for which the modal solution exists are given by

$$\int_{\tilde{z}^-}^{\tilde{z}^+} (\omega^2 S^2(z) - k_H^2)dz = \pi(m - \frac{1}{2}) \; for \; m = 1, 2, 3, \ldots$$

The vertical function $P(z)$ oscillates close to the depth of the sound channel axis, and beyond the turning points it becomes exponential. This function is also referred to as the normal mode function and describes the standing wave portion of the solution. These means that each normal mode can be considered to be a traveling wave in the horizontal plane and a standing wave in the vertical plane.

An important parameter is the **Action**, A is known as the action variable and plays a central role in Hamiltonian Mechanics, it is referred to as the delay time in seismic literature.

Consider first the definition of the Action variable in terms of ray tracing. A ray propagating through the SOFAR channel will experience turning points at upper depths of $\tilde{z}^+$ and lower depths of $\tilde{z}^-$. Munk, Worcester, and Wunsch (1995) determine the horizontal range of a particular ray loop, R, and the associated travel time, T, as the sum of the upper and lower components of the upper and lower loops of a particular ray loop. Thus:

$$R = R^+ + R^- = 2\tilde{S} \int_{z_o}^{\tilde{z}^\pm} \frac{1}{(S^2 - \tilde{S}^2)^{\frac{1}{2}}} \partial z$$

$$T = T^+ + T^- = 2 \int_{z_o}^{\tilde{z}^\pm} \frac{S^2}{(S^2 - \tilde{S}^2)^{\frac{1}{2}}} \partial z$$

The Action, which is defined as the time delay variable, is written in the form:

$$A^\pm(\tilde{S}) := \pm 2 \int_{z_o}^{\tilde{z}^\pm} (S^2 - \tilde{S}^2)^{\frac{1}{2}} \partial z$$

Thus the Action variable is separated into upper and lower components:

$$A = A^+ + A^-$$

In terms of normal mode theory, consider the vertical wave function, $P(z)$, which also has turning points at the depth $\tilde{z}$, associated with the extreme points of inflection of the function.

The Action for a particular non-surface interacting mode, m, is defined by Munk, Worcester, and Wunsch (1995) as:

$$A_m = \frac{2\pi(m - \frac{1}{2})}{\omega}$$

Different modes that have the same value of A have the same turning points.

In ray theory the axial ray has an Action value of zero, while in normal mode theory the axial mode, mode 1, has the smallest value of the Action.

1.3 Notation

This section introduces notation and techniques that are used throughout the remainder of this thesis. The notation is introduced for range independent propagation on a spherical earth. In this study, where the concern is with global underwater sound propagation the position of a point on the surface of the earth is defined in terms of only two coordinates - those of north latitude, $\lambda \in [-90^o, 90^o]$, and east longitude, $\phi \in [-180^o, 180^o]$. The local ray direction measured clockwise from north is $\alpha \in [0^o, 360^o]$.

The following table reflects the relationship between subscripts, that are used throughout this thesis, and the positions they represent for each ray on a spherical surface.

Subscript	Position
S	Source
A	Antipode
E	Extreme Latitudinal Turning Point
Eq	Equatorial Crossing Point

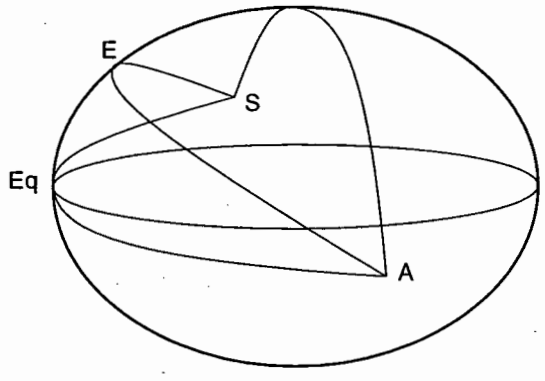

Figure 1.6: Subscripts used throughout this thesis on a spherical earth, which have been defined in the table above.

At this stage notation regarding the great semi-circle antipodal distances is introduced.

Three great semi-circles are shown in Figure 1.6, for a Northern Hemisphere source, $S(\lambda_S, \phi_S)$ to a Southern Hemisphere antipode, $A(\lambda_A, \phi_A)$, and $\alpha_S \in [0^o, 90^o]$, is in the first quadrant.

Where: $\lambda_S > 0$ and $\lambda_A = -\lambda_S < 0$
and: $\phi_A = (\phi_S + 180) \mid_{\text{mod } 360}$

Thus: $(\lambda_A, \phi_A) = (-\lambda_S, (\phi_S + 180) \mid_{\text{mod } 360})$.
and: $\alpha_A \in [90^o, 180^o]$, the second quadrant.

Consider the azimuthal angle for the following particular rays:

For the polar ray: $\alpha_S = 0^o$ $\alpha_A = 180^o$ $\lambda_E = 90^o$.
For the mid-latitude ray: $\alpha_S > 0^o$ $\alpha_A > 0^o$ $0 < \lambda_S < \lambda_E < 90^o$.
For the tropical ray: $\alpha_S = 90^o$ $\alpha_A = 90^o$ $\lambda_E = \lambda_S$.

In general: $\alpha_A = 180^o - \alpha_S$.

The following figure and table demonstrate the relationship between the azimuthal departure angle from the source to the azimuthal arrival angle at the antipode for each quadrant.

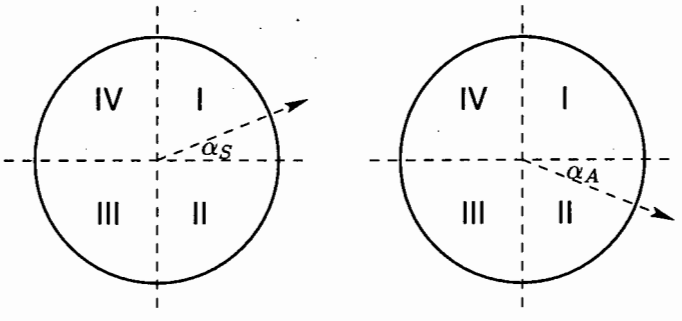

Figure 1.7: The azimuthal angle quadrants associated with the source and the antipode, actual results are shown in the table below.

Source		Antipode	
α_S	Quadrant	α_A	Quadrant
$0^o \to 90^o$	I	$180^o \to 90^o$	II
$90^o \to 180^o$	II	$90^o \to 0^o$	I
$180^o \to 270^o$	III	$360^o \to 270^o$	IV
$270^o \to 360^o$	IV	$270^o \to 180^o$	III

Along each great semi-circle, the local latitude and ray direction are given from Snell's law, which implies that sound rays propagating through the ocean bend away from regions of higher sound speed. Snell's law on a spherical earth is written as:

$$\begin{aligned} \cos\lambda . \sin\alpha &= constant = H, say. \\ &= \cos\lambda_S . \sin\alpha_S \\ &= \cos\lambda_A . \sin\alpha_A \end{aligned}$$

Now since:

$$\lambda_A = \lambda_S$$
$$\cos\lambda_A = \cos\lambda_S$$

Thus, Snell's law implies:

$$\sin\alpha_A = \sin\alpha_S$$
$$\Rightarrow \alpha_A = \alpha_S \quad or \quad \alpha_A = 180 - \alpha_S$$

and

$$sign(\alpha_A) = sign(\alpha_S) = sign(H)$$

This can be expressed in tabular form, for the azimuthal angle, α, for each ray:

Source Quadrant	Antipodal Quadrant	sign(H)
I	II	> 0
II	I	> 0
III	IV	< 0
IV	III	< 0

One can specify H for a given latitude by substituting known values of λ and α, for example λ_S and α_S, and thus provide values for other unknown positions along the ray such as at the extreme latitudinal turning point and the equatorial crossing point.

Consider the extreme latitudinal turning point, which is achieved when $\alpha = 90^o = \alpha_E$:

$$\cos\lambda_E = \cos\lambda.\sin\alpha = \cos\lambda_S.\sin\alpha_S = \cos\lambda_A.\sin\alpha_A = H$$

Clearly, $\lambda_S \leq \lambda_E \leq 90^o$ always and λ_E for any source, described by the initial position $(\lambda_S; \alpha_S)$, on a particular great circle is always the same.

Also, the equatorial crossing point of a ray, when $\lambda = 0^o = \lambda_{Eq}$:

$$\sin\alpha_{Eq} = \cos\lambda.\sin\alpha = \cos\lambda_S.\sin\alpha_S = \cos\lambda_A.\sin\alpha_A = H$$

The examples demonstrate clearly, that if the source position is known, then H can easily be determined, and thus specific positions along the ray can be established.

The symmetry of the situation means that for the great semi-circle distance:

$$G.S.C.D. = \int_S^A ds = 2\int_{Eq}^E ds$$

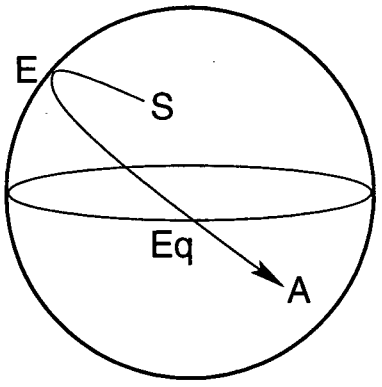

Figure 1.8: The symmetry on the surface of the sphere, means that the distance $S \rightarrow A$ is twice the distance $Eq \rightarrow E$.

The ray propagation equation: $R\frac{d\lambda}{ds} = \cos\alpha$ is now used to give:

$$\begin{aligned} G.S.C.D. &= 2.R. \int_0^{\lambda_E} \frac{1}{\cos\alpha} d\lambda \\ &= 2.R. \int_0^{\lambda_E} \frac{1}{\sqrt{1 - \frac{\cos^2\lambda_E}{\cos^2\lambda}}} d\lambda \\ &= 2.R. \int_0^{\lambda_E} \frac{\cos\lambda}{\sqrt{\cos^2\lambda - \cos^2\lambda_E}} d\lambda \\ &= 2.R. \int_0^{\lambda_E} \frac{\cos\lambda}{\sqrt{\sin^2\lambda_E - \sin^2\lambda}} d\lambda \\ &= 2.R. \int_0^{\lambda_E} \frac{\cos\lambda}{\sin\lambda_E \sqrt{1 - \frac{\sin^2\lambda}{\sin^2\lambda_E}}} d\lambda \\ &= 2.R. \int_0^{\lambda_E} \frac{1}{\sqrt{1 - (\frac{\sin\lambda}{\sin\lambda_E})^2}} d(\frac{sin\lambda}{\sin\lambda_E}) \end{aligned}$$

Put: $y = \frac{\sin\lambda}{\sin\lambda_E}$

$$G.S.C.D. = 2.R. \int_0^1 \frac{1}{\sqrt{1 - y^2}} dy$$

Put: $y = \sin q$

$$\begin{aligned} G.S.C.D. &= 2.R. \int_0^{\frac{\pi}{2}} \frac{\cos q}{\cos q} dq \\ &\Rightarrow G.S.C.D. = \pi R \end{aligned}$$

Details for this argument are provided here, because this technique, introduced for a simple situation, is useful in more complex situations, which arise later on in this work.

Chapter 2

The Geometric and Refractive Assumptions

The two principal factors which affect global range propagation paths were introduced in the preceding chapter as the geometric assumption, which refers to the form of the earth, and the refractive assumption, which refers to horizontal variations in sound speed. In this chapter these two assumptions and their implications for an axially propagating sound signal are considered separately. In fact, throughout this thesis, these two assumptions are considered separately in order to determine the inherent character of each of the assumptions and to determine their individual contribution to the nature of the antipodal region.

In the first section the geometric assumption is considered, specifically the effects of the form of the earth on a global range propagation path within a range dependent sound speed environment. The first consideration is that of a spherical earth, which is described in detail to provide an understanding of the necessary geometry involved. The spherical earth is then extended to an ellipsoidal earth form, which is a closer approximation to the true form of the earth yet has similar geometric relationships to that of the spherical earth model.

In the second section of this chapter the effects of horizontal sound speed variation, which are referred to as refractive effects, are considered in detail. In order to isolate refractive effects from the geometric effects of the previous section, the sound speed environment is described on a spherical earth only. Since sound propagates through the sound speed channel in the ocean, the effects of horizontal sound speed variability on the sound speed axis are described.

2.1 Geometric Assumption

In this section the form of the earth is considered in detail, with regard to its effect on global range sound propagation. The geometry regarding a spherical earth is provided and upon this basis the ellipsoidal form of the earth is introduced. The work of Pearson (1990) is used extensively throughout this section.

The form of the earth refers to the physical and mathematical surface of the earth. The irregular surface of the earth, which includes both ocean surfaces and land masses, cannot be modeled easily. The ancient Greeks, among them Pythagoras (540 BC) and Aristotle (384–322 BC) believed that the earth was a sphere (Strahler 1975), which is considered to be the most basic form of the earth. The use of a sphere as a model of the earth greatly simplifies the mathematics required to model upon the earth's surface (Torge 1980).

If the only forces acting upon the earth were gravitational forces then the earth would be a sphere. However, centrifugal and rotational forces deform the shape of the earth into a figure, which is in equilibrium with respect to gravitational and rotational forces (Kaula 1967). As the earth rotates so it tends to be cast outwards in opposition to the centripetal attraction of the force of gravity, this outward forcing is greatest at the equator. Thus a standard representation of the form of the earth is the oblate ellipsoid, which is defined by revolving an ellipse about it's semi-major axis. The distortion from a spherical shape in which the equatorial diameter exceeds the polar diameter refers to the oblateness of the feature (Parker 1994). When the semi-major axis corresponds with the axis of rotation of the earth, the earth ellipsoid or spheroid, is mathematically classified as an oblate spheroid. From this discussion it is clear that the oblate spheroid is a closer approximation to the actual form of the earth than the sphere.

The **spherical model** of the earth is clearly the simplest representation and thus the easiest to implement. The equation for the sphere in Cartesian coordinates is given by:

$$\frac{x^2}{R^2} + \frac{y^2}{R^2} + \frac{z^2}{R^2} = 1$$

where R is the radius of the sphere and has a value of approximately $6372.4\ km$ (Munk, O'Reilly, and Reid 1988).

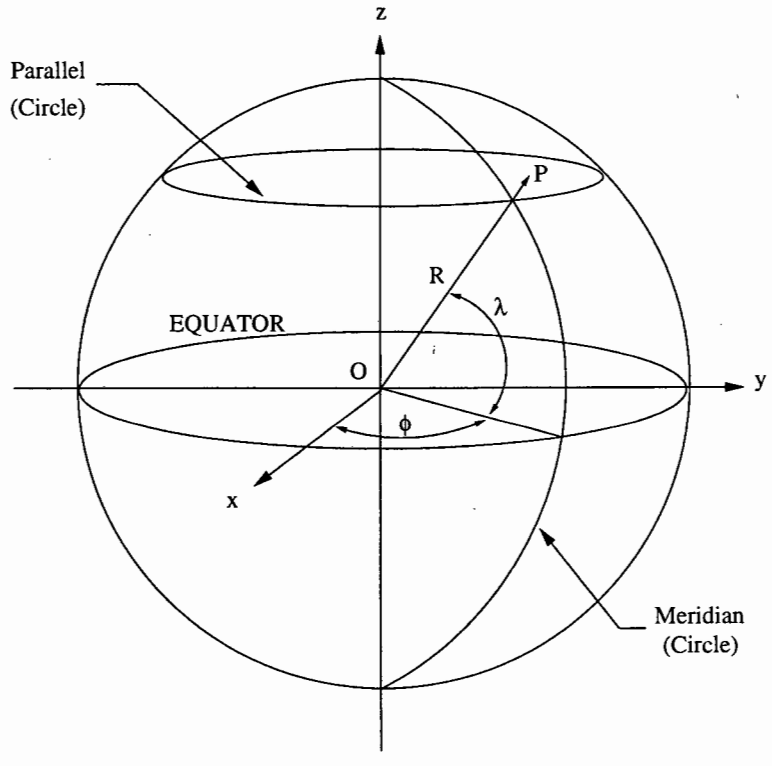

Figure 2.1: Geometry of the sphere.

Any point on the surface of the spherical earth model can be determined using the Cartesian coordinates x, y and z. But, since any point is constrained to lie on the surface the coordinates are not independent and are related by the equation of the surface defined by the equation for the sphere. Therefore there

are only two independent coordinates and instead of using two randomly chosen independent coordinates, it is often more useful and appropriate to use an angular coordinate system, with two angular variables.

Two angular coordinates are required to uniquely define the position of a point, P say, on the surface of the sphere. The first is latitude, λ, which is the angle between a vector from the center of the sphere to the point, P, and the $X-Y$ plane. It is conventional to measure latitude as positive in the Northern Hemisphere and negative in the Southern Hemisphere. The second coordinate is longitude, ϕ, which is measured in the $X-Y$ plane and has been defined as the angle of rotation from the $x-axis$. The convention for longitude is to measure rotation towards the east as positive and towards the west as negative.

It is conventional to use latitude and longitude to form a geographic grid for the purposes of locating position on the surface of the earth. The axis of rotation provides two points, the north and south poles, upon which the grid can be based. North–south lines connecting the poles, known as meridians, and east–west lines parallel to the equator, known as parallels, provide the framework.

The intersection between a sphere and a plane passing through its center (regardless of the attitude of the plane) is known as a great circle. Circles produced in this way, but not passing through the center of the sphere, are known as small circles. Because of the definition of a great circle, a great circle is the largest possible circle that can be drawn on the surface of a sphere. Also only one great circle can be drawn on the surface of the sphere that will pass between two given points on the surface, unless the two points are on diametrically opposite sides of the sphere, in which case an infinite number of great circles can be drawn through them (Strahler 1975).

The mathematical surface which is considered to most closely fit the form of the earth is that of the **oblate spheroid.** The oblate spheroid is generated by rotating an ellipse about its axis so that the equatorial diameter exceeds the length of the polar axis.

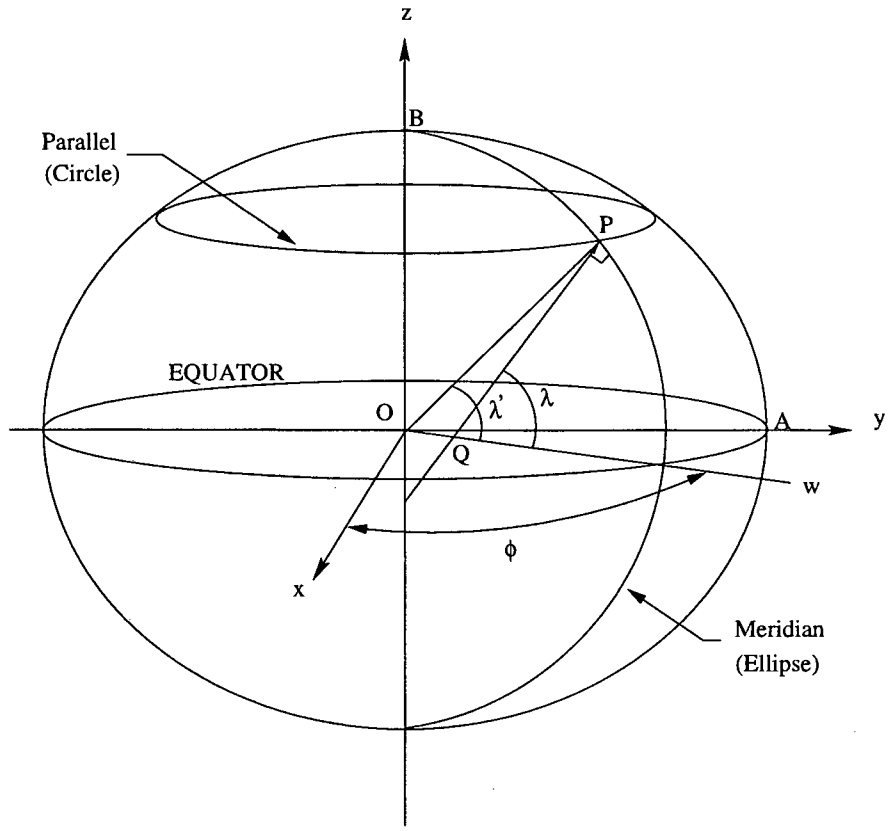

Figure 2.2: Geometry of the spheroid.

In Figure 2.2 the semi-major axis, a, is the length of the line segment OA, along the $y-axis$. The semi-minor axis, b, is the length of the line segment OB, along the $z-axis$, which is used as the axis of rotation when generating the oblate ellipsoid. The equation for an ellipse, centered at O, in Cartesian coordinates is:

$$\frac{x^2}{a^2} + \frac{z^2}{b^2} = 1$$

The oblateness of the spheroid is, by definition, the distortion from a spherical shape, in which the diameter at the equator exceeds that at the poles (Parker 1994). The oblateness is also referred to as the degree of flattening (f) of the poles and can be determined by examining the ratio between the difference in length between the semi-major axis, which is the equatorial radius, and the semi-minor axis, to the length of the semi-major axis:

$$f = \frac{a-b}{a}$$

The eccentricity, e, defined as the degree of departure of the ellipse from a circle is determined by:

$$e^2 = \frac{a^2-b^2}{a^2} = 2f - f^2$$

The WGS-84 (Department of Defence World Geodetic System, 1984) spheroid has been used in this thesis, since it has been taken to be the best representation available today in many texts (Pearson

1990). The WGS-84 spheroid has been defined with a semi-major and semi-minor axis of 6 378 137 m and 6 356 752 m, respectively. From these values the eccentricity and flattening can be determined as 0.081819 and 0.003353 respectively.

Because the spheroid has less symmetry than the sphere more complex relationships exist between the coordinates. As with the sphere an angular coordinate system, using latitude and longitude, can be used to determine position on the surface of the oblate spheroid. However, for the spheroid two types of latitude have been defined: the geocentric and the geodetic latitude.

The geocentric latitude of a position on the surface of the earth is defined as the angle between the line to the center of the earth and the plane of the equator (Parker 1994). In Figure 2.2 the geocentric latitude of point P would be the angle POw or λ'. The geodetic latitude of a position is defined as the angular distance between the plane of the equator and a normal to the spheroid (Parker 1994). Hence, in Figure 2.2 the geodetic latitude is given by the angle PQw or λ, where Qw is in the $xy - plane$.

A relationship between the two types of latitudes exist and is described here:

Consider a Polar coordinate system and Figure 2.2. Let the magnitude of the vector between the origin, O, and a point, P be r. Then the relationship between the Cartesian coordinates and Polar coordinates is:

$$\begin{aligned} x &= r \cos\lambda' \\ z &= r \sin\lambda' \end{aligned}$$

which can be combined together to form:

$$\frac{z}{x} = \tan\lambda'$$

Also the geodetic latitude, λ, defines the inclination of the line QP, which is normal to the ellipse at P.

$$\tan\lambda = -\frac{\partial x}{\partial z}$$

Now taking the differential of the equation for an ellipse gives:

$$\begin{aligned} \frac{2x}{a^2}\partial x + \frac{2z}{b^2}\partial z &= 0 \\ \Rightarrow \frac{\partial x}{\partial z} &= -\frac{a^2}{b^2}\frac{z}{x} \end{aligned}$$

Substituting this gives:

$$\begin{aligned} \tan\lambda &= \frac{a^2}{b^2}\frac{z}{x} \\ \Rightarrow \tan\lambda &= \frac{a^2}{b^2}\tan\lambda' \\ or\ \tan\lambda' &= \frac{b^2}{a^2}\tan\lambda \end{aligned}$$

and, since $e^2 = \frac{a^2-b^2}{a^2}$ *a relationship between geocentric and geodetic latitude can be written as:*

$$\tan \lambda' = (1 - e^2) \tan \lambda$$

The value of the eccentricity for the reference ellipsoid is small and because of this the differences in magnitude between the geocentric and geodetic latitude at any given point are small. At 0^o and 90^o the two latitudes are the same while at 45^o the greatest differences occur. For the WGS-84 ellipsoid the greatest difference is $< 0.2^o$, at 45^oN or 45^oS.

In acoustic propagation modeling the difference between the two latitudes can be interpreted as the departure from the vertical that would affect the given sound speed environmental data - "In that sense it is a negligible difference" (Dworski and Mercer 1990). According to Dworski and Mercer (1990), texts in general do not distinguish between the two latitudes but refer simply to 'latitude' and this is commonly understood to be the geodetic latitude, λ.

In Figure 2.2 the spheroidal surface has been illustrated using a three-dimensional Cartesian coordinate system. The equation for the oblate spheroid, using this system is:

$$\frac{x^2}{a^2} + \frac{y^2}{a^2} + \frac{z^2}{b^2} = 1$$

where a is the semi-major axis of revolution and b is the semi-minor axis.

The radii of curvature are introduced in this section as they become important later on in this thesis, where distances and the nature of sound propagation paths are considered. Their derivations are not provided here, since they can be found in a number of texts regarding the form of the earth and geometry on a spheroid, for example Pearson (1990). The equations for the radius of a circle of parallel and the radius of curvature are independent of longitude, this is a characteristic of surfaces of revolution.

1. Radius of parallel, R_o:

$$R_o = \frac{a \cos \lambda}{\sqrt{1 - e^2 \sin^2 \lambda}}$$

2. Radius of curvature of the spheroid in the plane perpendicular to the meridional plane, R_p:

$$R_p = \frac{a}{\sqrt{1 - e^2 \sin^2 \lambda}}$$

3. The radius of curvature of the meridional ellipse, R_m:

$$R_m = \frac{a(1 - e^2)}{(1 - e^2 \sin^2 \lambda)^{\frac{3}{2}}}$$

It is useful to relate the three-dimensional Cartesian coordinates for the spheroid to angular coordinates, this is done using the radius of curvature of the spheroid in the plane perpendicular to the meridional

plane, as follows:

$$\begin{aligned} x &= R_p \cos\lambda \cos\Delta\phi \\ y &= R_p \cos\lambda \sin\Delta\phi \\ z &= (1-e^2) R_p \sin\lambda \end{aligned}$$

According to Fermat's principle sound travels along the path with the minimum travel time. Under the assumption of a uniform sound speed environment Fermat's condition of minimum travel time is considered to be the same as that of minimum range. The appropriate shortest path on the ellipsoidal earth is the geodesic. The standard definition of a geodesic is that it is the shortest line between two points on a curved surface (Parker 1994).

In general the equations to derive the geodesic path on an ellipsoidal earth are constructed by numerically integrating the geodesic equations: (from Munk, O'Reilly, and Reid (1988) and also Bomford (1980)).

$$\begin{aligned} \frac{d\lambda}{ds} &= \frac{\cos\alpha}{R_m} \\ \frac{d\phi}{ds} &= \frac{\sin\alpha}{R_p \cos\phi} \\ \frac{d\alpha}{ds} &= \frac{\sin\alpha \tan\phi}{R_p} \end{aligned}$$

The first two of these equations describe changes in latitude and longitude, while the third equation represents the azimuthal steering in the horizontal plane. When sound speed, C, is constant as is the case for this assumption, the equation that determines the azimuthal steering, $\frac{d\alpha}{ds}$, is equivalent to the Hamiltonian equation:

$$H = R_p . \cos\lambda . \sin\alpha = constant$$

which is the equation for the geodesic (Munk, O'Reilly, and Reid 1988). This equation reduces to the great circle equation on a sphere, since $e = 0 \Rightarrow R_p = a$, thus

$$H = \cos\lambda . \sin\alpha = constant$$

Munk, O'Reilly, and Reid (1988) noted that while there is a short range difference between the geodesic path and the great circle path on the surface of the earth, what is significant is that the geodesic path is displaced further south than the great circle path. The southward displacement of the geodesic follows since the shortest path would be displaced towards higher latitudes where the radius of the earth is smaller.

2.2 Refractive Assumption

In this section the sound speed structure associated with the world oceans has been considered, particularly with regard to the latitudinal variability of sound slowness. It contains an overview of the global ocean in terms of horizontal sound speed variability or rather sound slowness variability. In order to introduce the ideas associated with horizontal sound speed variability within the world oceans, this

Section builds upon ideas introduced in Section 1.2, particularly with reference to axial sound propagation, which is the form of propagation utilized in global propagation studies.

Because this thesis is concerned with global range propagation a global view of sound variability within the ocean is required. The figure below, Figure 2.3 demonstrates firstly the depth of the sound channel axis and secondly the actual sound speed value at the depth of the sound channel axis.

The data used to prepare the maps was taken from a set of approximately 8 000 hydrographic stations that have been selected in many studies to represent the world oceans (Munk, O'Reilly, and Reid 1988). The data in the very high latitudes was sparse and mostly collected during the summer months and so it is not truly representative of the situation there (Dworski and Mercer 1990).

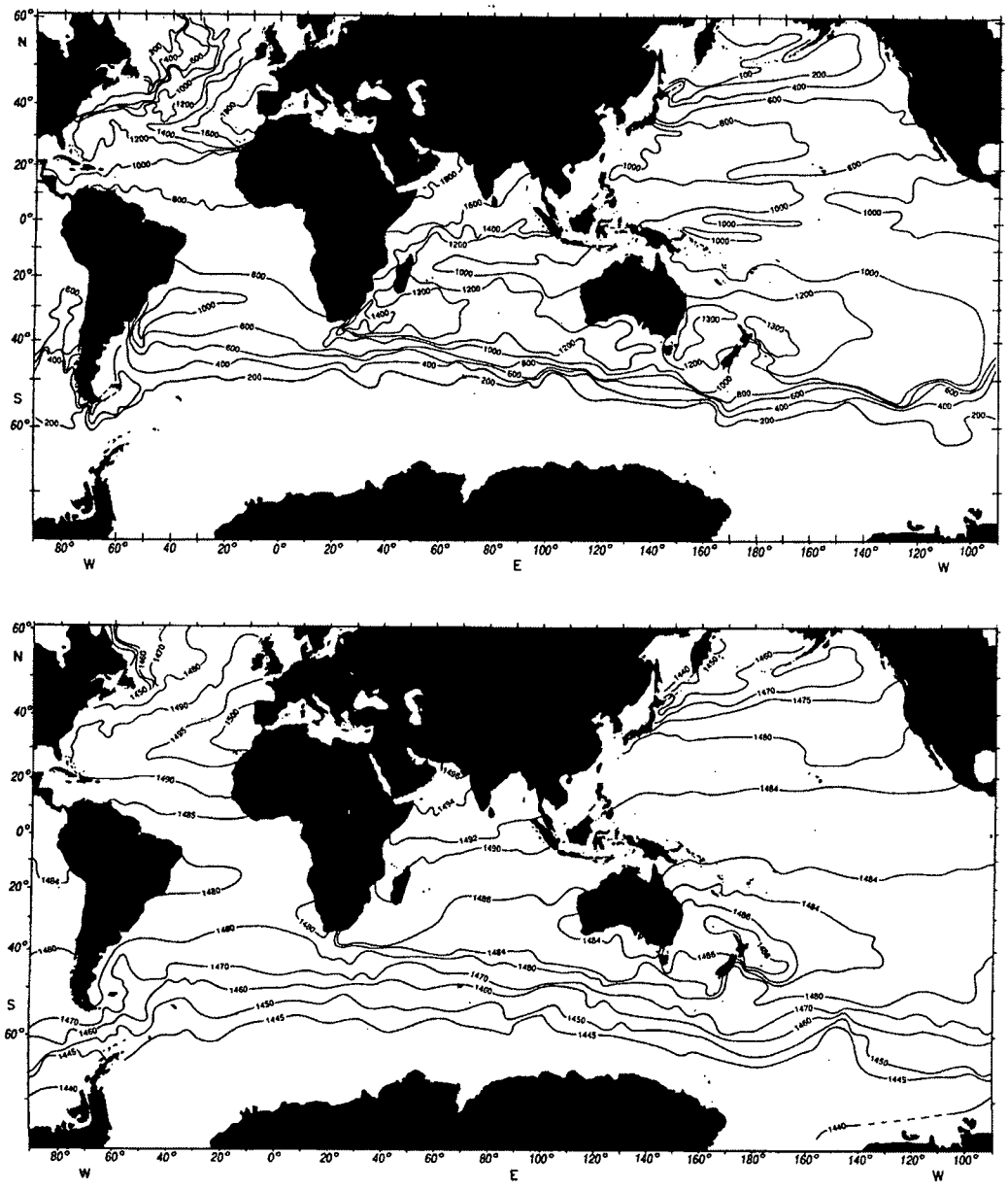

Figure 2.3: The depth of the minimum sound speed axis in meters (top) and the sound speed in meters per second (bottom) (Munk and Forbes, 1989).

Throughout most of the world oceans the depth of the sound channel channel axis lies between 800 m and 1 000 m below sea level. The figure indicates that the sound channel axis rises with distance from the equator actually shoaling and eventually outcropping in the polar regions.

The deeper depths of the sound channel in the mid-latitudes corresponds to the warmer waters that occur and thus the maximum sound speed, and by inference the minimum sound slowness. Similarly the shallow or surface axis associated with the cold polar waters corresponds to the minimum sound speed values and hence the highest sound slowness values.

The strong latitudinal gradients in the region of the Antarctic Circumpolar Current, where sound speed

decreases rapidly with latitude corresponding to the thermal structure, are also apparent from the figure.

The figure indicates an underlying latitudinal dependence of sound speed and thus on sound slowness. This indicates that a reasonable representation of sound slowness is an even function of latitude, increasing from a minimum value at the equator to a maximum value at the poles.

Figure 2.4 below, taken from Munk, Worcester, and Wunsch (1995), shows a generalized ray path that demonstrates an accepted model of latitudinal axial variability. The sound channel axis is at a depth of approximately $1\ 000\ m$ within the mid-latitudes, shoaling with increasing latitude and finally outcropping within the polar waters.

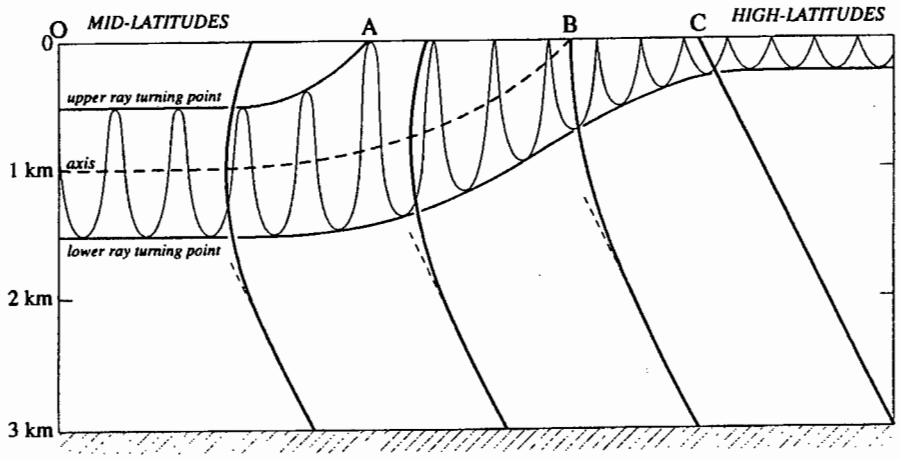

Figure 2.4: A schematic representation of the latitudinal variation of a SOFAR ray path, taken from Munk, Worcester and Wunsch 1995.

The ray paths demonstrate the effect of the variable depth of the sound channel axis on sound propagation. The rays vary from Refracted-Refracted rays in the mid-latitudes to Refracted-Surface-Refracted rays in the high latitudes.

The sound speed profiles included in Figure 2.4 demonstrate a typical profile in the mid-latitudes. Between A and B the sound channel axis is shoaling, and reaches the surface at B. Finally at C the sound speed becomes adiabatic throughout the depth and the sound speed minimum is positioned at the ocean surface.

As mentioned in Section 1.1, Munk, O'Reilly, and Reid (1988) considered a one-dimensional model of the world ocean, using latitude as the dependent variable. However, those authors felt that their model was inadequate considering the large differences in sound speed values, in the mid-latitudes, between the Indian, Pacific and the Atlantic. Latitudinally the Pacific and the Atlantic Oceans appear to be remarkably similar; it is the Indian Ocean which is anomalous. However, as Dworski and Mercer (1990) concluded "an antipodal geometry exists for underwater paths on earth and it is most likely only realizable between the Southern Indian and the North Atlantic Oceans."

By ignoring the mid-latitudinal Indian Ocean where global range propagation paths can not exist,

the discussion above indicates that a one-dimensional even function is a reasonable representation of latitudinal sound slowness of the world oceans. In order to determine this function actual sound speed values were taken from Figure 2.3, these were then transformed into sound slowness values, which were then fitted to a *cosine* function.

Firstly the two extreme points were considered. That is the sound speed values (in $m.s^{-}1$) at the equator and as close to a polar value as possible.

$$C(0^o) = 1\ 484 \Rightarrow S(0^o) = 673.8E-6$$
$$C(90^o) = 1\ 440 \Rightarrow S(90^o) = 694.4E-6$$

The derived Sound Slowness Model was selected to be a function of the form of the sum of a reference sound slowness value, S_o, and a sound slowness perturbation model, ΔS. Thus:

$$S(\lambda) := S_o + \Delta S$$

The sound slowness perturbation model consists of an even function of the form $-\mathcal{A}\cos 2\lambda$, which represents the frontal regions in each of the hemispheres. This means that:

$$S(\lambda) := S_o - \mathcal{A}\cos 2\lambda$$

Where: $S_o := \frac{S(0^o)+S(90^o)}{2} = 684.1E-6$
and: $\mathcal{A} := \frac{S(90^o)-S(0^o)}{2} = 10.3E-6$

A comparison is performed in order to validate the model, using a sound speed value taken from Figure 2.3 at 60^o.

$$C(60^o) = 1\ 445 \Rightarrow S(60^o) = 692.0E-6$$

And using the proposed sound slowness model:

$$S(60^o) = S_o - \mathcal{A}\cos 2\lambda$$
$$= 684.1E-6 - 10.3E-6\cos 120^o$$
$$= 689.2E-6$$

The model function and the observed data point agree well. The sound slowness model has been plotted below in Figure 2.5 against data values taken from Figure 2.3. The figure is included so as to demonstrate the close similarities between the proposed latitudinal sound slowness model and observed sound slowness data values.

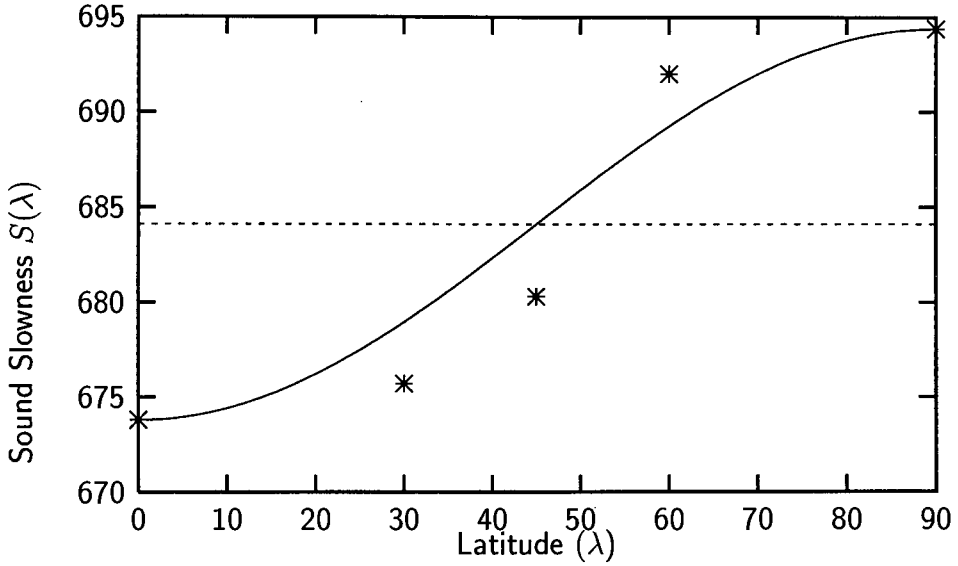

Figure 2.5: Comparison between observed sound slowness values (*), taken from Figure 2.3, and the proposed sound slowness model, $S(\lambda)$. The sound slowness values have been multiplied by 10^6.

Notice that the sound slowness model front is situated at 45^o, while the actual front can be observed in Figure 2.3 at 50^o.

Munk, O'Reilly, and Reid (1988) and Dworski and Mercer (1990) both demonstrated that horizontal refraction modifies sound ray paths, on a spherical or ellipsoidal earth, significantly. Also, the only feasible global range propagation paths involve propagation through the cold polar waters of the Southern Ocean. The strong thermohaline front and the Antarctic Circumpolar Current are the two major zonal structures in the Southern Ocean. The current itself has a very small effect on sound propagating across it, simply because the sound speed of the ray propagating through the current, $\pm 1\ 450\ m.s^{-}1$, is extremely high when compared to the current speed of $0.3\ m.s^{-1}$, thus the ray does not spend very much time within the influence of the current.

Dworski and Mercer (1990) did, however, determine that the significant deviation to the refracted geodesic as opposed to the unrefracted geodesic on the ellipsoidal earth was due to the intense thermohaline Circumpolar Front, since their modeled source and receivers were placed on either side of the front.

Under this assumption, where the form of the earth is taken to be a sphere, minimum range paths are no longer appropriate for determining Fermat paths between source and receiver, rather minimum t paths have to be taken into account. The ray equations, under this assumption, are (according to Munk, O'Reilly, and Reid (1988)):

$$\frac{d\lambda}{dt} = \frac{C(\lambda,\phi)}{R}\cos\alpha$$
$$\frac{d\phi}{dt} = \frac{C(\lambda,\phi)}{R}\frac{\sin\alpha}{\cos\lambda}$$

$$\frac{d\alpha}{dt} = \frac{1}{R}\sin\alpha\frac{dC(\lambda,\phi)}{d\lambda} - \frac{1}{R}\frac{\cos\alpha}{\cos\lambda}\frac{dC(\lambda,\phi)}{d\phi} + \frac{C(\lambda,\phi)}{R}\sin\alpha\tan\alpha$$

Where: $C(\lambda,\phi)$ is the sound speed at the axis.

For the case that the sound speed is a function of latitude only, the ray equations become:

$$\frac{d\lambda}{dt} = \frac{C(\lambda)}{R}\cos\alpha$$
$$\frac{d\phi}{dt} = \frac{C(\lambda)}{R}\frac{\sin\alpha}{\cos\lambda}$$
$$\frac{d\alpha}{dt} = \frac{1}{R}\sin\alpha\frac{dC(\lambda)}{d\lambda} + \frac{C(\lambda)}{R}\sin\alpha\tan\alpha$$

Also in this case the equation for $\frac{d\alpha}{dt}$ is equivalent to:

$$H = C^{-1}(\lambda).\cos\lambda.\sin\alpha = constant$$
$$or$$
$$H = S(\lambda).\cos\lambda.\sin\alpha = constant$$

This equation represents Snell's law on a sphere. If sound speed, C is a constant, then the equations again reduce to the great-circle equation.

Chapter 3

Distance Discrepancy and its Approximation

In order to develop an algorithm for determining the form and extent of the antipodal region it is necessary that the distance discrepancy function, d, be determined for both the geometric and refractive assumptions. The distance discrepancy function is defined as the distance travelled on each ray within the antipodal region. It is defined as a function of both the local latitude and local ray direction, measured clockwise from north. For ray points which are still to reach the antipodal region, the discrepancy function is taken to be negative.

Two approaches are considered for determining d. The first approach is used with regard to the geometric assumption. This approach maps out the position of the wave front at a particular time and yields the geometric distance discrepancy function, d_G. The second approach is used with regard to the refractive assumption. It establishes the travel times at a fixed distance along each ray emanating from the source and yields the refractive distance discrepancy function, d_R.

For each distance discrepancy function determined in this chapter a graph is plotted. The graphs are produced using a polar coordinate system, where positive and negative values of the distance discrepancy functions are plotted for the azimuthal range, $\alpha \in [0^o; 360^o]$. A 'value table' of the specific distance discrepancy function for specific values of α is provided alongside each graph, so as to aid interpretation of the function under consideration.

In order to assist with the interpretation of these functions with regard to their orientation and bearing within the azimuthal range, a table referred to as an octant table is included for each function. An octant table is defined in the following way: consider dividing the azimuthal range into eight regions of 45^o each, these smaller ranges correspond to an arc of the relevant function. The graphs of the function are plotted for accumulative azimuthal octant ranges, that is the ranges: $[0^o; 45^o]; [0^o; 90^o]; [0^o; 135^o]; \ldots [0^o; 360^o]$. The octant table thus demonstrates the bearing and development of the relevant function over the complete azimuthal range.

3.1 Geometric Approach

In this Section the distance discrepancy function under the geometric assumption is determined. This function is referred to as the geometric distance discrepancy function and concerns the distance dis-

crepancy function in a range independent sound speed environment on a spheroidal earth. In order to derive this function much use is made of Longuet-Higgins (1990).

A unique ellipse on the surface of the spheroidal earth can be defined once the source point $S(\lambda_S, \phi_S)$ and the tangent direction at the source point, α_S, are specified. Distance along the ellipse, from the source point to a range of half a circumference of the ellipse, yields a point B, where the position of B is:

$$B := (\lambda_B, \phi_B) = (-\lambda_S; 180^o + \phi_S)$$

B is referred to as the center of the antipodal region. The half circumference of the ellipse depends on α_S and λ_S, or equivalently on α_B and λ_B. A geodesic path will not always pass through the center of the antipodal region.

The geodesic path, which has the same tangent to the ellipse at the source, the dashed line in Figure 3.1, is considered. From Munk, O'Reilly, and Reid (1988), it is known that the geodesic path will lie poleward of the ellipsoidal path, since the radius of the earth ellipsoid is shorter at higher latitudes. At this stage it is important to determine how closely the ellipsoidal path approximates that of the geodesic path.

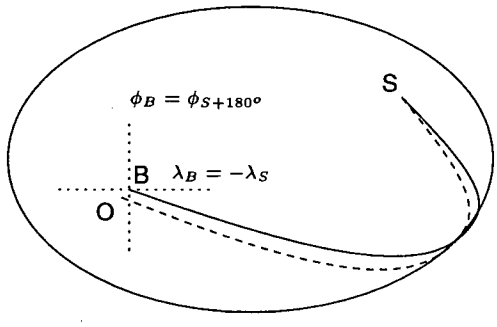

Figure 3.1: The ray path along the geodesic (dashed path) and the ellipse (solid path) associated with the spheroidal form of the earth.

According to Longuet-Higgins (1990), the geodesic curve is almost parallel to the curve of the ellipse always, that is the two curves differ by a small angle, f, throughout their extent and their separation is also of the order f. Previously in Section 2.1, f was defined as the degree of flattening of the spheroidal earth. However, the length of the geodesic curve at a given time differs from that of the ellipsoidal curve, to the second order of f (Longuet-Higgins 1990).

A detailed view of the antipodal region is provided below in Figure 3.2. The perpendicular from the ellipse at B is considered, this line intersects the geodesic curve orthogonally at the point O. Using the Longuet-Higgins argument in this scenario means that, to the second order in f, the distance from the source to B is the same as the distance from the source to O, which from the definition of B is the half circumference of the ellipse.

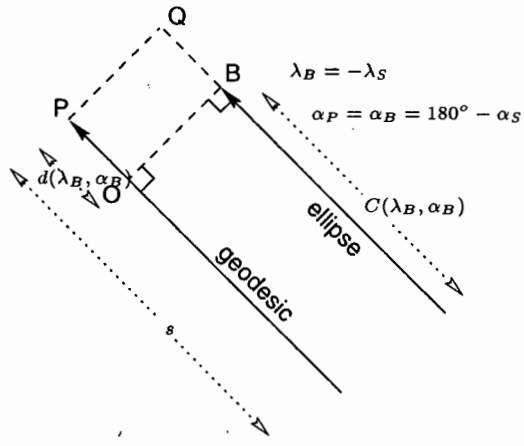

Figure 3.2: Close up view of the antipodal region.

From Figure 3.2 and using the Longuet-Higgins approximation, the distance traveled along the geodesic path at a particular time, P say, is the same as the distance traveled along the ellipse to Q, where PQ is perpendicular to both the ellipse and the geodesic curve. The distance SP is referred to as s and at any given time is fixed.

Thus using the Longuet-Higgins approximation and Figure 3.2, the geometric distance discrepancy function, d_G, which is the distance OP, on a spheroidal earth with a uniform ocean environment is defined as:

$$d_G(\lambda_B, \alpha_B) = s - C(\lambda_B, \alpha_B)$$

where: $C(\lambda_B, \alpha_B)$ $= \frac{1}{2}$ circumference of the ellipse.
$= SB = SO$ to the second order in f.

Longuet-Higgins (1990) derived $C(\lambda_B, \alpha_B)$ geometrically, using a radial coordinate system in the plane of the ellipse through the source, S; the center of the ellipsoid; and the point B. In this coordinate system r denotes the radial distance from the center of the ellipse and θ the rotational angle, clockwise from north.

Using this coordinate system r is defined by:

$$r = \left(\frac{\cos^2\theta}{a^2} + \frac{\sin^2\theta}{b^2}\right)^{-\frac{1}{2}} \tag{3.1}$$

Where: a and b are the semi-major and semi-minor axis, of the ellipse, respectively. The semi-major axis of the ellipse lies in the equatorial plane of the spheroidal earth. Thus a corresponds to the equatorial radius of the spheroidal earth and is the same for all ellipses. The semi-minor axis is dependent on the position of the source and the inclination of the ellipse but is not used in the following derivation. Thus precise details regarding b are not provided here, but can be found in Longuet-Higgins (1990).

The half circumference of the ellipse is defined by:

$$C(\lambda_B, \alpha_B) = \int_0^{\pi} r\, d\theta$$

which is expanded to:

$$C(\lambda_B, \alpha_B) = \pi.a - \frac{\pi}{2} f.a(1 - \frac{1}{2}\cos^2\lambda_B(1 - \cos 2\alpha_B))$$

So by definition:

$$d_G(\lambda_B, \alpha_B) = s - \pi.a + \frac{\pi}{2} f.a - \frac{\pi}{4} f.a\cos^2\lambda_B + \frac{\pi}{4} f.a\cos^2\lambda_B \cos 2\alpha_B$$

Or rather, defining d_G as a function of s as well as λ_B and α_B:

$$d_G(s, \lambda_B, \alpha_B) = A_G(s, \lambda_B) + B_G(\lambda_B).\cos 2\alpha_B$$

Where: $A_G(s, \lambda_B) = s - \pi.a + \frac{\pi}{2} f.a - \frac{\pi}{4} f.a\cos^2\lambda_B$
$B_G(\lambda_B) = \frac{\pi}{4}.f.a.\cos^2\lambda_B$

At this stage it is appropriate to consider the derived geometric distance discrepancy function, $d_G(s, \lambda_B, \alpha_B)$, in more detail. This function is written more conveniently (for this discussion, at least) as a scaled function:

$$\widehat{d_G}(s, \lambda_B, \alpha_B) := \frac{d_G(s, \lambda_B, \alpha_B)}{B_G(\lambda_B,)} = \frac{A_G(s, \lambda_B)}{B_G(\lambda_B)} + \cos 2\alpha_B = \widehat{A_G}(s, \lambda_B) + \cos 2\alpha_B \qquad (3.2)$$

Clearly, for a polar source, $B_G(\lambda_B) = B_G(\pm\frac{\pi}{2}) = 0$, the description of $\widehat{d_G}(s, \lambda_B, \alpha_B)$ is not defined, but logistically a polar source is not a practical option either. Thus for all non-polar sources, $B_G(\lambda_B)$ provides an appropriate scale for $d_G(s, \lambda_B, \alpha_B)$ and $A_G(s, \lambda_B)$ within the antipodal region.

Now for a known source, $B_G(\lambda_B)$ is constant and $\widehat{A_G}(s, \lambda_B)$ varies in s only, since λ_B is known. Since the second term of the function $\widehat{d_G}(\alpha_B)$ is always $+\cos 2\alpha_B$, this family of curves is referred to as the '$+\cos 2\alpha$ family' of curves in future sections of this work. A number of polar plots of $\widehat{d_G}$ over the azimuthal range $\alpha \in [0^o; 360^o]$ are considered below, in order to get a sense of the character of the function.

The most straightforward plot of the scaled distance discrepancy function occurs when $\widehat{A_G}(s, \lambda_B) = 0$ or $s = \pi.a - \frac{\pi}{2} f.a + \frac{1}{4} f.a\cos^2\lambda_B$, which means that:

$$\widehat{d_G}(s, \lambda_B, \alpha_B) = \cos 2\alpha_B$$

This particular function is used frequently in the Chapters which follow and is referred to as the 'special case' geometric distance discrepancy function, $\widehat{d_{G0}}(\alpha_B)$. The graph produced by this function, for the complete azimuthal range, $\alpha_B \in [0^o; 360^o]$, is shown in Figure 3.3. Alongside the graph a table showing values of $\widehat{d_{G0}}(\alpha_B)$ for particular values of α_B is included.

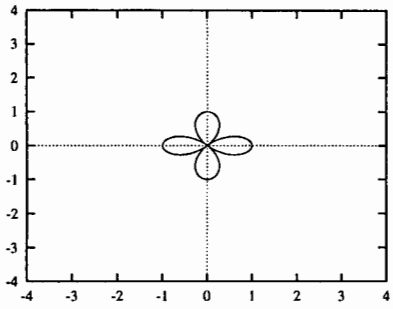

α_B	$\widehat{d_{G0}}(\alpha_B)$	α_B	$\widehat{d_{G0}}(\alpha_B)$
0^o	1	180^o	1
45^o	0	225^o	0
90^o	-1	270^o	-1
135^o	0	315^o	0

Figure 3.3: Plot of $\widehat{d_{G0}}(\alpha_B)$ and the associated value table.

The graph produced in Figure 3.3 is four-rose curve plot, also known as a quadrifolium (Lockwood 1961). In general a rose-curve can be described by a function of the form $r = \cos n\theta$. If n is even, as is the case here, the curve will have '$2n$ loops' and if n is odd, the curve will have 'n loops' (Spiegel 1968). In passing, the equation for $r = \sin n\theta$ has a similar curve obtained by rotating the axially aligned '$\cos n\theta$' curve by 45^o (Spiegel 1968). The value $n = 2$ indicates that indeed $\widehat{d_{G0}}(\alpha_B)$ is a four-looped quadrifolium.

The graph and table in Figure 3.3 indicate that the initial position of the graph, on the positive $y - axis$ since α_B is measured clockwise from north, is $\widehat{d_{G0}}(0^o) = 1$. As α_B increases from 0^o to 45^o so the values of $\widehat{d_{G0}}(\alpha_B)$ decrease from 1 to 0, forming a 'half-loop' in the north-east quadrant of the graph. This discussion is completed with the aid of the following octant table, Table 3.1. Each of the eight figures in the table represent the function $\widehat{d_{G0}}(\alpha_B)$ for the accumulated azimuthal octants. Thus the first graph pertains to the azimuthal range $\alpha_B \in [0^o; 45^o]$, for the second graph $\alpha_B \in [0^o; 90^o]$ and so on.

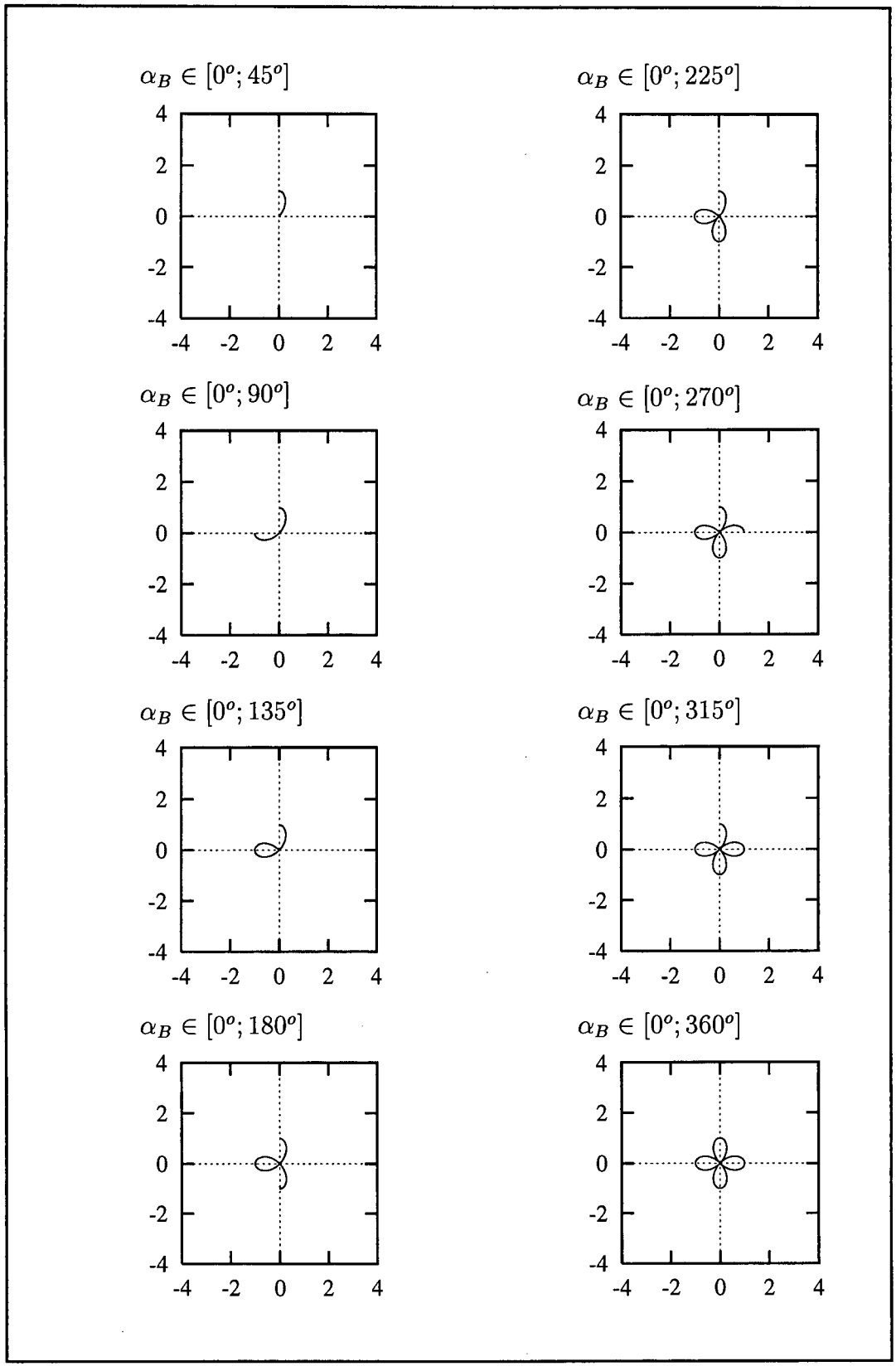

Table 3.1: Octant table for $\widehat{d_{G0}}(\alpha_B)$.

The octant table shows that the function $\widehat{d_{G0}}(\alpha_B)$ traces a path in a clockwise direction throughout the azimuthal range. The octant table also clearly demonstrates that each azimuthal range of 45^o corre-

sponds to half a loop of the quadrifolium curve. The azimuthal ranges $[315^o; 45^o]$; $[135^o; 225^o]$; $[225^o; 315^o]$ and $[45^o; 135^o]$ respectively yield the north; south; east and west loops of the quadrifolium curve.

Notice that positive values of $\widehat{d_{G0}}(\alpha_B)$ occur in the azimuthal ranges $\alpha_B \in [315^o; 45^o]$ and $\alpha_B \in [135^o; 225^o]$. While negative values of $\widehat{d_{G0}}(\alpha_B)$ occur in the azimuthal ranges $\alpha_B \in [45^o; 135^o]$ and $\alpha_B \in [225^o; 315^o]$. This means that, in the ranges $\alpha_B \in [45^o; 135^o]$ and $\alpha_B \in [225^o; 315^o]$, the ray points that $\widehat{d_{G0}}(\alpha_B)$ describe are not yet at the point B, which is at the center of the antipodal region. While in the ranges $\alpha_B \in [315^o; 45^o]$ and $\alpha_B \in [135^o; 225^o]$ the ray points are beyond the center of the antipodal region.

Now $\widehat{d_{G0}}(\alpha_B)$ is a specific member of the $\widehat{d_G}(\alpha_B)$ family of curves, which corresponds to the value of $\widehat{A_G} = 0$. The family members of $\widehat{d_G}(\alpha_B)$ with $\widehat{A_G} < 0$ correspond to points approaching the antipodal region, while those with $\widehat{A_G} > 0$ correspond to points beyond. Thus $\widehat{A_G}$ can be used as a discrete proxy to distance through the antipodal region, and $\widehat{A_G} = 0$, which is the special case, can be taken as the proxy origin.

A number of specific functions of $\widehat{d_G}(\alpha_B)$ are considered here, particularly for the integer values of $\widehat{A_G} = -3; -2; \ldots; +2; +3$, which are referred to as the $\widehat{d_{G-3}}(\alpha_B); \widehat{d_{G-2}}(\alpha_B); \ldots; \widehat{d_{G+2}}(\alpha_B); \widehat{d_{G+3}}(\alpha_B)$ functions within the $\widehat{d_G}(\alpha_B)$ family. The graphs of these functions are plotted below in Figure 3.4, for the full azimuthal range. The relevant value table is included in the plot.

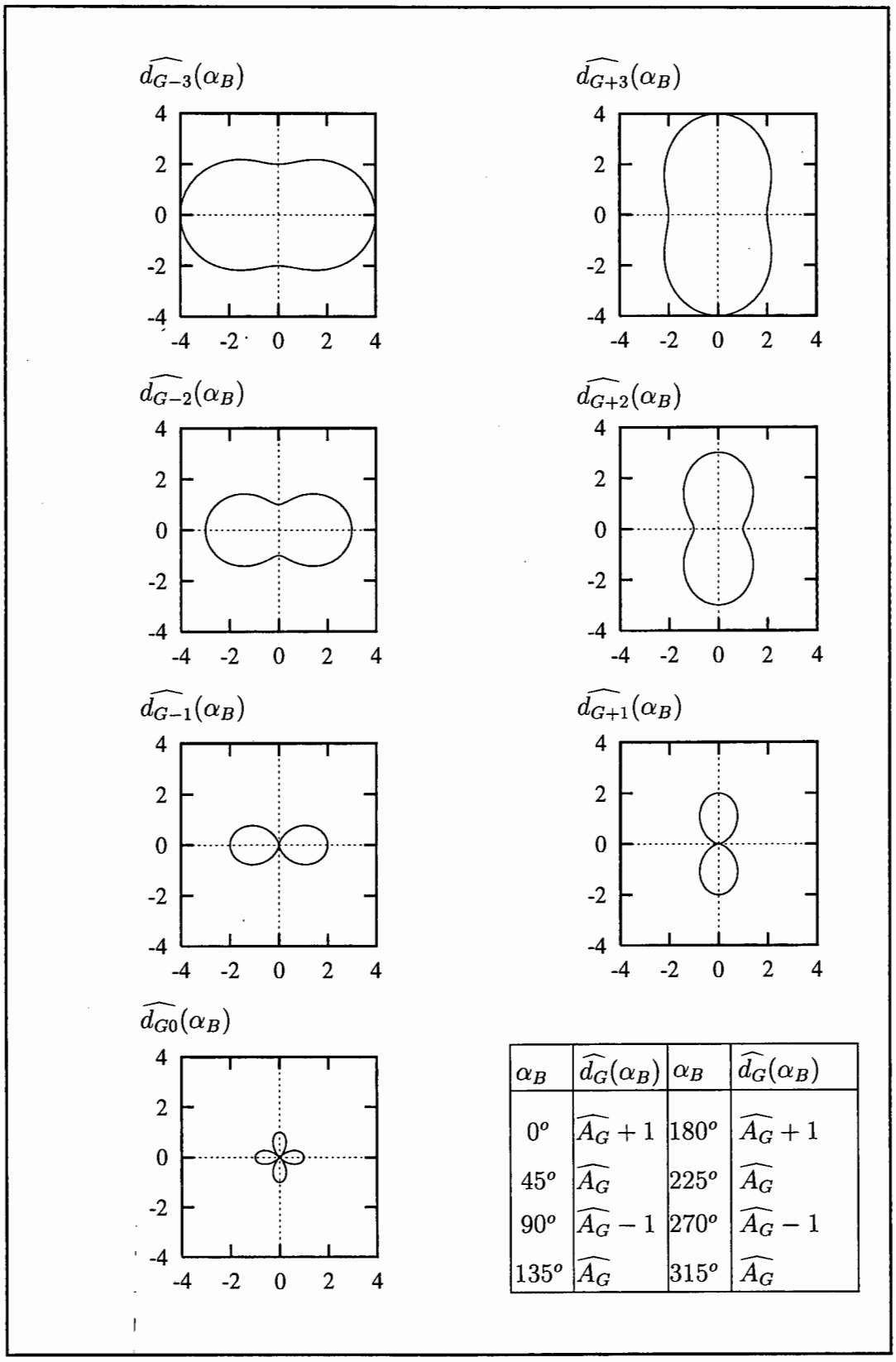

α_B	$\widehat{d_G}(\alpha_B)$	α_B	$\widehat{d_G}(\alpha_B)$
0^o	$\widehat{A_G}+1$	180^o	$\widehat{A_G}+1$
45^o	$\widehat{A_G}$	225^o	$\widehat{A_G}$
90^o	$\widehat{A_G}-1$	270^o	$\widehat{A_G}-1$
135^o	$\widehat{A_G}$	315^o	$\widehat{A_G}$

Figure 3.4: Polar plot and value table for $\widehat{d_G}(\alpha_B)$, for the integer values of $\widehat{A_G}(\alpha_B) = -3; -2; \ldots; +2; +3$.

The curves for $\widehat{A_G} < 0$, have a west-east orientation and those beyond the proxy origin have a north-south orientation. This is because rays propagating over the poles (that is from the north or south) have a shorter path, due to the ellipsoidal form of the earth, and thus approach the antipodal region more quickly than those approaching the region along the western or eastern equatorial path. Similarly for those rays beyond the antipodal region the rays propagating towards the poles approach the poles more quickly, because of the shorter propagation distance involved than those rays propagating along the equator.

It is interesting to notice that the function $\widehat{d_G}(\alpha_B)$ passes through a series of phases as the ray approaches or departs from the proxy origin. It appears that for $|\widehat{A_G}| > 1$ the function has an oval like curve known as the 'Ovals of Cassini' or a 'Cassinian Oval'. The locus of the curve is described as a point such that the product of its distances from two fixed points ($2a$ apart) is a constant b^2 (Spiegel 1968). It has a generalized polar equation of the form $r^4 + a^4 - 2a^2r^2\cos 2\theta\ b^4$. If $b < a$ then the curve is represented by two separate ovals, however for $b > a$ the curve is a single oval as was the case here for the relevant $\widehat{d_G}(\alpha_B)$ curves. When $b = a$ the Cassinian Oval reduces to the special curve of a lemniscate, which is the case here for $|\widehat{A_G}| = 1$.

The lemniscate is also referred to as the lemniscate of Bernoulli, because in 1694 Bernoulli wrote an article regarding the figure eight curve, which he called the lemniscus (Lockwood 1961). At that stage Bernoulli did not know that the lemniscate was a special case of the Cassinian Oval, his primary interest was analytical and laid the foundations for later works on elliptic functions. The generalized polar equation for a lemniscate is: $r^2 = a^2\cos 2\theta$, and in rectangular coordinates is: $(x^2 + y^2)^2 = a^2(x^2 - y^2)^2$. The area of one of the loops is easily determined as a^2 (Spiegel 1968).

Finally for $\widehat{A_G} = 0$, the function $\widehat{d_G}(\alpha_B)$, reduces to the quadrifolium function discussed in detail with regard to the special case geometric distance discrepancy function $\widehat{d_{G0}}(\alpha_B)$.

Notice that the functions $\widehat{d_{G-3}}(\alpha_B)$ and $\widehat{d_{G-2}}(\alpha_B)$ are negative throughout the azimuthal range, indicating that the ray points they represent are not at the center of the antipodal region yet. However, the $\widehat{d_{G-1}}(\alpha_B)$ function is negative throughout the azimuthal range except at $\alpha_B = 0^o$ or $\alpha_B = 180^o$, where $\widehat{d_{G-1}}(\alpha_B) = 0$. This indicates that those two polar rays are at the center of the antipodal region, while others are still approaching it.

The $\widehat{d_{G0}}(\alpha_B)$ function is positive throughout the azimuthal ranges $\alpha_B \in [315^o; 45^o]$ and $\alpha_B \in [135^o; 225^o]$, the rays are still approaching the center of the antipodal region, B. For the zero functions: $\widehat{d_{G0}}(45^o)$; $\widehat{d_{G0}}(135^o)$; $\widehat{d_{G0}}(225^o)$ and $\widehat{d_{G0}}(315^o)$ the ray points are at B. Throughout the remainder of the azimuthal range $\widehat{d_{G0}}(\alpha_B)$ is positive, which indicates that the ray points are beyond the center of the antipodal region.

The function $\widehat{d_{G+1}}(\alpha_B)$ is zero for $\alpha_B = 90^o$ or $\alpha_B = 270^o$, which indicates that those rays are at the center of the antipodal region. While all other values of $\widehat{d_{G+1}}(\alpha_B)$ are positive and thus beyond the center of the antipodal region. Also, $\widehat{d_{G+2}}(\alpha_B)$ and $\widehat{d_{G+3}}(\alpha_B)$ are positive throughout the azimuthal range, indicating that the ray points are all beyond the center of the antipodal region.

In order to discuss the orientation of the $\widehat{d_G}(\alpha_B)$ family of curves the relevant octant table is presented below in Table 3.2.

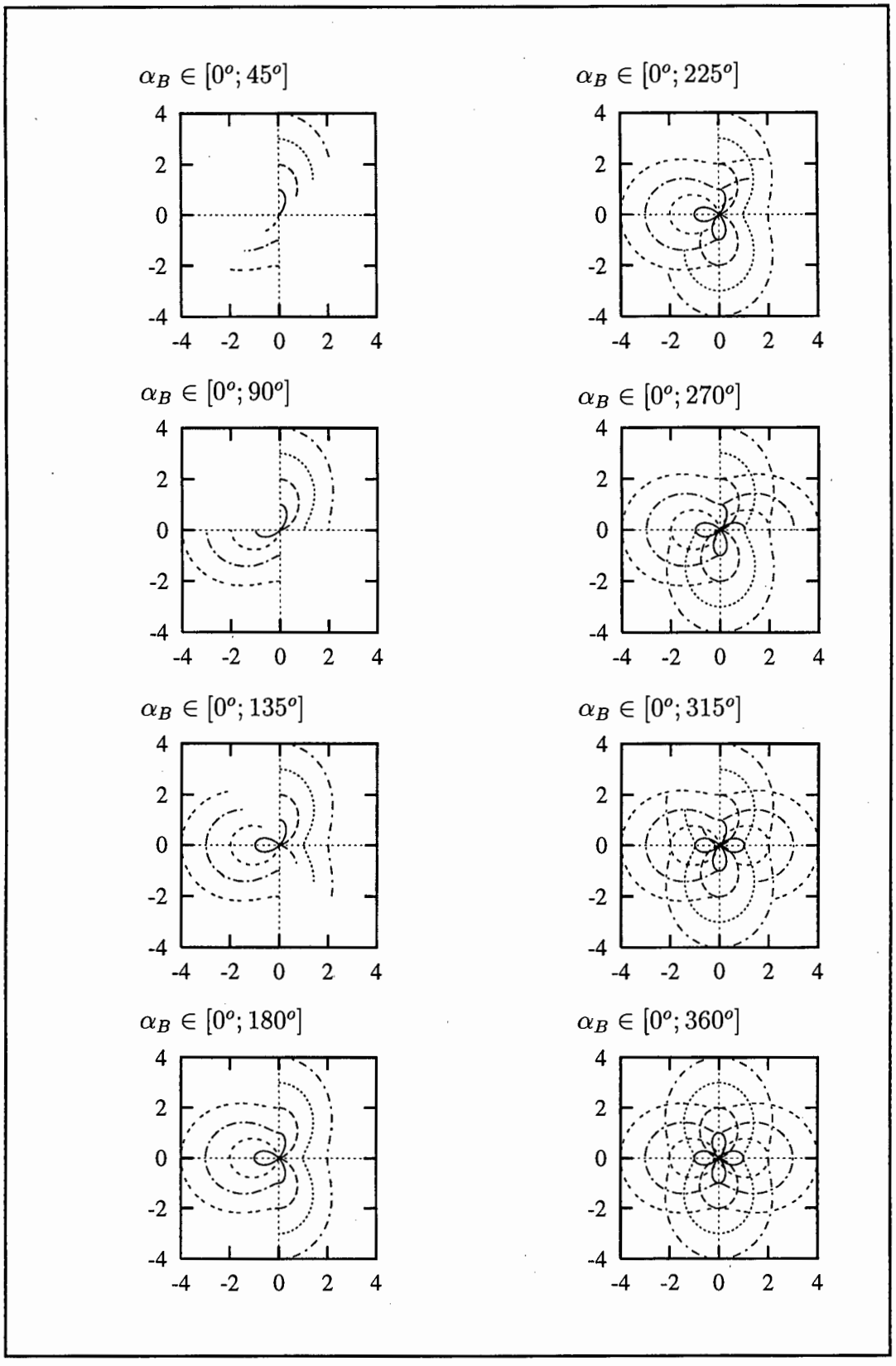

Table 3.2: Octant table for $\widehat{d_G}(\alpha_B)$, for the integer values of $\widehat{A_G}(\alpha_B) = -3; -2; \ldots; +2; +3$.

The octant table shows that all the functions in the $\widehat{d_G}(\alpha_B)$ family have a clockwise orientation throughout the azimuthal range. This is true even for the $\widehat{d_{G\pm1}}(\alpha_B)$ which, when viewed for the whole

azimuthal range appears to 'cross-over' at the center of the figure eight, but in actual fact the functions merely 'bounce' onwards, without changing bearing. Also, regarding the lemniscate, a 90^o azimuthal range contributes to the half loop as opposed to a 45^o range for the quadrifolium.

The octant table demonstrated that for successive values of $\widehat{A_G}$ the functions approaches and then departs from $\widehat{d_G} = 0$ along a straight line. An example of where this occurs is in the first graph of the octant table. For the ray inclined at $\alpha_B = 0^o$, $\widehat{d_G}$ increases steadily from $\widehat{d_{G-3}} = -2$ to $\widehat{d_{G+3}} = +2$ whilst for $\alpha_B = 45^o$, $\widehat{d_G}$ increases from -3 to $+3$. This is also evident from the table in Figure 3.4.

3.2 Refractive Approach

In this Section the refractive distance discrepancy function is determined for a spherical earth rather than a spheroidal earth, with a range dependent sound speed environment imposed upon it. The latitudinal variation is represented by the sound slowness function, $S(\lambda)$, which is defined in Section 2.2. Again as mentioned in Section 1.1 and as in the geometrical approach, a particular antipodal point does not exist, because of the inclusion of a sound speed variability, which results in refractive effects and propagation path perturbations.

The refractive distance discrepancy function is determined by establishing travel times at a fixed distance along each ray propagating from the source. In this Section much use is made of the work of Munk, Worcester, and Wunsch (1995), particularly their Section 2.8 entitled "Ray Perturbations".

Since this approximation occurs on a spherical earth it is appropriate to refer to the antipodal point, which is defined as A. In Figure 3.5 below, the refracted ray path (dashed path) and the great semi-circle path (solid path), between the source, $S(\lambda_S, \phi_S)$, and the antipodal point $A(-\lambda_S, 180^o + \phi_S)$, on a spherical earth are presented. The refracted ray path lies between the source, $S(\lambda_S, \phi_S)$, and a point P, which is positioned in the antipodal region, with the same latitude as the antipodal point, A. Thus the coordinates of the point P are $(-\lambda_S; \phi_P)$.

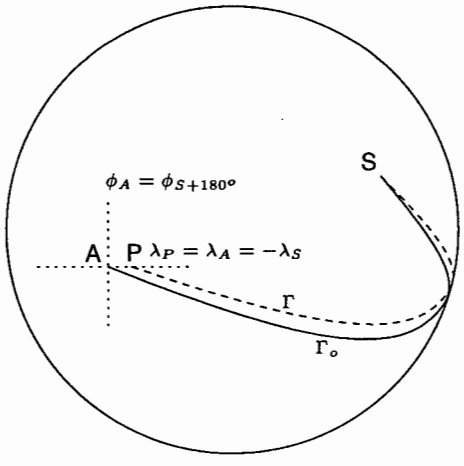

Figure 3.5: The path along the refracted great semi-circle (dashed) path, Γ, and the great circle (solid) path, Γ_o, between S and P and S and A respectively.

In the previous figure, Figure 3.5 a point, P, in the region of the antipode is selected, lying on the refracted great semi-circle with a complementary latitude to that of the source. By the definition of P:

$$\begin{aligned} \lambda_P &= -\lambda_S \\ \Rightarrow \cos\lambda_P &= \cos\lambda_S \end{aligned}$$

Also, since $S(\lambda)$ is an even function:

$$S(\lambda_P) = S(\lambda_S)$$

Using Snell's law on a sphere, where sound-speed is a function of latitude only:

$$\begin{aligned} S(\lambda).\cos\lambda.\sin\alpha &= constant \\ \Rightarrow S(\lambda_P).\cos\lambda_P.\sin\alpha_P &= S(\lambda_S).\cos\lambda_S.\sin\alpha_S \\ \Rightarrow \sin\alpha_P &= \sin\alpha_S \end{aligned}$$

This relationship, which is an expression of Snell's Law on a spherical earth with latitudinal sound speed variation, holds for all refracted ray paths, Γ.

The refracted great semi-circle distance from S to P is given by:

$$\begin{aligned} \int_S^P ds &= \int_S^P \frac{R}{\cos\alpha} d\lambda \\ &= \int_S^P \frac{R.S(\lambda).\cos\lambda}{\sqrt{(S(\lambda)\cos\lambda)^2 - (S(\lambda_S)\cos\lambda_S\sin\alpha_S)^2}} d\lambda \end{aligned}$$

Previously, in Section 1.2, a small function ϵ, defined as the refractive index was introduced. It is possible to approximate the preceding integral to the first order in small quantities of ϵ, say, and evaluate. However a 'neater' Fermat approach is taken.

In this scenario sound propagated along a refracted ray path, Γ, which is refracted away from the great semi-circle path, Γ_o, according to the sound slowness function, $S(\lambda)$, is considered.

For a given ray the associated refracted path, Γ, and great semi-circle path, Γ_o, have the same initial azimuthal angle at the source. The difference between the two paths is the different travel times as they propagate through slightly different sound slowness environments.

The travel time, T, for a particular refracted ray is defined as the integral of the sound slowness along the refracted ray path, Γ. Thus:

$$T = \int_\Gamma S ds$$

Now the refracted ray path, Γ is slightly perturbed from the great semi-circle path, Γ_o, and therefore:

$$T = \int_\Gamma S ds \simeq \int_{\Gamma_o} S ds$$

This approximation corresponds to the Longuet-Higgins approximation in the previous section, Section 3.1. For a given great circle path, Γ_o, a good approximation to T can be found, even though the

ray path, Γ, is unknown - since integration occurs along the known great semi-circle path.

The comparison between slight changes in $S(\lambda)$ on Γ_o as against Γ, are balanced by the slight change in length between Γ_o and Γ according to Fermat's principle. Thus Fermat's approximation means that:

$$\int_{\Gamma} Sds - \int_{\Gamma_o} Sds \simeq 0$$

This means that a good approximation for T can be calculated for every path propagating from a given source.

Now in order to compare different values of T it is necessary to define a standard or reference travel time T_o. T_o is defined as the integral along the great semi-circle path for the constant sound speed, S_o. S_o is a preselected reference sound slowness throughout the world oceans and was chosen, in the previous chapter to be the 45^o value of $S(\lambda)$. Thus the great semi-circle path, Γ_o yields:

$$T_o = \int_{\Gamma_o} S_o ds = \pi.R.S_o$$

Thus a comparable function, ΔT is written using the form:

$$\begin{aligned} \Delta T &= T - T_o \\ &= \int_{\Gamma} Sds - \int_{\Gamma_o} S_o ds \\ &= \int_{\Gamma} Sds - \int_{\Gamma_o} Sds + \int_{\Gamma_o} Sds - \int_{\Gamma_o} S_o ds \end{aligned}$$

Using the Fermat approximation:

$$\Delta T \simeq \int_{\Gamma_o} (S - S_o) ds = \int_{\Gamma_o} \Delta S ds$$

This indicates that the change in travel time between sound propagating along a refracted ray path, Γ and a great circle path, Γ_o, are found by determining the integral of the variation in sound slowness along the great circle path, Γ_o.

The extreme latitude, λ_E, introduced in Section 1.3, is expressed by:

$$S(\lambda_E).\cos\lambda_E = S(\lambda_S).\cos\lambda_S.\sin\alpha_S$$

Now along the great circle path, Γ_o, Snell's law is reduced to:

$$\cos\lambda_E = \cos\lambda_S.\sin\alpha_S$$

The detailed calculation is:

$$\begin{aligned} \Delta T &= 2\int_S^A \Delta S ds \\ &= 2\int_0^{\lambda_E} \Delta S(\lambda).\frac{R}{\cos\alpha} d\lambda \\ &= 2.R\int_0^{\lambda_E} \frac{\Delta S(\lambda).\cos\lambda}{(\cos^2\lambda - \cos^2\lambda_E)^{\frac{1}{2}}} d\lambda \\ &= 2.R\int_0^{\lambda_E} \frac{\Delta S(\lambda)}{\sqrt{1 - (\frac{\sin\lambda}{\sin\lambda_E})^2}} d(\frac{\sin\lambda}{\sin\lambda_E}) \end{aligned}$$

Now q is introduced, where q is given by $\sin q = \frac{\sin\lambda}{\sin\lambda_E}$, then:

$$\Delta T = 2.R\int_0^{\frac{\pi}{2}} \Delta S(q)dq$$

The relative travel perturbation is a transformed mean of the relative slowness perturbation, with the transform from latitude given by:

$$\sin q = \frac{\sin\lambda}{\sin\lambda_E}$$

It is convenient to transform ΔT into the refractive distance discrepancy function, d_R, to ease determining the wavefront. d_R is defined as the distance traveled by a ray, beyond the reference distance at a specific reference time on a spherical earth, within a range dependent environment. Thus d_R is negative for rays approaching the antipode and positive for rays that are propagating beyond the antipode. The refractive distance discrepancy function is defined in terms of the antipodal point, A, as:

$$d_R(\lambda_A, \alpha_A) = -\frac{\Delta T}{S_o}$$
$$= -\frac{2R}{S_o}\int_0^{\frac{\pi}{2}} \Delta S(q)dq$$

(With $\sin q = \frac{\sin\lambda}{\sin\lambda_E}$ as the transformed variable).

At this stage it is important to examine the detail of the refractive distance discrepancy function, which is dependent on the sound slowness function determined in the previous Chapter, in Section 2.2, where the model sound slowness perturbation was defined as:

$$\Delta S(\lambda) = -\mathcal{A}\cos 2\lambda = -\mathcal{A}(2.\cos^2\lambda - 1)$$

For the transformed variable:

$$\sin\lambda = \sin\lambda_E.\sin q$$
$$\Rightarrow \cos\lambda = \sqrt{1 - \sin^2\lambda_E.\sin^2 q}$$

Notice that for a given great circle, for any source on that great circle the extreme latitude, λ_E is constant. It follows that for:

$$\Delta S(q) = -\mathcal{A}(2(1 - \sin^2\lambda_E.\sin^2 q) - 1)$$
$$\int_0^{\frac{\pi}{2}} \Delta S(q)dq = -\mathcal{A}\int_0^{\frac{\pi}{2}} (1 - 2\sin^2\lambda_E.\sin^2 q)dq$$
$$= -\mathcal{A}\frac{\pi}{2} + 2\mathcal{A}\sin^2\lambda_E\int_0^{\frac{\pi}{2}} \sin^2 q dq$$
$$= -\mathcal{A}\frac{\pi}{2} + 2\mathcal{A}\sin^2\lambda_E[\frac{1}{2}q - \frac{1}{4}\sin 2q]_0^{\frac{\pi}{2}}$$
$$= -\mathcal{A}\frac{\pi}{2} + 2\mathcal{A}\sin^2\lambda_E[\frac{\pi}{4}]$$
$$= -\mathcal{A}\frac{\pi}{2} + \frac{\pi}{2}\mathcal{A}\sin^2\lambda_E$$
$$\Rightarrow \int_0^{\frac{\pi}{2}} \Delta S(q)dq = -\mathcal{A}\frac{\pi}{2}\cos^2\lambda_E$$

The nature of λ_E described in Section 1.3 indicates that $\int_0^{\frac{\pi}{2}} \Delta S(q)dq = -\mathcal{A}\frac{\pi}{2}\cos^2\lambda_E$ holds true for any source on a particular path of a specific great circle.

Thus, for a specific great circle, ΔT is written in the following form:

$$\begin{aligned}\Delta T &= 2R\int_0^{\frac{\pi}{2}} \Delta S(q) \\ &= -\pi R\mathcal{A}\cos^2\lambda_E\end{aligned}$$

A realistic interpretation of T_o is necessary in order to draw realistic comparisons between T and T_o. At this stage it is necessary to consider an interpretation of T_o that is consistent with a reasonable understanding of the physical environment.

In Chapter 2 sound slowness is described using the form:

$$S = S_o + \Delta S$$

Similarly T is defined in this way:

$$T = T_o + \Delta T$$

Thus:

$$\begin{aligned}T &= T_o - \frac{A.T_o}{S_o}\cos^2\lambda_E \\ \Rightarrow T &= \pi RS_o - \pi R\mathcal{A}\cos^2\lambda_E\end{aligned}$$

Consider for a given source, the ray that has $\lambda_E = 90^o$, this ray is clearly the ray which propagates through the pole, that has an initial azimuthal angle of 0^o and is referred to here as the 'polar ray'. From the definition of λ_E in Section 1.3 every source for a particular ray has a great circle route through the pole between the source and the antipode.

For the polar ray $\lambda_E = 90^o$ and therefore $\Delta T = 0$ and $T = \pi RS_o$. And, by definition the polar ray has a travel time equivalent to the reference travel time T_o. This means that

$$T_{polar} = \int_{\Gamma_o} Sds = \pi RS_o = \int_{\Gamma_o} S_o ds = T_o$$

And the reference travel time corresponds to the travel time along the polar path for all sources on a given great circle.

From the definition of T:

$$T = T_o + \Delta T = \pi RS_o - \pi RS_o\mathcal{A}\cos^2\lambda$$

it follows, analytically, that $T \leq T_o$ for all values of α_S. For $\alpha_S = 0^o$ or $\alpha_S = 270^o$, $\lambda_E = \pm 90^o$ and $T = T_o$. All other rays, with $\alpha_S \neq 0^o$ or $\alpha_S \neq 270^o$, for a particular source have a slower travel time than that of the polar ray. This analytical result corresponds to the realistic understanding that the polar ray propagates through the coolest waters and experiences the region of maximum sound slowness and therefore has the maximum travel time for all possible rays from a given source.

Consequently, a reasonably realistic interpretation of the reference travel time is the travel time associated with the polar path. The polar path is theoretically achievable for all sources and is therefore a path that can easily be used for comparative purposes.

Returning to the integral $\int_0^{\frac{\pi}{2}} \Delta S(q)dq$, which is rewritten here in terms of the presumed antipodal point position angles: λ_A and α_A:

$$\begin{aligned}\int_0^{\frac{\pi}{2}} \Delta S(q)dq &= -\mathcal{A}\frac{\pi}{2}\cos^2\lambda_A.\sin^2\alpha_A \\ &= -\mathcal{A}\frac{\pi}{4}\cos^2\lambda_A(1-\cos 2\alpha_A)\end{aligned}$$

Therefore the refractive distance discrepancy function is derived as:

$$\begin{aligned}d_R(\lambda_A,\alpha_A) &= -\frac{\Delta T}{S_o} \\ &= -\frac{2R}{S_o}.\int_0^{\frac{\pi}{2}} \Delta S(q)dq \\ &= \frac{2R}{S_o}.\mathcal{A}\frac{\pi}{4}\cos^2\lambda_A(1-\cos 2\alpha_A) \\ \Rightarrow d_R(\lambda_A,\alpha_A) &= \frac{\pi R\mathcal{A}}{2S_o}\cos^2\lambda_A(1-\cos 2\alpha_A)\end{aligned}$$

This function can be related to the geometric distance discrepancy function in the previous Section, Section 3.1, if it is written in the form:

$$d_R(\lambda_A,\alpha_A) = A_R(\lambda_A) - B_R(\lambda_A)\cos 2\alpha_A$$

Where:

$$A_R(\lambda_A) = \frac{\pi R\mathcal{A}}{2S_o}\cos^2\lambda_A = B_R(\lambda_A)$$

If the function d_R is written in the more convenient form, as d_G was in Section 3.1, as a scaled function, with B_R as the scaling factor, then:

$$\widehat{d_R}(\lambda_A,\alpha_A) := \frac{d_R(\lambda_A,\alpha_A)}{B_R(\lambda_A)} = \frac{A_R(\lambda_A)}{B_R(\lambda_A)} - \cos 2\alpha_A = 1-\cos 2\alpha_A \tag{3.3}$$

As for the scaling factor $B_G(\alpha_A)$ in Section 3.1, for a polar source $B_R(\lambda_A) = B_R(\pm\frac{\pi}{2}) = 0$, the description of $\widehat{d_R}(s,\lambda_A,\alpha_A)$ is not defined, but again, logistically a polar source is not a practical option. Thus for all non-polar sources, $B_R(\lambda_A)$ provided an appropriate scale for $d_R(s,\lambda_A,\alpha_A)$ and $A_R(s,\lambda_A)$ within the antipodal region.

$\widehat{d_R}(\alpha_A)$ is invariant with respect to the distance parameter s, for a given latitude, thus the refractive distance discrepancy function is the same for all approaches to and from the antipodal region. The graph produced for this plot and its associated Value Table, are shown below in Figure 3.6.

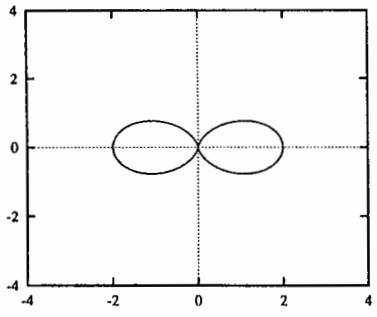

α_A	$\widehat{d_R}(\alpha_A)$	α_A	$\widehat{d_R}(\alpha_A)$
0^o	0	180^o	0
45^o	1	225^o	1
90^o	2	270^o	2
135^o	1	315^o	1

Figure 3.6: Polar plot and value table of $\widehat{d_R}(\alpha_A)$.

The graph in Figure 3.6 is a member of the '$-\cos 2\alpha$ family', and clearly has the form of a lemniscate. The generalized form of a lemniscate curve was described with respect to the function $\widehat{d_{G\pm1}}(\alpha_B)$. In fact, this curve has exactly the same form as that of $\widehat{d_{G-1}}(\alpha_B)$, however the differences become apparent when considering the octant table for $\widehat{d_R}(\alpha_A)$, which is provided below in Table 3.3.

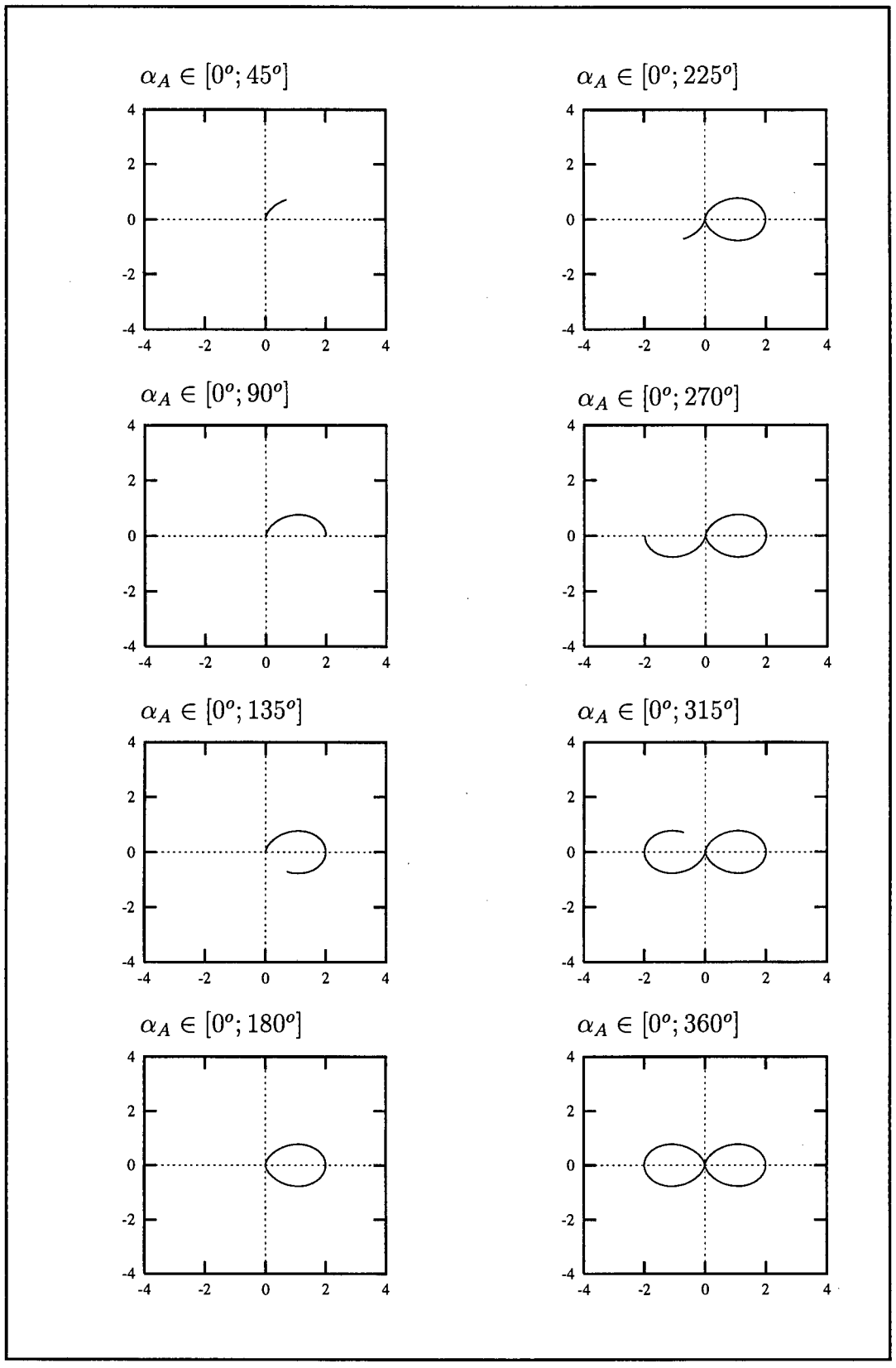

Table 3.3: Octant table for $\widehat{d_R}(\alpha_A)$.

This particular lemniscate has an initial point $\widehat{d_R}(0^o) = 0$, the same as that of $\widehat{d_{G-1}}(\alpha_B)$. From Table 3.3 for the azimuthal range $\alpha_A \in [0^o; 45^o]$ the function $\widehat{d_R}(\alpha_A)$ increases from 0 to 1. Continuing

in this way throughout the azimuthal range indicates that for $\alpha_A \in [0^o; 90^o]$ and $\alpha_A \in [180^o; 270^o]$ the function $\widehat{d_R}(\alpha_A)$ is increasing, otherwise $\widehat{d_R}(\alpha_A)$ was decreasing. Again the octant table demonstrates that even though the graph for the total azimuthal range appears to 'cross-over' at the origin, the graph in fact does not but continues with a clockwise orientation throughout the azimuthal range.

The functions $\widehat{d_R}(\alpha_A)$ and $\widehat{d_{G-1}}(\alpha_B)$ have the same initial positions and clockwise orientation, however the functions follow different paths throughout their ranges. The functions $\widehat{d_R}(\alpha_A)$ initializes at zero and the path of the function moves into the north-east quadrant, while the path of the $\widehat{d_{G-1}}(\alpha_B)$ also initializes at the origin progresses into the south-west quadrant. Consequently it can be said that these two functions are offset from each other by 180^o.

Notice, also, that $\widehat{d_R}(\alpha_A)$ is positive throughout the azimuthal range, except for $\alpha_A = 0^o$ or $\alpha_A = 180^o$, where $\widehat{d_R}(\alpha_A) = 0$. Thus, throughout the azimuthal range the ray points associated with $\widehat{d_R}(\alpha_A)$ are beyond the antipodal point, except at $\alpha_A = 0^o$ or $\alpha_A = 180^o$ where the associated ray points are positioned at the antipodal point.

Chapter 4

The Family of Wave Fronts

In the previous chapter a ray approach was used to determine the distance discrepancy function under certain physical assumptions, while in this chapter it is necessary to use a wavefront approach to determine the arrival pattern of sound rays as they advance towards the antipodal region. The purpose of this chapter is to determine the family of wavefronts, where a wavefront is defined as the envelope of lines perpendicular to the approaching rays at a particular time, associated with a distance discrepancy function, $d(\alpha)$.

Throughout this chapter, and the remainder of this thesis, the antipodal point refers either to the center of the antipodal region or the antipodal point, under the geometric and refractive assumptions respectively. Thus the parameter α, in this chapter and the remainder of this thesis, refers to the azimuthal angle at the antipodal point, which in the previous chapter has a subscript referring to α_B and α_A for the geometric and refractive assumptions respectively. The subscript is removed in this chapter because of the more generalized nature of the derivation. However, when applying the derivation to the specific distance discrepancy functions that were derived in the previous chapter then α refers to either the center of the antipodal region or the antipodal point, depending on the relevant assumption and the subscripts α_B and α_A are inferred.

In the first section, Section 4.1, a technique is developed for determining the family of wavefronts associated with the advancing rays at a particular time, where the rays are advancing according to a defined distance discrepancy function, $d(\alpha)$. The derived method, for a generalized wavefront function, is a systematic one which results in a set of parametric equations into which a specific distance discrepancy function can be substituted in order to determine the associated family of wavefronts.

In order to demonstrate the derived wavefront technique the wavefronts associated with the derived distance discrepancy functions in Chapter 3, the geometric and the refractive distance discrepancy functions are established in Section 4.2. Initially the geometric assumption is considered and the geometric distance discrepancy function is substituted into the derived wave equations. The family of wavefronts associated with this function is produced and compares favorably with the family of wavefronts that were derived in Longuet-Higgins (1990). The procedure is repeated for the refractive assumption using the associated discrepancy function with pleasing results.

4.1 Derivation of Wavefront Equations

In this section a set of parametric equations are derived that are used to determine the family of wavefronts associated with a particular distance discrepancy function. The procedure is described here for a completely arbitrary distance discrepancy function, $d(\alpha)$, in order to provide generalized equations for the family of wavefronts. The derivation is presented here in order to validate the resulting equations and to provide completeness.

The derivation has a strong geometric emphasis and relies heavily on the work of Longuet-Higgins (1990). The following figure provides the notation that is used in the text and is necessary to the understanding of the derivation.

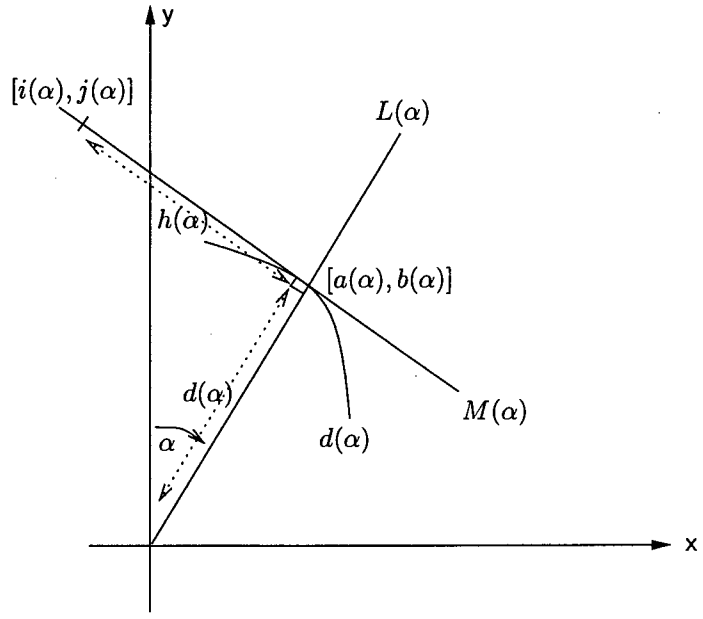

Figure 4.1: Introduction to the notation used to derive the equation of the wave fronts.

Consider Figure 4.1, which is constructed on a polar coordinate system, where α is the angle of rotation in a clockwise direction ranging from $[0^o; 360^o]$ and the zero axis is the positive vertical axis. A portion of the distance discrepancy function, $d(\alpha)$ is plotted using this coordinate system.

The derivation begins by expressing the distance discrepancy function in terms of Cartesian coordinates. The distance $d(\alpha)$ along the approximate path $L(\alpha)$, which is the same as the distance along the ray is considered. The equation for the straight line equation for $L(\alpha)$ is written as:

$$L(\alpha) := y = \tan(90 - \alpha).x$$

The point of intersection between $L(\alpha)$ and $d(\alpha)$ is established in Cartesian coordinates. The point of intersection represents the distance discrepancy function in Cartesian coordinates and is labeled $[a(\alpha); b(\alpha)]$ in Figure 4.1. The coordinates of the point are determined here:

$$[a(\alpha); b(\alpha)] := d(\alpha) \cap L(\alpha)$$

$$\Rightarrow a(\alpha) = d(\alpha).\cos(90-\alpha) = d(\alpha).\sin\alpha \tag{4.1}$$
$$b(\alpha) = d(\alpha).\sin(90-\alpha) = d(\alpha).\cos\alpha \tag{4.2}$$

The following stage in the derivation is to construct the straight line $M(\alpha)$ (refer to Figure 4.1) through the point $[a(\alpha), b(\alpha)]$ and perpendicular to the straight line $L(\alpha)$. Now at the point $[a(\alpha), b(\alpha)]$, by definition the straight line $L(\alpha)$ intersects with the distance discrepancy function, and as a result $L(\alpha)$ is parallel to the direction of the ray with azimuthal angle α. Consequently, the newly constructed straight line $M(\alpha)$ is perpendicular to the ray path. By definition of the wavefront the envelope of the lines $M(\alpha)$, for all α, provides the equation for the wavefront at the particular time that $d(\alpha)$ is plotted.

$$\begin{aligned} M(\alpha) \perp L(\alpha) \Rightarrow gradient &= \frac{-1}{\tan(90-\alpha)} \\ &= -\frac{\cos(90-\alpha)}{\sin(90-\alpha)} \\ &= -\frac{\sin(\alpha)}{\cos(\alpha)} \end{aligned}$$

The gradient of $M(\alpha)$ is known and a point on $M(\alpha)$, $[a(\alpha), b(\alpha)]$, was determined previously in equations 4.1 and 4.2. Hence an equation for $M(\alpha)$ is straightforward to determine.

$$\begin{aligned} M(\alpha) := y - b(\alpha) &= -\frac{\sin(\alpha)}{\cos(\alpha)}[x - a(\alpha)] \\ \Rightarrow \cos\alpha[y - b(\alpha)] &= -\sin(\alpha)[x - a(\alpha)] \end{aligned}$$

The question arises as to how far along the line $M(\alpha)$ must one proceed before the wavefront envelope created by the accumulated $M(\alpha)$ lines, for all α, is intersected. This point of intersection is referred to as $[i(\alpha), j(\alpha)]$ in Figure 4.1, thus:

$$\mathcal{W}(\alpha) := [i(\alpha); j(\alpha)]$$

The distance between $[a(\alpha), b(\alpha)]$ and $[i(\alpha), j(\alpha)]$ is referred to here as $h(\alpha)$ and is merely an unknown factor, which is added to both sides of the equation of $M(\alpha)$, so that:

$$\cos\alpha[y - b(\alpha) + h(\alpha).\sin\alpha] = -\sin\alpha[x - a(\alpha) - h(\alpha).\cos\alpha] \tag{4.3}$$

At this stage a function of the envelope of wavefront tangents is generated from known parameters and a point on this envelope is already defined as $[i(\alpha), j(\alpha)]$. It is known that a wavefront tangent has a gradient of the form: $\frac{j'(\alpha)}{i'(\alpha)}$, where $j'(\alpha) = \frac{\partial j(\alpha)}{\partial \alpha}$ and $i'(\alpha) = \frac{\partial i(\alpha)}{\partial \alpha}$. Also, the selected wavefront tangent passes through the point $[i(\alpha), j(\alpha)]$. Consequently, the wavefront tangent has an equation of the form:

$$i'(\alpha)[y - j(\alpha)] = j'(\alpha)[x - i(\alpha)]$$

This equation does not include a scaling factor and in order to generalize it both sides of the equation are multiplied by a factor $k(\alpha)$ say, and thus the equation for the generalized wavefront tangent becomes:

$$k(\alpha).i'(\alpha)[y - j(\alpha)] = k(\alpha).j'(\alpha)[x - i(\alpha)] \tag{4.4}$$

Now the envelope of the wavefront is defined by two distinct equations, that of equation 4.3 and equation 4.4. By systematically comparing the x and y components of these two equations the point $[i(\alpha), j(\alpha)]$ can be determined. In fact, matching the two equations, 4.3 and 4.4, gives:

$$i(\alpha) = a(\alpha) + h(\alpha).\cos\alpha$$
$$j(\alpha) = b(\alpha) - h(\alpha).\sin\alpha$$

But $a(\alpha)$ and $b(\alpha)$ have already been defined in equations 4.1 and 4.2 respectively and this means that $i(\alpha)$ and $j(\alpha)$ can be written in the form:

$$i(\alpha) = d(\alpha).\sin\alpha + h(\alpha).\cos\alpha$$
$$j(\alpha) = d(\alpha).\cos\alpha - h(\alpha).\sin\alpha$$

These equations clearly indicate that a point on the wavefront is constructed from two different distance components, one in the direction of the ray in terms of the distance discrepancy function, $d(\alpha)$, and the other perpendicular to the ray, which is referred to as $h(\alpha)$. Clearly, the function $k(\alpha)$ does not necessarily need to be known to determine the position of $[i(\alpha); j(\alpha)]$.

Continuing with the derivation, the equations for $i(\alpha)$ and $j(\alpha)$ are differentiated with respect to α, providing the equations:

$$i'(\alpha) = d'(\alpha).\sin\alpha + d(\alpha).\cos\alpha + h'(\alpha).\cos\alpha - h(\alpha).\sin\alpha$$
$$j'(\alpha) = d'(\alpha).\cos\alpha - d(\alpha).\sin\alpha - h'(\alpha).\sin\alpha - h(\alpha).\cos\alpha$$

Again matching the two wave equations yields:

$$k(\alpha).i'(\alpha) = \cos\alpha \quad and \quad k(\alpha).j'(\alpha) = -\sin\alpha$$

Thus:

$$\begin{aligned} k(\alpha).d'(\alpha).\sin\alpha + k(\alpha).d(\alpha).\cos\alpha \\ +k(\alpha).h'(\alpha).\cos\alpha - k(\alpha).h(\alpha).\sin\alpha = \cos\alpha \\ \Rightarrow k(\alpha)[d'(\alpha) - h(\alpha)]\sin\alpha + k(\alpha)[d(\alpha) + h'(\alpha\cos\alpha)] = \cos\alpha \end{aligned}$$

Similarly:

$$\begin{aligned} k(\alpha).d'(\alpha).\cos\alpha - k(\alpha).d(\alpha).\sin\alpha \\ -k(\alpha).h'(\alpha).\sin\alpha - k(\alpha).h(\alpha).\cos\alpha = \sin\alpha \\ \Rightarrow k(\alpha)[d'(\alpha) - h(\alpha)]\cos\alpha + k(\alpha)[d(\alpha) + h'(\alpha)]\sin\alpha = -\sin\alpha \end{aligned}$$

These two equations indicate, firstly that:

$$\begin{aligned} d'(\alpha) - h(\alpha) = 0 \\ \Rightarrow h(\alpha) = d'(\alpha) \end{aligned}$$

and secondly that:

$$d(\alpha) + h'(\alpha) = \frac{1}{k(\alpha)}$$
$$\Rightarrow k(\alpha) = \frac{1}{d(\alpha) + h'(\alpha)} = \frac{1}{d(\alpha) + d''(\alpha)}$$

This means that both factors, $h(\alpha)$ and $k(\alpha)$ are both written more conveniently in terms of the distance discrepancy function $d(\alpha)$. Substituting these terms, specifically $h(\alpha)$ means that the defining equations for a particular wavefront can be written exclusively in terms of the distance discrepancy function. Since the function $k(\alpha)$ is not necessary for the determination of the point $[i(\alpha); j(\alpha)]$ it is not discussed in detail.

The family of wavefronts, $\mathcal{W}(\alpha)$, associated with a particular distance discrepancy function is written in the following parametric format, using $[i(\alpha); j(\alpha)]$ as a point on a particular wavefront.

$$i(\alpha) = d(\alpha).\sin\alpha + d'(\alpha).\cos\alpha \tag{4.5}$$
$$j(\alpha) = d(\alpha).\cos\alpha - d'(\alpha).\sin\alpha \tag{4.6}$$

These equations indicate that it is necessary that $d(\alpha)$ be defined as a differentiable function, which is true for the distance discrepancy functions that were defined in Chapter 3.

It is interesting to notice that the wavefront, $\mathcal{W}(\alpha)$, is by definition the negative pedal curve of the distance discrepancy function, $d(\alpha)$, with respect to the central point of $d(\alpha)$. Since, a negative pedal curve with respect to another curve, Υ say, is defined as the envelope of the line drawn through a point on the curve Υ, perpendicular to the line intersecting a preselected stationary point (Lockwood 1961). Here $\mathcal{W}(\alpha)$ is determined by finding the envelope of the line $M(\alpha)$ drawn through a point $[a(\alpha), b(\alpha)]$ on the curve $d(\alpha)$, perpendicular to the central point of $d(\alpha)$.

4.2 Application of the Wavefront Equations

As mentioned previously, in the introduction to this Chapter, this Section is included in order to demonstrate the usefulness of the derived wavefront equations.

To begin with a working example of the derivation of the wavefront equation is presented in order to enhance understanding of the derivation technique. The distance discrepancy function used for this illustration is the 'special case' geometric distance discrepancy function, $\widehat{d_{G0}}(\alpha)$, which is introduced in Section 3.1. The resulting wavefront, for the distance discrepancy function, $\widehat{d_{G0}}(\alpha)$, is a 4-cusped hypocycloid which is consistent with the work of Longuet-Higgins (1990).

This derivation exercise is not essential to determining the family of wavefronts associated with a specific distance discrepancy function. In general the distance discrepancy function is substituted into the wavefront equations, equations 4.5 and 4.6, and the user need not be concerned with the actual derivation technique.

Following the working example of the derivation of the wavefront equations, the use of the wavefront equations is demonstrated by substituting first the geometric distance discrepancy function, $\widehat{d_G}(\alpha)$ and secondly the refracted distance discrepancy function $\widehat{d_R}(\alpha)$ into the wavefront equations. The wavefronts associated with each of the derived distance discrepancy functions are thus determined.

For each of these scenarios the distance components to the wavefront function are considered, that is the given distance discrepancy function $d(\alpha)$ and the derived distance component $h(\alpha)$. Each of these functions are plotted, using the polar plotting technique of the previous Chapter. Each of the distance components are then substituted into the wavefront equations and the corresponding wavefront graphs

are produced in order to ease the interpretation of the wavefront functions for each of the scenarios.

As mentioned previously, this Section begins with an overview of the technique used to derive the wavefront equations, with the aid of Figure 4.2, in terms of the 'special case' geometric distance discrepancy function, $\widehat{d_{G0}}(\alpha)$.

Initially a polar plot of the distance discrepancy function, in this case $\widehat{d_{G0}}$, is considered, actually the same plot that is produced in Figure 3.4. Onto this graph the straight line $L(\alpha)$ is constructed, and the point of intersection between the distance discrepancy function and the straight line is labeled $[a(\alpha); b(\alpha)]$ in Figure 4.2. The next step in the derivation is to construct the straight line $M(\alpha)$, perpendicular to the straight line $L(\alpha)$ and passing through the point $[a(\alpha); b(\alpha)]$.

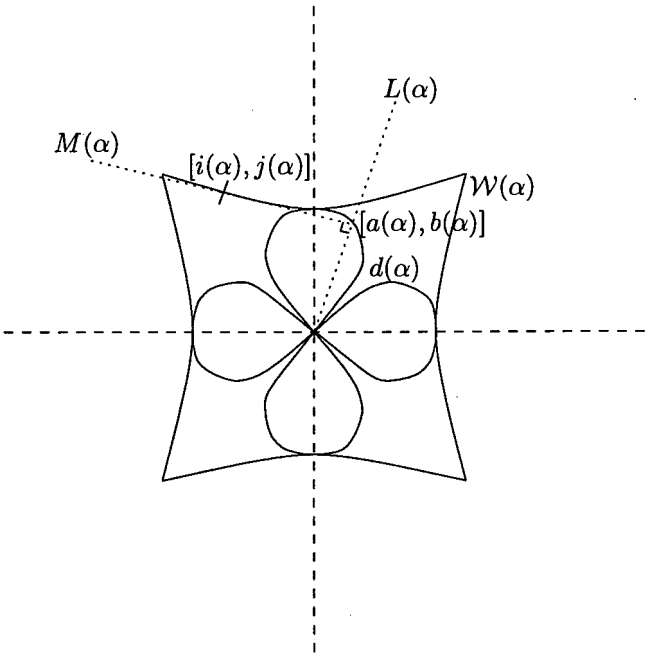

Figure 4.2: Diagram used in the derivation of a wavefront equation for the geometric distance discrepancy function.

The point of intersection between the straight line $M(\alpha)$ and the envelope of the wavefront is labeled as the point $[i(\alpha); j(\alpha)]$ in Figure 4.2. The generalized equations for the particular point $[i(\alpha); j(\alpha)]$ are given in equations 4.5 and 4.6 at the end of the previous section, Section 4.1, as:

$$i(\alpha) = d(\alpha).\sin\alpha + d'(\alpha).\cos\alpha$$
$$j(\alpha) = d(\alpha).\cos\alpha - d'(\alpha).\sin\alpha$$

In Section 3.1 the geometric distance discrepancy function is written in the convenient scaled form of:

$$\widehat{d_{G0}}(\alpha) = \cos 2\alpha$$
$$\Rightarrow \widehat{h_{G0}}(\alpha) = \widehat{d'_{G0}}(\alpha) = -2\sin 2\alpha$$

This means that for this particular distance discrepancy function the $h(\alpha)$ distance component has twice the magnitude of the distance discrepancy component.

The distance components, $\widehat{d_{G0}}(\alpha)$ and $\widehat{h_{G0}}(\alpha)$, are plotted in the figure below, Figure 4.3, using a polar coordinate system. The value table of the function $\widehat{h_{G0}}(\alpha)$ is included with the figure. The value table for $\widehat{d_{G0}}(\alpha)$ is included previously in Figure 3.3.

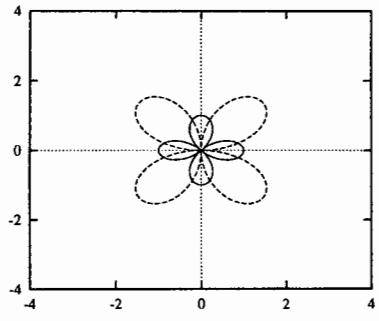

α	$\widehat{h_{G0}}(\alpha)$	α	$\widehat{h_{G0}}(\alpha)$
0^o	0	180^o	0
45^o	-2	225^o	-2
90^o	0	270^o	0
135^o	2	315^o	2

Figure 4.3: Polar plot of $\widehat{d_{G0}}(\alpha)$ (solid line) and $\widehat{h_{G0}}(\alpha)$ (dashed line), and the value table for $\widehat{h_{G0}}(\alpha)$.

Figure 4.3 demonstrates that both distance components form a 4-rose curve or a quadrifolium. The function $\widehat{d_{G0}}(\alpha)$ is discussed in detail with regard to Figure 3.3 and Table 3.3. The combined octant table for these two functions is not included as it provides no insight into the necessary understanding.

These two functions have a similar form but $\widehat{h_{G0}}(\alpha)$ has an inclination 45^o off that of the distance discrepancy function, $\widehat{d_{G0}}(\alpha)$, because $\widehat{h_{G0}}(\alpha)$ is of the '$\sin 2\alpha$ family' as opposed to, $\widehat{d_{G0}}(\alpha)$ of the '$\cos 2\alpha$ family'. The two functions also have the same bearing, in that they both have a clockwise orientation throughout their azimuthal range.

Also, it is clear that the azimuthal range $\alpha \in [0^o; 90^o]$ is responsible for the south-westerly loop; $\alpha \in [90^o; 180^o]$ is responsible for the south-easterly loop; $\alpha \in [180^o; 270^o]$ is responsible for the north-easterly loop; and $\alpha \in [270^o; 360^o]$ is responsible for the north-westerly loop of $\widehat{h_{G0}}(\alpha)$.

Returning to the derivation of the wavefront technique for the function $\widehat{d_{G0}}$, this function and its derivative with respect to α are substituted into the system of wave equations to yield:

$$\widehat{i_{G0}}(\alpha) = \cos 2\alpha . \sin \alpha - 2 \sin 2\alpha . \cos \alpha$$
$$\widehat{j_{G0}}(\alpha) = \cos 2\alpha . \cos \alpha + 2 \sin 2\alpha . \sin \alpha$$

Thus the derived wavefront equation after simplification is written:

$$\widehat{\mathcal{W}_{G0}}(\alpha) = [2 \sin^3 \alpha - 3 \sin \alpha; -2 \cos^3 \alpha + 3 \cos \alpha]$$

These parametric equations for the 'special case' geometric distance discrepancy function are plotted below in Figure 4.4. The value table associated with the function includes points in their Cartesian form, $[\widehat{i_{G0}}; \widehat{j_{G0}}]$.

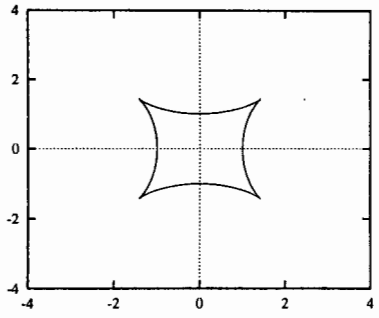

α	$(\widehat{i_{G0}};\widehat{j_{G0}})$	α	$(\widehat{i_{G0}};\widehat{j_{G0}})$
0^o	$0;1$	180^o	$0;-1$
45^o	$-\sqrt{2};\sqrt{2}$	225^o	$\sqrt{2};-\sqrt{2}$
90^o	$-1;0$	270^o	$1;0$
135^o	$-\sqrt{2};-\sqrt{2}$	315^o	$\sqrt{2};\sqrt{2}$

Figure 4.4: Cartesian graph and value table of $\widehat{\mathcal{W}_{G0}}(\alpha)$.

The wavefront plotted in Figure 4.4 is observed to be a four-cusped hypocycloid, the four cusps are orientated towards the north-west; south-west; south-east and the north-east. Lockwood (1961) showed that the negative pedal curve of a quadrifolium or 'four-rose curve' is a hypocycloid, as is the case here, where $\widehat{\mathcal{W}_{G0}}(\alpha)$ is a four-cusped hypocycloid and is the negative pedal curve of the four-rose curve $\widehat{d_{G0}}(\alpha)$.

In general, a four-cusped hypocycloid is defined in rectangular coordinates as:

$$x^{\frac{2}{3}} + y^{\frac{2}{3}} = a^{\frac{2}{3}}$$

or in parametric form:

$$x = a\cos^3\theta$$
$$y = a\sin^3\theta$$

and has an arclength $6a$, where a is the 'outer radial' distance, and an enclosed area of $\frac{3}{8}\pi a^2$ (Spiegel 1968).

The initial position of the wavefront is at $\widehat{\mathcal{W}_{G0}}(0^o) = [0;1]$, and as α increases from 0^o to 45^o, so $\widehat{\mathcal{W}_{G0}}(\alpha)$ moves into the north-westerly quadrant from $[0;1]$ to $[-\sqrt{2};-\sqrt{2}]$. Continuing in this manner yields the relevant octant table. The octant table for the wavefront associated with the 'special case' geometric distance discrepancy function is presented here in Table 4.1 to aid the discussion, which follows.

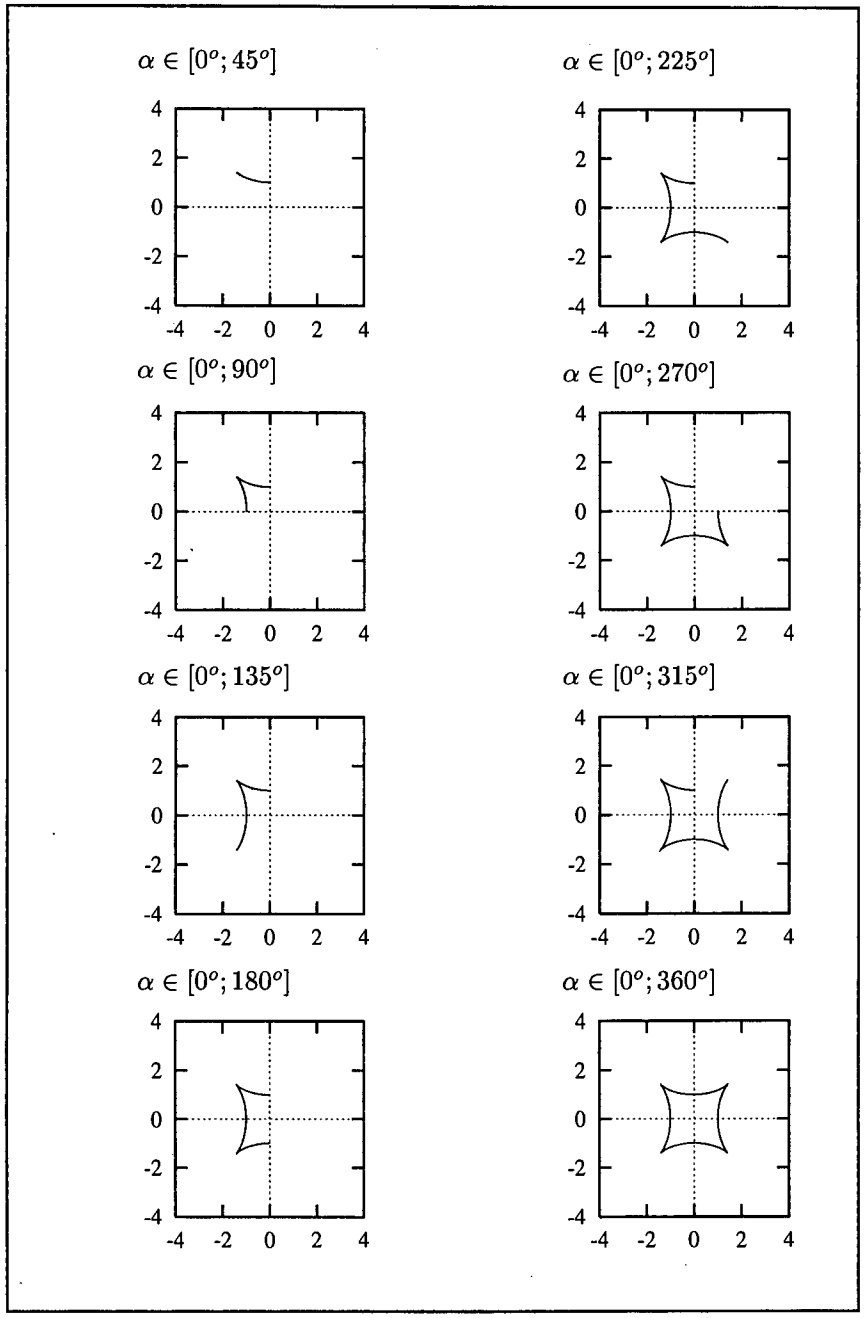

Table 4.1: Octant table for $\widehat{\mathcal{W}_{G0}}(\alpha)$.

The octant table clearly indicates that throughout the azimuthal range $\widehat{\mathcal{W}_{G0}}(\alpha)$ had an anticlockwise bearing. Notice that while $\widehat{\mathcal{W}_{G0}}(\alpha)$ has an anticlockwise rotation throughout the azimuthal range, both of the contributing distance components (in Figure 4.3) have clockwise rotations.

Notice also that as with the discussion regarding $\widehat{d_{G0}}(\alpha)$, which was negative in the azimuthal range $\alpha \in [45^o; 135^o]$ and $\alpha \in [225^o; 315^o]$, the 'west' and 'east' sectors of the hypocycloid, represent wavefronts that are yet to reach the antipodal point. Similarly, the 'north' and 'south' faces of the hypocycloid represent a region where $\widehat{d_{G0}}(\alpha)$ is positive, which means that those sectors of the wavefront are beyond the antipodal point.

Polar rays crossing the wavefront from the north and south, cross a particular wavefront sector orthogonally (by definition), and on the far side of the sector they converge. However, the tropical rays diverge as they cross the appropriate wavefront sectors.

The distance discrepancy function $\widehat{d_{G0}}(\alpha)$ used to demonstrate the technique of the derived wavefront equations is a rather special case, however in Section 3.1 of the previous Chapter, the geometric difference discrepancy function was written more generally in the form:

$$\widehat{d_G}(s,\lambda,\alpha) = \widehat{A_G}(s,\lambda) + \cos 2\alpha$$
$$\Rightarrow \widehat{h_G}(\alpha) = \widehat{d'_G}(s,\lambda,\alpha) = -2\sin 2\alpha$$

Again, as in the previous chapter, where a number of specific functions of the $\widehat{d_G}(\alpha)$ family are considered, the distance components of the geometric distance discrepancy function are considered here with respect to the corresponding integer values of $\widehat{A_G}(\alpha)$. The relevant functions $\widehat{d_{G-3}}(\alpha); \widehat{d_{G-2}}(\alpha); \ldots; \widehat{d_{G+2}}(\alpha); \widehat{d_{G+3}}(\alpha)$ and $\widehat{h_G}(\alpha)$ are plotted below in Figure 4.5. The value table associated with $\widehat{d_G}(\alpha)$ is included with Figure 3.4 and the value table associated with $\widehat{h_G}(\alpha)$ is the same as the value table for $\widehat{h_{G0}}(\alpha)$ and is included with Figure 4.3.

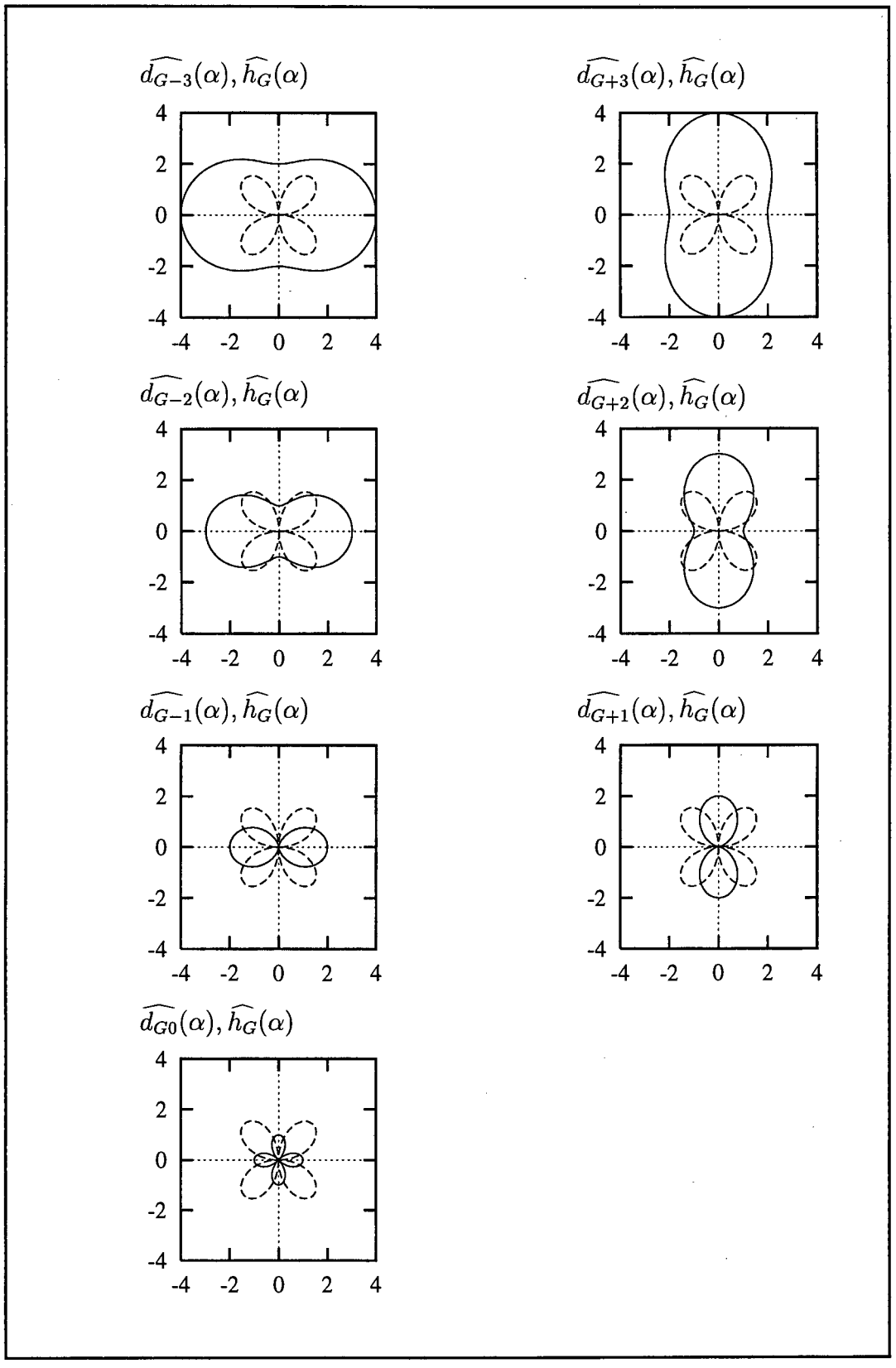

Figure 4.5: Polar plot of $\widehat{d_G}(\alpha)$ (solid line) and $\widehat{h_G}(\alpha)$ (dashed line).

Figure 4.5 is provided for completeness, it contains the same distance discrepancy functions that were described in detail with regard to Figure 3.4 and since $\widehat{h_G}(\alpha)$ is the same function as $\widehat{h_{G0}}(\alpha)$, the discussion regarding $\widehat{h_{G0}}(\alpha)$ with regard to Figure 4.3 corresponds to the figure above as well.

It is important to notice that $\widehat{h_G}(\alpha)$ is independent of $\widehat{A_G}(\alpha)$. This means that while the distance discrepancy function $\widehat{d_G}(\alpha)$ varies for incremental values of $\widehat{A_G}(\alpha)$, $\widehat{h_G}(\alpha)$ remains invariant. Consequently the sideways deflection of a ray is the same for all increments of $\widehat{A_G}(\alpha)$, as the ray approaches or departs from the antipodal region.

Substituting the distance components into the wavefront equations means that the family of wavefronts associated with the geometric discrepancy function are written in the generalized form:

$$\widehat{\mathcal{W}_G}(\alpha) = [2\sin^3\alpha + (\widehat{A_G} - 3)\sin\alpha; -2\cos^3\alpha + (\widehat{A_G} + 3)\cos\alpha]$$

The family of wavefronts associated with the geometric distance discrepancy function, $\widehat{d_G}(\alpha)$, are plotted below in Figure 4.6. These functions are referenced according to the relevant integral values of $\widehat{A_G}(\alpha)$, thus the wavefronts plotted are $\widehat{\mathcal{W}_{G-3}}(\alpha); \widehat{\mathcal{W}_{G-2}}(\alpha); \ldots; \widehat{\mathcal{W}_{G+2}}(\alpha); \widehat{\mathcal{W}_{G+3}}(\alpha)$. The figure is followed immediately by the relevant value table.

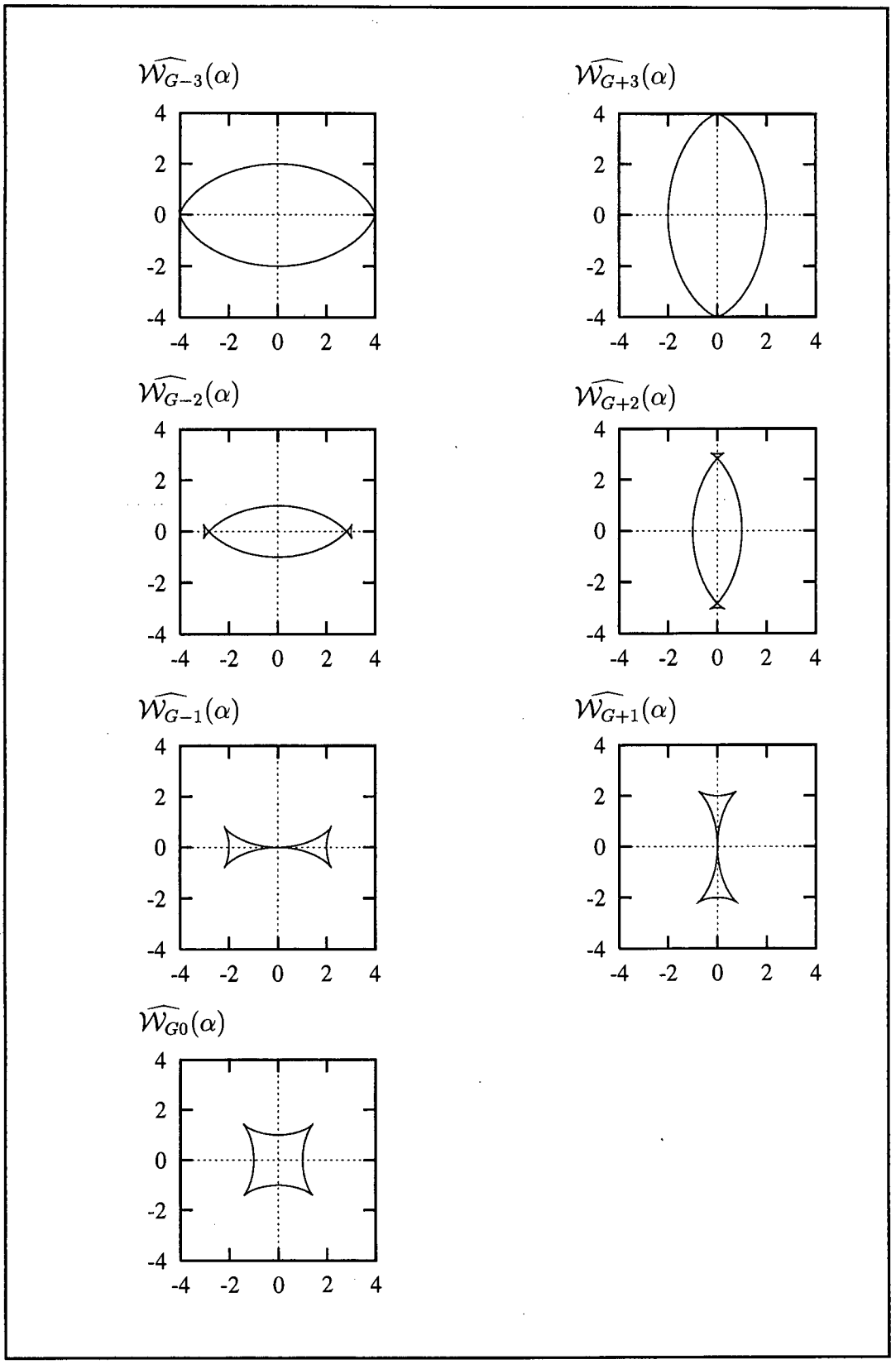

Figure 4.6: Cartesian graph of $\widehat{\mathcal{W}_G}(\alpha)$.

α	$\widehat{W_G}(\alpha)$	
	$\widehat{i_G}(\alpha)$	$\widehat{j_G}(\alpha)$
0	0	$1+\widehat{A_G}$
45^o	$-\sqrt{2}+\frac{\widehat{A_G}}{\sqrt{2}}$	$\sqrt{2}+\frac{\widehat{A_G}}{\sqrt{2}}$
90^o	$-1+\widehat{A_G}$	0
135^o	$-\sqrt{2}+\frac{\widehat{A_G}}{\sqrt{2}}$	$-\sqrt{2}-\frac{\widehat{A_G}}{\sqrt{2}}$
180^o	0	$-1-\widehat{A_G}$
225^o	$\sqrt{2}-\frac{\widehat{A_G}}{\sqrt{2}}$	$-\sqrt{2}-\frac{\widehat{A_G}}{\sqrt{2}}$
270^o	$1-\widehat{A_G}$	0
315^o	$\sqrt{2}-\frac{\widehat{A_G}}{\sqrt{2}}$	$\sqrt{2}+\frac{\widehat{A_G}}{\sqrt{2}}$
360^o	0	$1+\widehat{A_G}$

Again a correspondence exists between the approaching/departing wavefronts and the negative/positive values of $\widehat{d_G}(\alpha)$, which are discussed with regard to Figure 3.4. As in the geometric distance discrepancy functions, the wavefront value 'marches' forward with respect to the $\widehat{A_G}(\alpha)$ value. Thus for the wavefronts approaching the proxy antipode ($\widehat{A_G}(\alpha) < 0$) the wave fronts have a two-fold symmetry about the $x-axis$ and appear to be "compressed" towards the $x-axis$. This is because rays approaching the region from the poles approach more quickly than those approaching over the greater distance along the equator. Similarly for those wavefronts beyond the proxy antipode ($\widehat{A_G}(\alpha) > 0$), there is a two-fold symmetry about the $y-axis$ and these wavefronts appear to be extended along the $y-axis$. This is because the rays approaching the poles have already passed over the antipodal region, more quickly than the equatorial paths, which appear to lag behind. The graph associated with $\widehat{W_{G0}}(\alpha)$ is discussed in detail with regard to Figure 4.4 and is the only member of the '$+\cos 2\alpha$ family' that has a four-fold symmetry.

Again, as the geometric distance discrepancy function passes through a series of phases as the ray approaches or departs from the proxy origin, so the wavefront function passes through a series of phases. For the $\widehat{W_{G\pm3}}(\alpha)$ functions the wavefronts appear to have a 'disc' shape with all sides of the wavefront either converging towards or diverging from the antipodal point for $\widehat{A_G}(\alpha) < 0$ and $\widehat{A_G}(\alpha) > 0$ respectively.

Between the integer values $|\widehat{A_G}(\alpha)| = 3$ and $|\widehat{A_G}(\alpha)| = 2$ the wavefront transforms from a disc shape to a disc shape with two anomalies at each of the narrow ends. Again all sides of the wavefronts are either converging on or diverging from the antipodal point depending on the sign of the $\widehat{A_G}(\alpha)$ term.

Between the values $|\widehat{A_G}(\alpha)| = 2$ and $|\widehat{A_G}(\alpha)| = 1$ the wavefront function undergoes another transformation, this time a 'bow' shaped form results, since the anomalous endpoints associated with $|\widehat{A_G}(\alpha)| = 2$ seem to dominate the disc shape form associated with $|\widehat{A_G}(\alpha)| = 3$.

For the $\widehat{W_{G-1}}(\alpha)$ wavefront the sides approaching from the poles intersect at the antipodal point and the equatorial sides are still converging on the proxy origin. For the $\widehat{W_{G+1}}(\alpha)$ wavefront the sides from the poles have crossed the antipodal point and are now diverging away from the region, while the equatorial fronts have intersected at the antipodal point.

Between the values $|\widehat{A_G}(\alpha)| = 1$ and $|\widehat{A_G}(\alpha)| = 0$ the wavefront function is transformed into the

hypocycloid form discussed in detail with regard to the $\widehat{\mathcal{W}_{G0}}(\alpha)$ function in Figure 4.4.

For all the wavefronts the initial position $\widehat{\mathcal{W}_G}(0^o)$ lies on the $y-axis$ of the Cartesian graph, at $[0; 1+\widehat{A_G}]$. This means that for $\widehat{A_G} > -1$ the initial position lies above the $x-axis$; for $\widehat{A_G} < -1$ the initial position lies below the $x-axis$; and for $\widehat{A_G} = -1$ the initial position is on the origin.

To provide more insight into the geometric wavefront family the relevant octant table is provided below in Table 4.2.

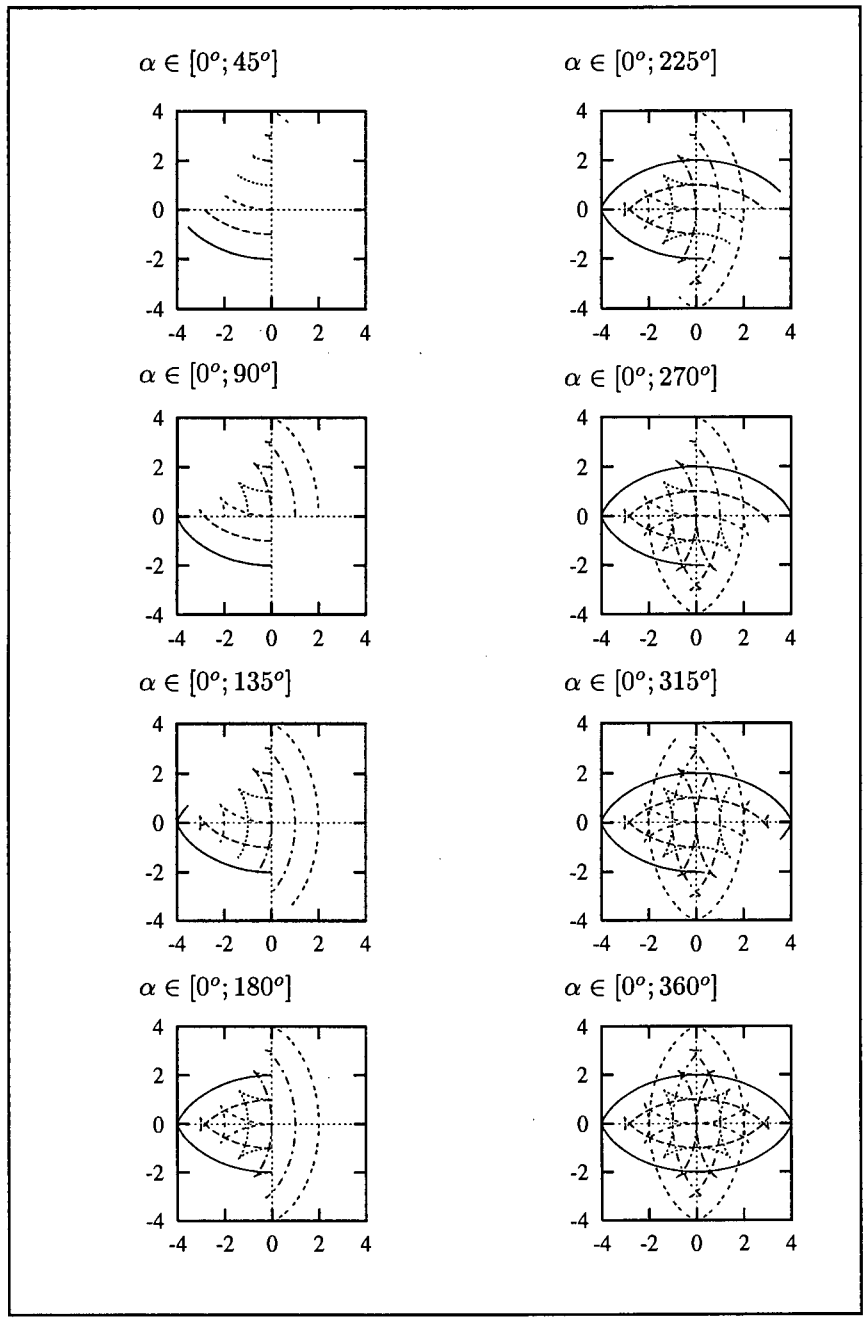

Table 4.2: Octant table for $\widehat{\mathcal{W}_G}(\alpha)$, for the integer values of $\widehat{A_G}(\alpha) = -3; -2; \ldots; 2; 3$.

The octant table together with the value table in Figure 4.6 indicate the bearing of each of the $\widehat{\mathcal{W}_G}(\alpha)$

functions. Notice that the $\widehat{\mathcal{W}_{G\pm3}}$ functions have a clockwise rotation. The two wavefronts, $\widehat{\mathcal{W}_{G\pm2}}$, have a clockwise rotation within their disc shaped form, and an anticlockwise rotation within their anomalous endpoints. The wavefronts $\widehat{\mathcal{W}_{G\pm1}}$ and $\widehat{\mathcal{W}_{G0}}$ have an anticlockwise rotation. Thus the $\widehat{\mathcal{W}_{G\pm2}}$ demonstrate the transition between the totally anticlockwise wavefronts for the graphs with $\widehat{A_G} < |1|$ and the entirely clockwise rotation for $\widehat{A_G} = |3|$.

Also notice, that as was the case in Table 3.2, the octant table above demonstrates that for successive values of $\widehat{A_G}$ the wavefronts progress through the antipodal region along an azimuthal bearing, for example along the $\alpha = 45^o$ line.

The graphs of the $\widehat{\mathcal{W}_G}(\alpha)$ family, in Figure 4.6, are the corresponding negative pedal curves of the $\widehat{d_G}(\alpha)$ family, with respect to the center of the distance discrepancy functions.

The previous paragraph ends the discussion regarding the family of wavefronts under the geometric assumption at this stage the envelope of wavefronts associated with the refractive distance discrepancy function is considered. Here:

$$\widehat{d_R}(\alpha) = 1 - \cos 2\alpha$$
$$\Rightarrow \widehat{h_R}(\alpha) = \widehat{d'_R}(\alpha) = 2\sin 2\alpha$$

The refractive distance discrepancy function is discussed in detail in the previous chapter, Chapter 3, particularly with regard to Figure 3.6. The function $\widehat{d_R}(\alpha)$ is plotted below in Figure 4.7, together with $\widehat{h_R}(\alpha)$, to demonstrate the distance components of the wavefronts associated with the refractive distance discrepancy function. The value table for $\widehat{h_R}(\alpha)$ is included with the figure, the value table associated with $\widehat{d_R}(\alpha)$ is included with Figure 3.6.

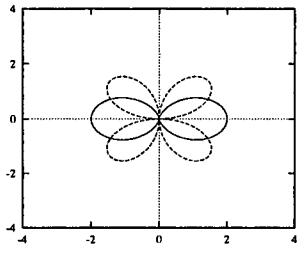

α	$\widehat{h_R}(\alpha)$	α	$\widehat{h_R}(\alpha)$
0^o	0	180^o	0
45^o	2	225^o	2
90^o	0	270^o	0
135^o	-2	315^o	-2

Figure 4.7: Polar plot of $\widehat{d_R}(\alpha)$ (solid line) and $\widehat{h_R}(\alpha)$ (dashed line) and the value table for $d_R(\alpha)$.

As mentioned above the refractive distance discrepancy function is discussed in detail in Section 3.2. The other distance component of the wavefront, $\widehat{h_R}(\alpha)$, appears to be very similar to $\widehat{h_G}(\alpha)$, in fact they only differ in sign. Clearly from Figure 4.7, while $\widehat{d_R}(\alpha)$ is a lemniscate, $\widehat{h_R}(\alpha)$ is a quadrifolium offset from the $x - y$ *axis* by 45^o.

Examination of the value table indicates that $\widehat{d_R}(\alpha)$ and $\widehat{h_R}(\alpha)$ have a clockwise orientation throughout the azimuthal range.

Because both $\widehat{d_R}(\alpha)$ and $\widehat{h_R}(\alpha)$ are invariant with respect to the approach or the departure from the

antipode only one wavefront is derived for the refractive distance discrepancy function. Substituting $\widehat{d_R}(\alpha)$ and $\widehat{h_R}(\alpha)$ into the wavefront equations yields:

$$\widehat{i_R}(\alpha) = (1 - \cos 2\alpha).\sin\alpha + 2\sin 2\alpha.\cos\alpha$$
$$\widehat{j_R}(\alpha) = (1 - \cos 2\alpha).\cos\alpha - 2\sin 2\alpha.\sin\alpha$$

These equations are written in a simplified form:

$$\widehat{i_R}(\alpha) = -2\sin^3\alpha + 4\sin\alpha$$
$$\widehat{j_R}(\alpha) = +2\cos^3\alpha - 2\cos\alpha$$

The wavefront graph for the refractive distance discrepancy function is been plotted below in Figure 4.8 using a Cartesian coordinate system. The corresponding value table is included with the figure.

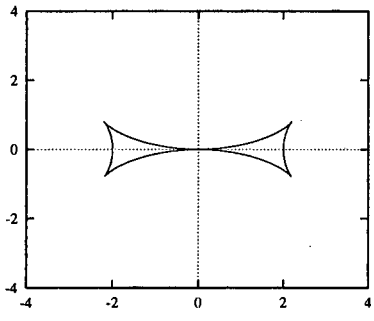

α	$(\widehat{i_R};\widehat{j_R})$	α	$(\widehat{i_R};\widehat{j_R})$
0^o	$0;0$	180^o	$0;0$
45^o	$\frac{3}{\sqrt{2}};\frac{-1}{\sqrt{2}}$	225^o	$\frac{-3}{\sqrt{2}};\frac{1}{\sqrt{2}}$
90^o	$2;0$	270^o	$-2;0$
135^o	$\frac{3}{\sqrt{2}};\frac{1}{\sqrt{2}}$	315^o	$\frac{-3}{\sqrt{2}};\frac{-1}{\sqrt{2}}$

Figure 4.8: Cartesian graph and value table of $\widehat{\mathcal{W}_R}(\alpha)$.

Figure 4.8 demonstrates that the negative pedal curve of a lemniscate function, with respect to the center of the lemniscate, is a "compressed hypocycloid", with the same orientation as the lemniscate, in this case both have a west-east orientation. Now $\widehat{d_R}(\alpha)$ is positive throughout the azimuthal range, except at $\alpha = 0^o$ or $\alpha = 180^o$, where $\widehat{d_R}(\alpha) = 0$. This indicates that the wavefront has propagated beyond the antipodal point, except for the two polar ray path components of the wavefront, which are positioned at the antipodal point.

$\widehat{\mathcal{W}_R}(\alpha)$ plotted above in Figure 4.8, has an initial position $\widehat{\mathcal{W}_R}(0^o) = [0;0]$. As α ranges from 0^o to 45^o so $\widehat{\mathcal{W}_R}(\alpha)$ ranges from $[0;0]$ to $[\frac{3}{\sqrt{2}};\frac{-1}{\sqrt{2}}]$. Continuing in this fashion provides the octant table, which is presented below in Table 4.3.

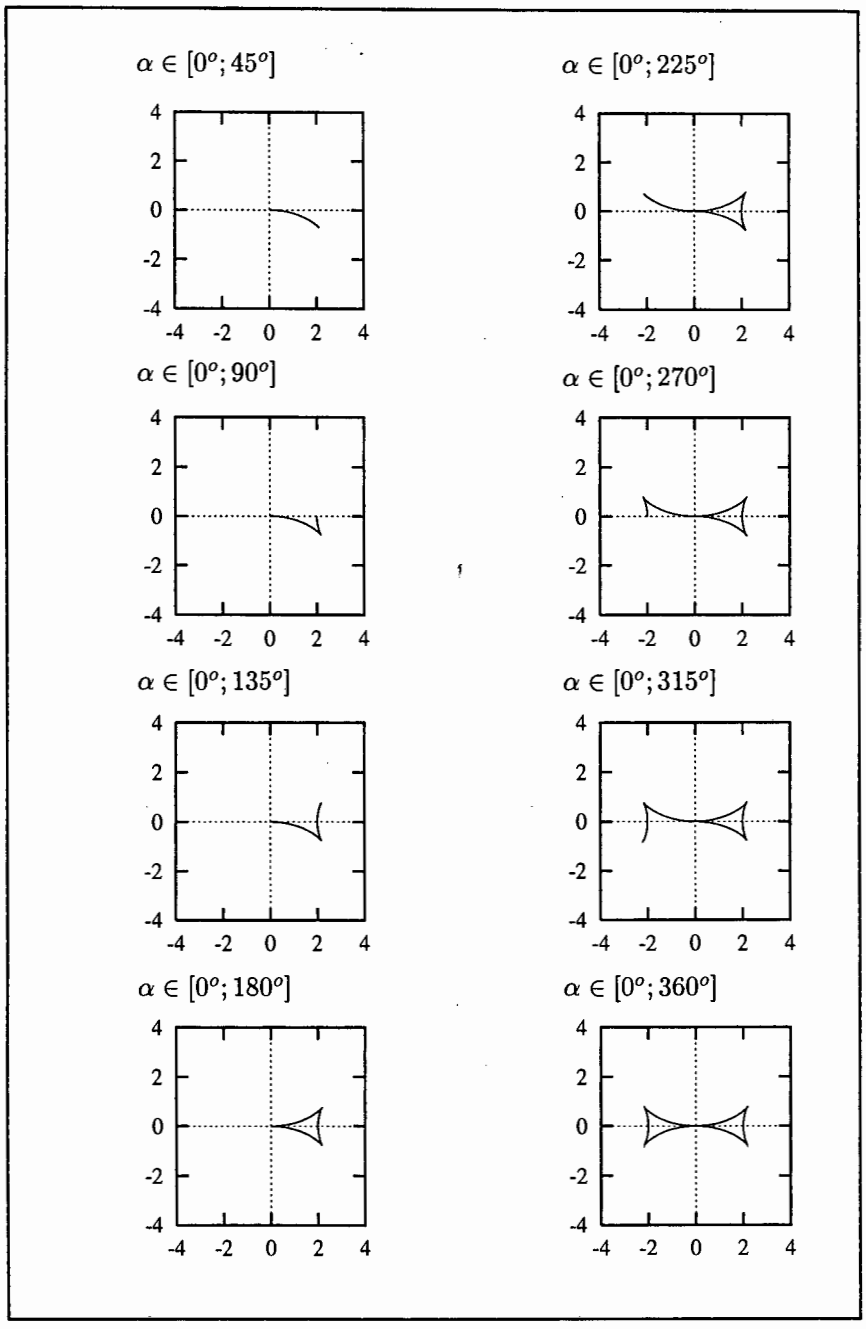

Table 4.3: Octant table for $\widehat{\mathcal{W}_R}(\alpha)$.

The octant table clearly indicates that $\widehat{\mathcal{W}_R}(\alpha)$ has an anticlockwise rotation throughout the azimuthal range. This wavefront has a similar form to $\widehat{\mathcal{W}_{G^{-1}}}(\alpha)$ in Figure 4.6. They have the same initial positions, but opposite directions of rotation, that is $\widehat{\mathcal{W}_{G^{-1}}}(\alpha)$ has an anticlockwise rotation and $\widehat{\mathcal{W}_R}(\alpha)$ has a clockwise rotation.

Both $\widehat{\mathcal{W}_{G^{-1}}}(\alpha)$ and $\widehat{\mathcal{W}_R}(\alpha)$ have the same initial positions, $\widehat{\mathcal{W}_{G^{-1}}}(0^o) = [0^o; 0^o] = \widehat{\mathcal{W}_R}(0^o)$, and the same anticlockwise orientation throughout their azimuthal range, but $\widehat{\mathcal{W}_{G^{-1}}}(\alpha)$ begins by moving into the north-west quadrant and $\widehat{\mathcal{W}_R}(\alpha)$ into the south-east quadrant, thus the graphs of these functions are offset by a factor of 180^o.

Chapter 5

The Caustic

In the previous chapter the family of wavefronts are determined, according to the particular arrival pattern of rays approaching the antipodal region under certain physical assumptions. In this chapter the envelope of ray paths close to the antipodal region, known as the caustic curve, is derived from the relevant family of wavefronts. From the definition of a wavefront, the ray paths intersect the wavefronts orthogonally and thus any member of the wavefront family can be used to determine the caustic curve associated with that family (Longuet-Higgins 1990). The caustic curve provides insight into the region of the proposed enhanced signal close to the antipode.

In the first section, Section 5.1, a procedure is derived for determining the caustic curve connected with the family of wavefronts associated with the advancing rays at a particular time. The rays are advancing according to a defined distance discrepancy function, $d(\alpha)$. The procedure results in a set of parametric equations that represent the caustic curve, $\mathcal{C}(\alpha)$. A specific distance discrepancy function can be substituted into the parametric equations in order to determine the relevant caustic curve.

In order to demonstrate the derived caustic curve equations the caustic curve associated with the geometric and refractive distance discrepancy functions of Chapter 3 are established in Section 5.2. Initially the geometric distance discrepancy function is substituted into the caustic equations, providing results consistent with Longuet-Higgins (1990). The procedure is repeated for the refractive distance discrepancy function, with agreeable results.

5.1 Derivation of the Caustic Curve Equations

In this section a set of parametric equations are derived to determine the caustic associated with a family of wavefronts, which in turn are associated with a specific distance discrepancy function. In order to provide equations relevant to any distance discrepancy function a completely arbitrary distance discrepancy function, $d(\alpha)$, is used throughout this section.

The derivation is presented here for two reasons, firstly to validate the resulting parametric equations and secondly for completeness.

Again, as in the previous chapter, the derivation has a strong geometric emphasis and relies a great deal on Longuet-Higgins (1990). The notation that is used in the derivation which follows is introduced with the aid of Figure 5.1. Figure 5.1 develops from Figure 4.1, which was used to aid the derivation

of the family of wavefronts for a particular distance discrepancy function.

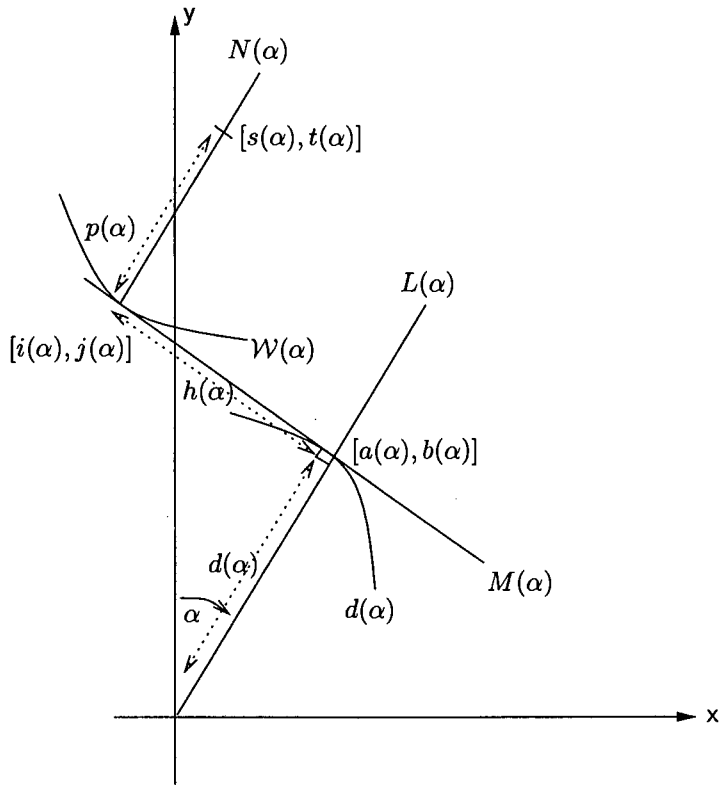

Figure 5.1: Introduction to the notation used to derive the equation of the caustic curve.

Figure 5.1 includes a portion of the $d(\alpha)$ function, plotted on a polar coordinate system. Using the technique of the previous chapter a portion of the wavefront associated with the $d(\alpha)$ function is plotted through the point $[i(\alpha); j(\alpha)]$ on the straight line $M(\alpha)$ and tangent to the line $M(\alpha)$.

This derivation begins by constructing the straight line $N(\alpha)$ through the point $[i(\alpha); j(\alpha)]$ on $M(\alpha)$ and perpendicular to the line $M(\alpha)$. Now, $N(\alpha)$ is defined to be perpendicular to $M(\alpha)$, and $M(\alpha)$ is defined in the previous chapter to be perpendicular to $L(\alpha)$. Thus $N(\alpha)$ is parallel to $L(\alpha)$ and these two straight lines have the same gradient.

So the equation of $N(\alpha)$ is written in Cartesian coordinates as:

$$N(\alpha) := \sin\alpha[y - j(\alpha)] = \cos\alpha[x - i(\alpha)]$$

By definition of the caustic curve the envelope of the lines $N(\alpha)$, for all α, provide the equation of the caustic curve for the given distance discrepancy function. Again, as in the wavefront derivation, the question arises as to how far along the line $N(\alpha)$ must one proceed before the caustic envelope is intersected. The point of intersection between $N(\alpha)$ and the caustic curve is labeled $[s(\alpha); t(\alpha)]$ in Figure 5.1 and can be written in the form:

$$\mathcal{C}(\alpha) := [s(\alpha); t(\alpha)]$$

The distance between $[i(\alpha); j(\alpha)]$ and $[s(\alpha); t(\alpha)]$ is defined here as $p(\alpha)$ and at this stage is an unknown factor that is added to both sides of the equation $N(\alpha)$. Thus:

$$\sin\alpha[y - j(\alpha) + p(\alpha).\cos\alpha] = \cos\alpha[x - i(\alpha) + p(\alpha).\sin\alpha] \tag{5.1}$$

At this point, a function of the envelope of straight lines, $N(\alpha)$, is generated from known parameters. Already this function, known as the caustic function, has a point $[s(\alpha); t(\alpha)]$ defined on it and the caustic curve tangent has a gradient $\frac{t'(\alpha)}{s'(\alpha)}$, where $t'(\alpha) = \frac{\partial t(\alpha)}{\partial \alpha}$ and $s'(\alpha) = \frac{\partial s(\alpha)}{\partial \alpha}$. Thus a tangent through the caustic curve passing through the point $[s(\alpha); t(\alpha)]$ has an equation of the form:

$$s'(\alpha)[y - t(\alpha)] = t'(\alpha)[y - s(\alpha)]$$

Notice that this equation does not contain a scaling factor and in order to generalize it for all tangents, multiply both sides of the equation by a factor $q(\alpha)$, say. Consequently the equation for a tangent to the caustic curve is written in the form:

$$s'(\alpha).q(\alpha)[y - t(\alpha)] = t'(\alpha).q(\alpha)[y - s(\alpha)] \tag{5.2}$$

Now the envelope of the caustic curve is defined by two distinct equations, that of equation 5.1 and equation 5.2. By systematically equating the x and y components of these equations the generalized point $[s(\alpha); t(\alpha)]$ is easily determined.

In fact matching equation 5.1 and equation 5.2 yields:

$$s(\alpha) = i(\alpha) - p(\alpha).\sin\alpha$$
$$t(\alpha) = j(\alpha) - p(\alpha).\cos\alpha$$

But $i(\alpha)$ and $j(\alpha)$ are defined in the previous chapter, in equations 4.5 and 4.6 respectively. Substituting these known values into the $s(\alpha)$ and $t(\alpha)$ equations above gives:

$$s(\alpha) = d(\alpha).\sin\alpha + d'(\alpha).\cos\alpha - p(\alpha).\sin\alpha$$
$$t(\alpha) = d(\alpha).\cos\alpha - d'(\alpha).\sin\alpha - p(\alpha).\cos\alpha$$

These equations indicate that a point on the caustic curve is constructed from three different distance components: two in the direction of the ray propagation, $d(\alpha)$ and $p(\alpha)$, and one $h(\alpha)$, which is shown to be $d'(\alpha)$ perpendicular to the ray direction, in the previous chapter.

Now the equations for $s(\alpha)$ and $t(\alpha)$ are differentiated with respect to α, producing the following equations:

$$\begin{aligned} s'(\alpha) = d'(\alpha).\sin\alpha + d(\alpha).\cos\alpha + d''(\alpha).\cos\alpha - d'(\alpha).\sin\alpha \\ -p'(\alpha).\sin(\alpha) - p(\alpha).\cos(\alpha) \\ \Rightarrow s'(\alpha) = [d(\alpha) + d''(\alpha) - p(\alpha)].\cos\alpha - [p'(\alpha)].\sin\alpha \end{aligned}$$

$$\begin{aligned} t'(\alpha) = d'(\alpha).\cos\alpha - d(\alpha).\sin\alpha - d''(\alpha).\sin\alpha - d'(\alpha).\cos\alpha \\ -p'(\alpha).\cos(\alpha) - p(\alpha).\sin(\alpha) \\ \Rightarrow t'(\alpha) = -[d(\alpha) + d''(\alpha) - p(\alpha)].\sin\alpha - [p'(\alpha)].\cos\alpha \end{aligned}$$

Again, matching the two caustic equations gives:

$$s'(\alpha).q(\alpha) = \sin\alpha \; and \; t'(\alpha).q(\alpha) = \cos\alpha$$

These two equations in turn imply that:

$$q(\alpha)[d(\alpha) + d''(\alpha) - p(\alpha)].\cos\alpha - q(\alpha)[p'(\alpha)].\sin\alpha = \sin\alpha$$
$$-q(\alpha)[d(\alpha) + d''(\alpha) - p(\alpha)].\sin\alpha - q(\alpha)[p'(\alpha)].\cos\alpha = \cos\alpha$$

From these equations it is deduced that:

$$d(\alpha) + d''(\alpha) - p(\alpha) = 0$$
$$\Rightarrow p(\alpha) = d(\alpha) + d''(\alpha)$$

and:

$$q(\alpha) = \frac{-1}{p'(\alpha)}$$
$$\Rightarrow q(\alpha) = \frac{-1}{d'(\alpha) + d'''(\alpha)}$$

This means that, as in the wavefront derivation, both factors: $p(\alpha)$ and $q(\alpha)$ can be written conveniently in terms of the distance discrepancy function, $d(\alpha)$. Again, as for $k(\alpha)$, $q(\alpha)$ is not used to define the caustic curve coordinates and thus is not considered further.

$p(\alpha)$ denotes the distance from the wavefront, $\mathcal{W}(\alpha)$, to the relevant point on the caustic curve, $\mathcal{C}(\alpha)$. In common with convention adopted for the distance discrepancy function, the value of $p(\alpha)$ will be negative when the wavefront is approaching the antipodal point and will be negative when the wavefront has passed the antipodal point. In other words a wavefront with $p(\alpha)$ negative will be converging and one with $p(\alpha)$ positive will be diverging.

The caustic curve associated with a particular distance discrepancy function is thus written in the following parametric format, using the point $[s(\alpha); t(\alpha)]$ as a point on the caustic curve:

$$s(\alpha) = d(\alpha)\sin\alpha + d'(\alpha)\cos\alpha - d(\alpha)\sin\alpha - d''(\alpha)\sin\alpha$$
$$t(\alpha) = d(\alpha)\cos\alpha - d'(\alpha)\sin\alpha - d(\alpha)\cos\alpha - d''(\alpha)\cos\alpha$$

Simplification yields the parametric equation for the caustic curve:

$$s(\alpha) = d'(\alpha)\cos\alpha - d''(\alpha)\sin\alpha \tag{5.3}$$
$$t(\alpha) = -d'(\alpha)\sin\alpha - d''(\alpha)\cos\alpha \tag{5.4}$$

These equations indicate that not only does the distance discrepancy function have to be defined as a differentiable function, as was necessary for determining the family of wavefronts, but in order to determine the caustic curve with respect to a specific distance discrepancy function, that function must be twice differentiable. Also, notice that these two equations, which define the caustic curve, are independent of the actual distance discrepancy function. Consequently, the caustic curve is constructed with the first and second derivatives of the distance discrepancy function only. The distance discrepancy functions determined in Chapter 3 are all twice differentiable and are thus appropriate.

It is interesting to notice that the caustic curve, $\mathcal{C}(\alpha)$ is by definition the evolute of the corresponding wavefront functions, $\mathcal{W}(\alpha)$. Where the evolute is defined as the envelope of the normals to the original curve (Lockwood 1961). In this case the caustic is generated from the envelope of ray paths, which are everywhere perpendicular to the wavefront. The original curve is defined as the involute of the new curve (Lockwood 1961). Thus the wavefront curve is the involute of the caustic curve. Parker (1994) defines an involute curve as the curve that lies on the tangent surface of a given space curve and is orthogonal to the tangents to the given curve.

5.2 Application of the Caustic Curve Equations

As in the previous chapter, where Section 4.2 is included so as to demonstrate the usefulness of the derived wavefront equations, this section is included to demonstrate the usefulness of the caustic curve equation.

A working example of the derivation of the caustic curve equation is provided here to improve understanding of the derivation technique. The distance discrepancy function used is the 'special case' geometric distance discrepancy function, $\widehat{d_{G0}}(\alpha)$, which was introduced in Section 3.1. The resulting caustic for that distance discrepancy function is a four-cusped hypocycloid, which corresponds exactly to the work of Longuet-Higgins (1990).

The derivation is not essential to determining the caustic curve for a particular distance discrepancy function. In general the distance discrepancy function is substituted into the equations for the caustic curve, that is equations 5.3 and 5.4, and the user need not be concerned with the derivation technique.

The usefulness of the caustic curve equations are demonstrated by substituting first the geometric distance discrepancy function, $\widehat{d_G}(\alpha)$, and secondly the refracted distance discrepancy function, $\widehat{d_R}(\alpha)$, into the caustic curve equations. The caustic curve for each of the distance discrepancy functions, that are introduced in Chapter 3, are thus determined.

For each of the scenarios, that is the geometric and refractive scenarios, the distance components to the caustic curve are considered. The distance components are: the given distance discrepancy function, $d(\alpha)$; and the derived functions $h(\alpha)$ and $p(\alpha)$. Each of these functions are plotted, using the polar plotting technique introduced in Chapter 3. The value table for the relevant $p(\alpha)$ function is included with each of the composite graphs. The value table associated with the $d(\alpha)$ and $h(\alpha)$ functions were included as part of the relevant graphs when they were introduced into the text in the previous two chapters.

The distance components are then substituted into the caustic curve equation. The corresponding curve is plotted using a Cartesian coordinate system.

As mentioned before this section begins with an overview of the derivation technique used to derive the caustic curve equations. The 'special case' geometric distance discrepancy function, $\widehat{d_{G0}}(\alpha)$, is used, with the aid of Figure 5.2, to demonstrate the derivation technique and how the equations for the caustic curve can be used for other distance discrepancy functions.

Figure 5.2 (below) builds upon Figure 4.2 from the previous chapter. The function $\widehat{d_{G0}}(\alpha)$ is plotted, as well as the corresponding wavefront graph, $\widehat{\mathcal{W}_{G0}}(\alpha)$. Also the straight lines $L(\alpha)$ and $M(\alpha)$ are included.

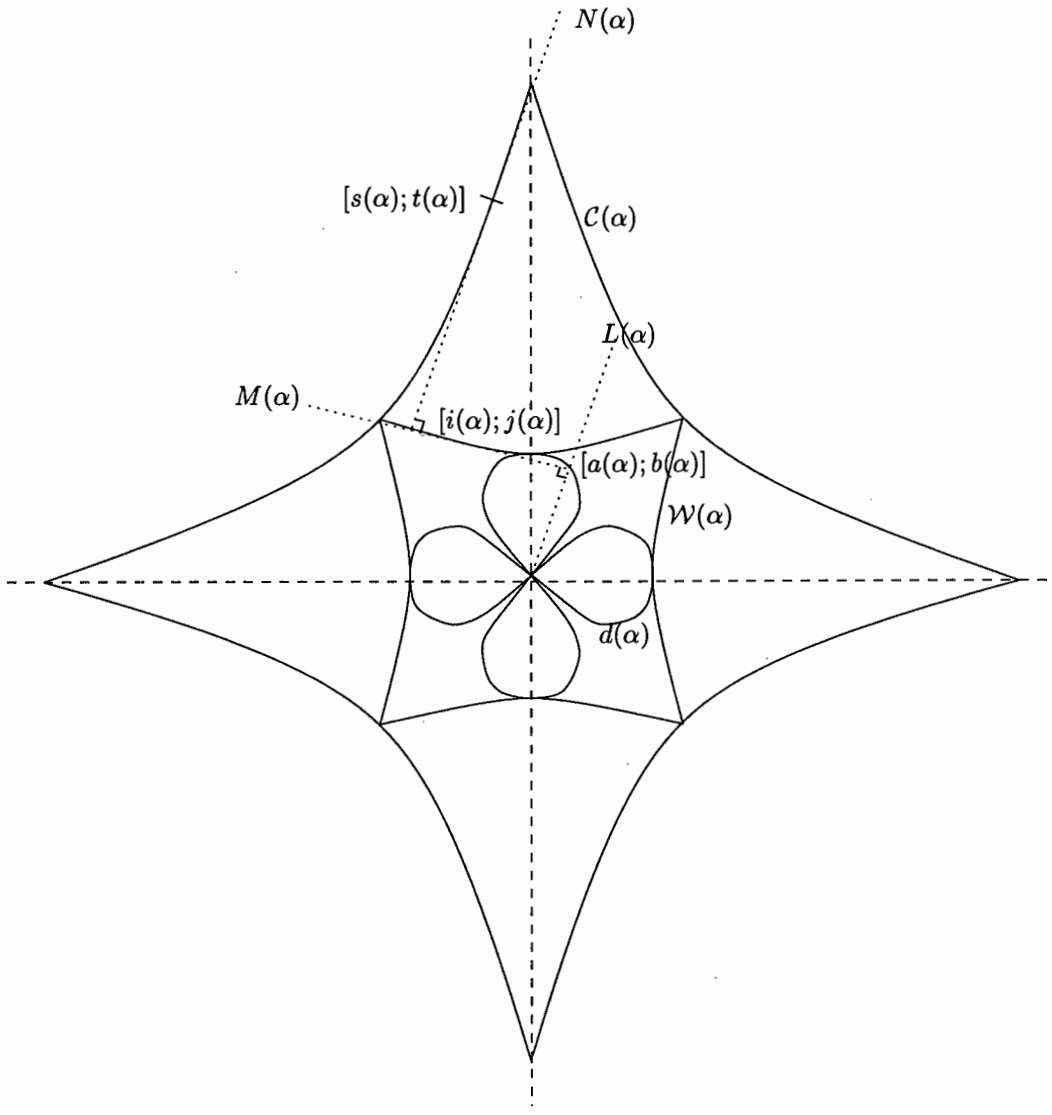

Figure 5.2: Diagram used to demonstrate the derivation techniques of the Caustic Curve equation, for the 'special case' geometric distance discrepancy function.

The first step in the caustic curve derivation is to construct the line $N(\alpha)$, perpendicular to $M(\alpha)$, through the point $[i(\alpha), j(\alpha)]$. The point of intersection between the straight line $N(\alpha)$ and the envelope of the caustic curve is labeled $[s(\alpha), t(\alpha)]$. The generalized equations for the parametric point $[s(\alpha), t(\alpha)]$ on the caustic curve are given in the previous section, Section 5.1 as equations 5.3 and 5.4.

In Section 3.1 the 'special case' geometric distance discrepancy function is written in the convenient form of:

$$\widehat{d_{G0}}(\alpha) = \cos 2\alpha$$

$$\Rightarrow \widehat{h_{G0}}(\alpha) = \widehat{d_{G0}}'(\alpha) = -2\sin 2\alpha$$
$$\Rightarrow \widehat{p_{G0}}(\alpha) = \widehat{d_{G0}}(\alpha) + \widehat{d_{G0}}''(\alpha) = \cos 2\alpha - 4\cos 2\alpha = -3\cos 2\alpha$$

A polar plot of the three distance components and the value table for $\widehat{p_G}(\alpha)$ is provided in the following figure, Figure 5.3. The value tables for $\widehat{h_G}(\alpha)$ and $\widehat{d_G}(\alpha)$ can be found in Figures 4.5 and 3.4 respectively.

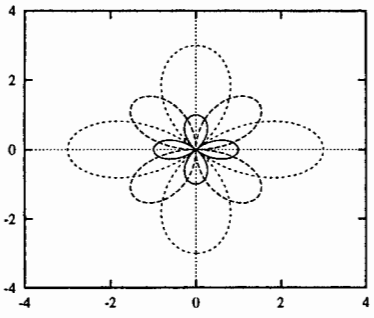

α	$\widehat{p_{G0}}(\alpha)$	α	$\widehat{p_{G0}}(\alpha)$
0^o	-3	180^o	-3
45^o	0	225^o	0
90^o	3	270^o	3
135^o	0	315^o	0

Figure 5.3: Polar plot of $\widehat{d_{G0}}(\alpha)$ (solid line), $\widehat{h_{G0}}(\alpha)$ (dashed line) and $\widehat{p_{G0}}(\alpha)$ (dotted line) and the value table for $\widehat{p_{G0}}(\alpha)$.

From the definition of $\widehat{p_{G0}}(\alpha)$ one knows that like $\widehat{d_{G0}}(\alpha)$ and $\widehat{h_{G0}}(\alpha)$, $\widehat{p_{G0}}(\alpha)$ is a quadrifolium, and because it is of the '$\cos 2\alpha$ family' the four loops were aligned with the north, south, east and west axis. Notice also that, while $\widehat{p_{G0}}(\alpha)$ has a magnitude three times that of $\widehat{d_{G0}}(\alpha)$ it is also opposite in sign, thus wherever $\widehat{d_{G0}}(\alpha)$ is positive $\widehat{p_{G0}}(\alpha)$ is negative and vice versa. Thus $\widehat{p_{G0}}(\alpha)$ is positive for the azimuthal range $\alpha \in [45^o; 135^o]$ and $\alpha \in [225^o; 315^o]$.

The functions $\widehat{d_{G0}}(\alpha)$ and $\widehat{h_{G0}}(\alpha)$ are discussed in detail with respect to Figure 3.3 in Chapter 3 and Figure 4.3 in Chapter 4 respectively. The three distance components, which contribute to the caustic curve, are overlayed in Figure 5.3, so as to demonstrate their respective contributions.

The initial position of the caustic distance component is at $\widehat{p_{G0}}(0^o) = -3$. As α increases from 0^o to 45^o so $\widehat{p_{G0}}(\alpha)$ increases from -3 to 0. In the same way that $\widehat{d_{G0}}(\alpha)$ and $\widehat{h_{G0}}(\alpha)$ have a clockwise orientation throughout the azimuthal range, so $\widehat{p_{G0}}(\alpha)$ has a clockwise rotation.

Returning to the problem at hand, which is to determine the caustic curve for the 'special case' geometric distance discrepancy function, the function $\widehat{d_{G0}}(\alpha)$ is substituted into the caustic curve equations, which are given at the end of the previous section as:

$$s(\alpha) = d'(\alpha)\cos\alpha - d''(\alpha)\sin\alpha$$
$$t(\alpha) = -d'(\alpha)\sin\alpha - d''(\alpha)\cos\alpha$$

Now $d'(\alpha) = -2\sin\alpha$ and $d''(\alpha) = -4\cos\alpha$ and the relevant caustic curve is described by the parametric points:

$$\widehat{s_{G0}}(\alpha) = -2.\sin 2\alpha.\cos\alpha + 4.\cos 2\alpha.\sin\alpha$$
$$\widehat{t_{G0}}(\alpha) = 2.\sin 2\alpha.\sin\alpha + 4.\cos 2\alpha.\cos\alpha$$

Which can be simplified to:

$$\widehat{\mathcal{C}_{G0}} := [\widehat{s_{G0}}(\alpha); \widehat{t_{G0}}(\alpha)] = [-4\sin^3\alpha; 4\cos^3\alpha]$$

Below the Cartesian graph of the caustic curve for the function $\widehat{d_{G0}}(\alpha)$ is plotted in Figure 5.4.

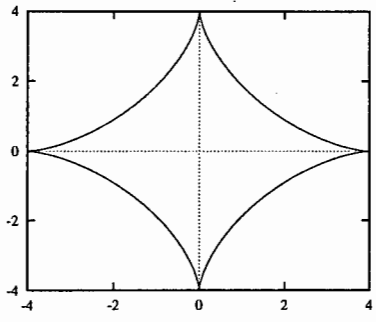

α	$(\widehat{s_{G0}}; \widehat{t_{G0}})$	α	$(\widehat{s_{G0}}; \widehat{t_{G0}})$
0^o	$0; 4$	180^o	$0; -4$
45^o	$-\sqrt{2}; \sqrt{2}$	225^o	$\sqrt{2}; -\sqrt{2}$
90^o	$-4; 0$	270^o	$4; 0$
135^o	$-\sqrt{2}; -\sqrt{2}$	315^o	$\sqrt{2}; \sqrt{2}$

Figure 5.4: Cartesian graph and value table for $\widehat{\mathcal{C}_{G0}}(\alpha)$.

Notice that when compared to the hypocycloid for the corresponding wavefront, $\widehat{\mathcal{W}_{\mathcal{G}}}(\alpha)$ in Figure 4.4, they are offset from each other by 45^o. Also, the outer radius of the caustic curve is 4 *units*, which is twice that of the outer radius of the $\widehat{\mathcal{W}_{\mathcal{G}}}(\alpha)$ outer radius, which is 2 *units*. This comparison corresponds exactly with Lockwood (1961), who demonstrated that the evolute of a hypocycloid with $(n+1)$ cusps is similar to the original hypocycloid, but enlarged by the ratio $(n+1) : (n-1)$ and rotated on the axis, from the original curve by 45^o. In this scenario the evolute of the four-cusped hypocycloid wavefront curve is another similar four-cusped hypocycloid with twice the magnitude of the original curve and rotated from the original curve by 45^o.

The octant table for $\widehat{\mathcal{C}_{G0}}(\alpha)$ is provided below in Table 5.1.

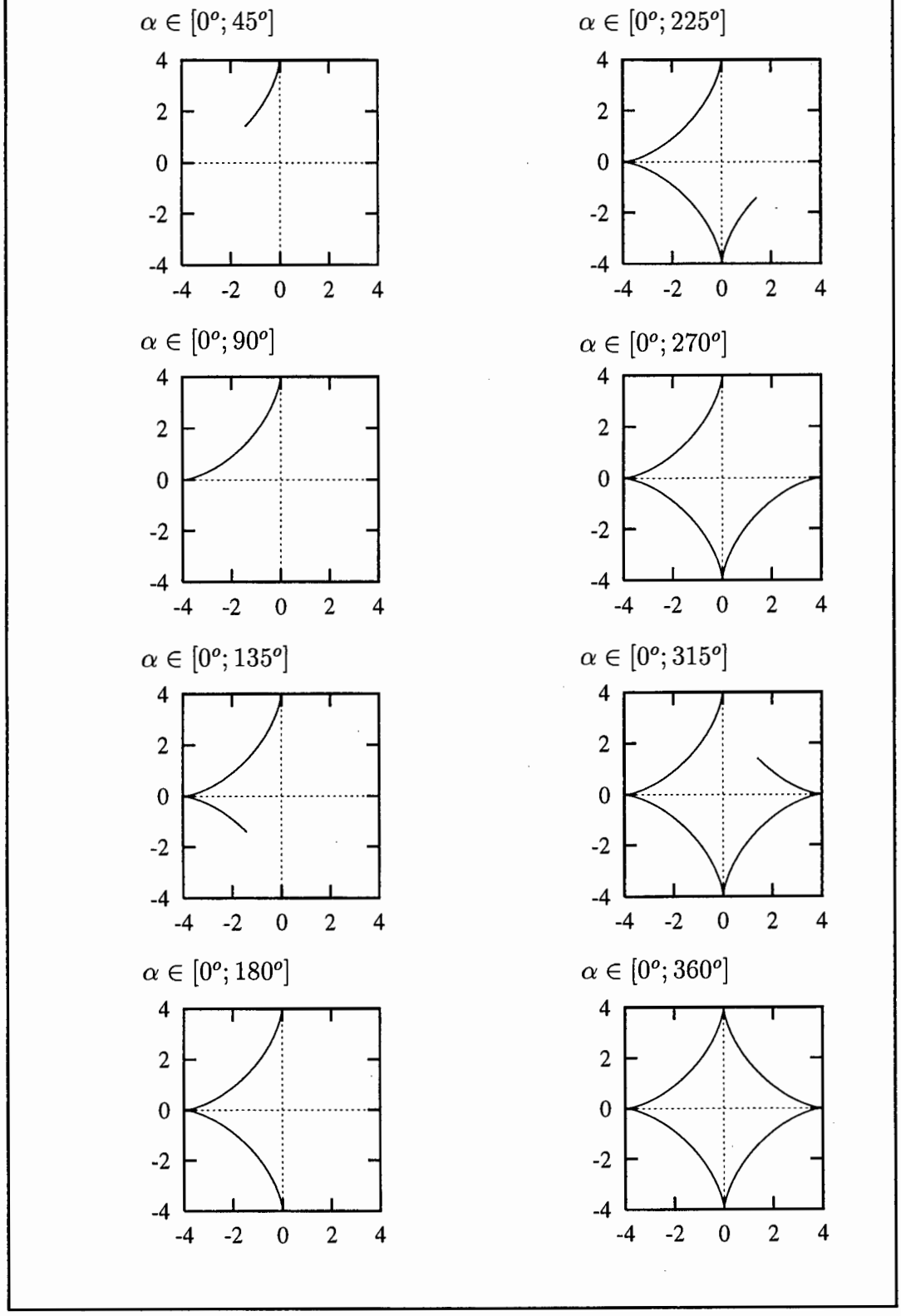

Table 5.1: Octant table for $\widehat{\mathcal{C}_{G0}}(\alpha)$.

The initial position of the caustic curve is at $\widehat{\mathcal{C}_{G0}}(0^o) = [0; 4]$. As α ranges from 0^o to 45^o so $\widehat{\mathcal{C}_{G0}}(\alpha)$ ranges from $[0; 4]$ to $[-\sqrt{2}; -\sqrt{2}]$. Continuing in this manner indicates the $\widehat{\mathcal{C}_{G0}}(\alpha)$ had an anticlockwise rotation, as did $\widehat{\mathcal{W}_{G0}}(\alpha)$.

At this stage the more general geometric distance discrepancy function is considered using the convenient scaled form of the function introduced in Section 3.1.

$$\begin{aligned} \widehat{d_G}(s, \lambda, \alpha) &= \widehat{A_G}(s, \lambda) + \cos 2\alpha \\ \Rightarrow \widehat{h_G}(\alpha) &= \widehat{d_G}'(\alpha) = -2 \sin 2\alpha \\ \Rightarrow \widehat{p_G}(s, \lambda, \alpha) = \widehat{d_G}(s, \lambda, \alpha) + \widehat{d_G}''(\alpha) &= \widehat{A_G}(s, \lambda) - 3 \cos 2\alpha \end{aligned}$$

The functions $\widehat{d_G}(\alpha)$ and $\widehat{h_G}(\alpha)$ were discussed previously in detail, with regard to Figures 3.4 and 4.5 respectively. Below in Figure 5.5, the functions $\widehat{d_G}(\alpha)$, $\widehat{h_G}(\alpha)$ and $\widehat{p_G}(\alpha)$ are plotted for the integral values of $\widehat{A_G}(\alpha) = -3; -2; \ldots; +2; +3$. Now $\widehat{h_G}(\alpha)$, as mentioned in Section 4.2, is invariant with respect to the distance of the approaching ray to or from the proxy origin and thus remain unchanged for all values of $\widehat{A_G}(\alpha)$. However $\widehat{d_G}(\alpha)$ and $\widehat{p_G}(\alpha)$ were both dependent on $\widehat{A_G}(\alpha)$ and thus experience a certain amount of variation as the ray approaches or departs from the antipodal region.

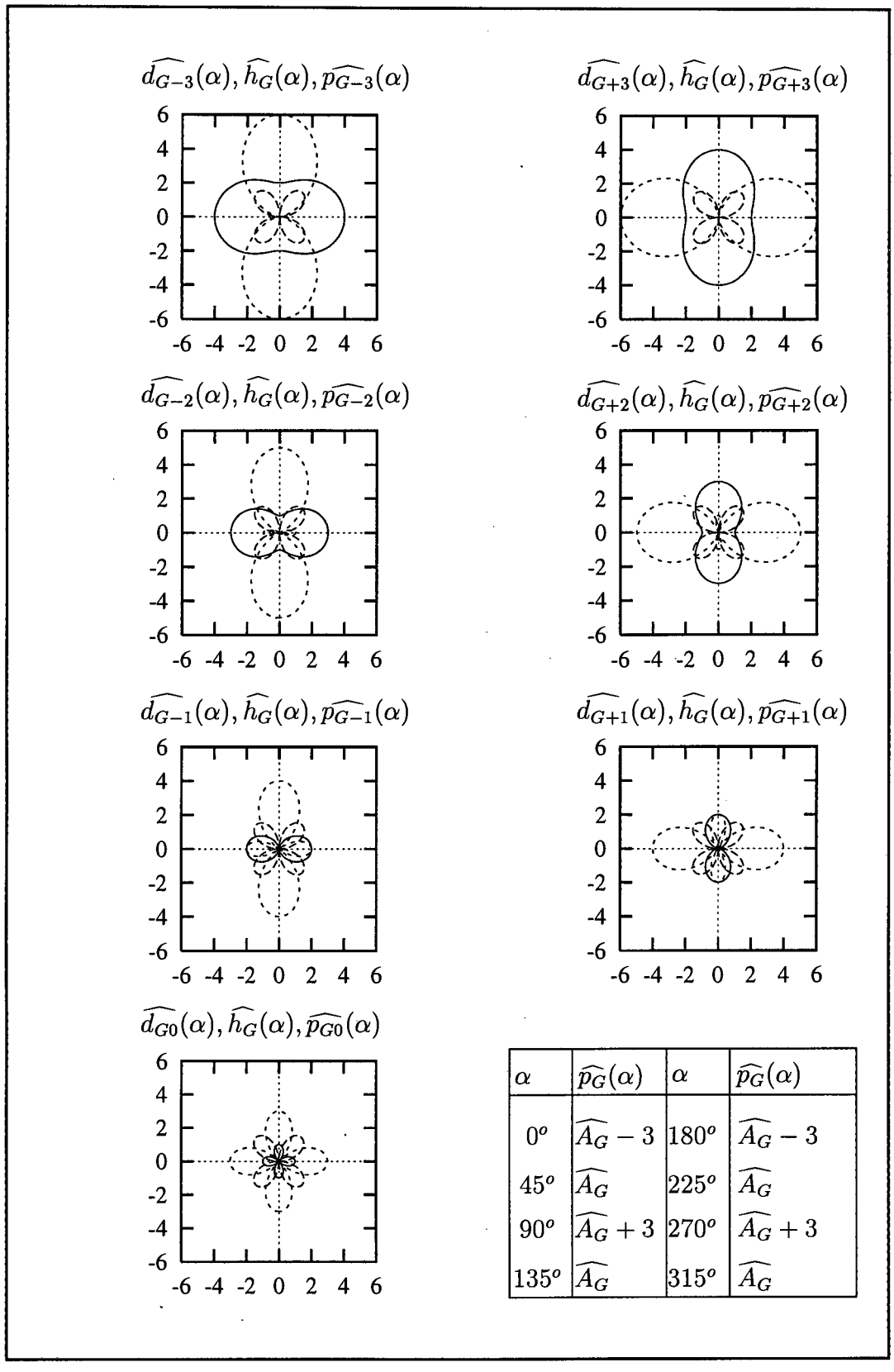

α	$\widehat{p_G}(\alpha)$	α	$\widehat{p_G}(\alpha)$
0^o	$\widehat{A_G} - 3$	180^o	$\widehat{A_G} - 3$
45^o	$\widehat{A_G}$	225^o	$\widehat{A_G}$
90^o	$\widehat{A_G} + 3$	270^o	$\widehat{A_G} + 3$
135^o	$\widehat{A_G}$	315^o	$\widehat{A_G}$

Figure 5.5: Polar plot of $\widehat{d_G}(\alpha)$ (solid line), $\widehat{h_G}(\alpha)$ (dashed line) and $\widehat{p_G}(\alpha)$ (dotted line) and the value table for $\widehat{p_G}(\alpha)$.

As mentioned before, $\widehat{d_G}(\alpha)$ and $\widehat{h_G}(\alpha)$ are discussed in detail in Sections 3.1 and 4.2 respectively, at this stage the functions: $\widehat{p_{G-3}}(\alpha); \widehat{p_{G-2}}(\alpha); \ldots; \widehat{p_{G+2}}(\alpha); \widehat{p_{G+3}}(\alpha)$ are considered in detail.

Again, as for all the other distance components, all the $\widehat{p_G}(\alpha)$ functions are continuous throughout the azimuthal range. As for the $\widehat{d_G}(\alpha)$ function that is also dependent on $\widehat{A_G}(\alpha)$, $\widehat{p_G}(\alpha)$ passes through a series of phases as the ray approaches and departs from the proxy origin.

As the ray approaches the proxy antipodal point, so the plots of $\widehat{p_G}(\alpha)$ are aligned along the north-south axis. For rays departing from the antipodal region ($\widehat{A_G} > 0$) the plots of $\widehat{p_G}(\alpha)$ are aligned with the west-east axis.

For $|\widehat{A_G}| = 3$ the function $\widehat{p_{G\pm3}}(\alpha)$ presents a plot in the form of a lemniscate. The function of the lemniscate was discussed previously in Section 2.2 with regard to the distance discrepancy functions $\widehat{d_{G\pm1}}(\alpha)$.

For $|\widehat{A_G}| = 0$, $\widehat{p_{G0}}(\alpha)$ is a quadrifolium with same form as $\widehat{d_{G0}}(\alpha)$, only $\widehat{p_{G0}}(\alpha)$ has a magnitude three times that of $\widehat{d_{G0}}(\alpha)$.

For $0 < |\widehat{A_G}| < 3$ the transition of $\widehat{p_G}(\alpha)$ between a lemniscate and a quadrifolium can be observed. For $|\widehat{A_G}| = 2$ the $\widehat{p_G}(\alpha)$ function is still dominated by the lemniscate component, but for $|\widehat{A_G}| = 1$ the $\widehat{p_{G\pm1}}(\alpha)$ function is clearly tending to a quadrifolium.

Apart from the form of the $\widehat{p_G}(\alpha)$ functions each function has the same value table, corresponding to the relevant value of $\widehat{A_G}$. Thus, $\widehat{p_G}(0^o) = \widehat{A_G} - 3$. Also, $\widehat{p_G}(\alpha)$ is opposite in sign to $\widehat{d_G}(\alpha)$ and is thus a positive function for the azimuthal range $\alpha \in [45^o; 135^o]$ and $\alpha \in [225^o; 315^o]$.

Also, in the same way that $\widehat{d_G}(\alpha)$ and $\widehat{\mathcal{W}_G}(\alpha)$ approached and departed from the antipodal region along an azimuthal line, so $\widehat{p_G}(\alpha)$ had the same approach.

Substituting the distance components into the parametric equations for the caustic curve yields:

$$\widehat{s_G}(\alpha) = -2\sin 2\alpha.\cos\alpha + 4\cos 2\alpha.\sin\alpha$$
$$\widehat{t_G}(\alpha) = 2\sin 2\alpha.\sin\alpha + 4\cos 2\alpha.\cos\alpha$$

which was reduced to the equation:

$$\widehat{\mathcal{C}_G}(\alpha) = [\widehat{s_G}(\alpha); \widehat{t_G}(\alpha)] = [-4\sin^3\alpha; 4\cos^3\alpha]$$

Notice that the curve $\widehat{\mathcal{C}_G}(\alpha)$ is independent of any variance with regard to $\widehat{A_G}$, in fact $\widehat{\mathcal{C}_G}(\alpha)$ is the same function as $\widehat{\mathcal{C}_{G0}}(\alpha)$. This is because the equations for $\widehat{s_G}(\alpha)$ and $\widehat{t_G}(\alpha)$ rely upon $\widehat{d_G}'(\alpha)$ and $\widehat{d_G}''(\alpha)$ only. Also for this family of distance discrepancy functions the first and second derivatives are independent of any variance associated with the $\widehat{A_G}$ term of the $\widehat{d_G}$ function.

The graph of the caustic curve for $\widehat{d_G}(\alpha)$ function is clearly the same as that for the $\widehat{d_{G0}}(\alpha)$ function and is plotted below as Figure 5.6 for completeness.

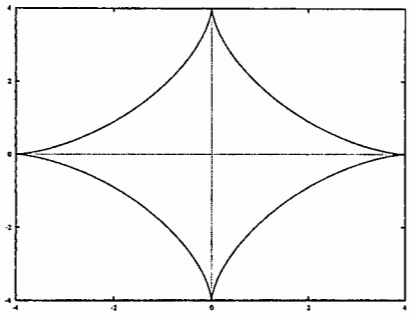

α	$(\widehat{s_G};\widehat{t_G})$	α	$(\widehat{s_G};\widehat{t_G})$
0^o	$0;4$	180^o	$0;-4$
45^o	$-\sqrt{2};\sqrt{2}$	225^o	$\sqrt{2};-\sqrt{2}$
90^o	$-4;0$	270^o	$4;0$
135^o	$-\sqrt{2};-\sqrt{2}$	315^o	$\sqrt{2};\sqrt{2}$

Figure 5.6: Cartesian graph and value table of $\widehat{\mathcal{C}_G}(\alpha)$.

The observations made for the caustic curve regarding the distance discrepancy function $\widehat{d_{G0}}(\alpha)$ hold for the '$+\cos 2\alpha$ family' of geometric distance discrepancy functions and are discussed in detail with regard to Figure 5.4.

It is a consequence of the definition of the caustic curve that all members of a wavefront family, for instance those associated with the geometric distance discrepancy function, which are plotted in Figure 4.6, all have the same caustic. This indicates that all these curves also have the same evolute curve, that of a four-cusped hypocycloid, with the four cusps aligned towards the north, west, south and east.

The paragraph above concludes the discussion regarding the caustic curve associated with the geometric distance discrepancy function. At this stage the caustic curve associated with the refractive distance discrepancy function $\widehat{d_R}(\alpha)$ is considered. Here:

$$\begin{aligned} \widehat{d_R}(\alpha) &= 1-\cos 2\alpha \\ \Rightarrow \widehat{h_R}(\alpha) &= \widehat{d_R}'(\alpha) = 2\sin 2\alpha \\ \Rightarrow \widehat{p_R}(\alpha) &= \widehat{d_R}(\alpha) + \widehat{d_R}''(\alpha) = 1-\cos 2\alpha + 4\cos 2\alpha = 1+3\cos 2\alpha \end{aligned}$$

Since $\widehat{d_R}(\alpha)$ is invariant with respect to the distance parameter s, for a given latitude, the refractive distance discrepancy function is the same for all approaches to or from the antipodal region. Now for $\widehat{p_R}(\alpha)$, which is by definition dependent on $\widehat{d_R}(\alpha)$, is consequently found to be the same for all approaches to and from the antipodal point.

As for the previous scenarios a polar plot is provided below of the functions $\widehat{d_R}(\alpha)$, $\widehat{h_R}(\alpha)$ and $\widehat{p_R}(\alpha)$ in Figure 5.7. The value table for $\widehat{p_R}(\alpha)$ is also included in Figure 5.7, while the value tables for $\widehat{h_R}(\alpha)$ and $\widehat{d_R}(\alpha)$ are included in Figures 4.7 and 3.6 respectively.

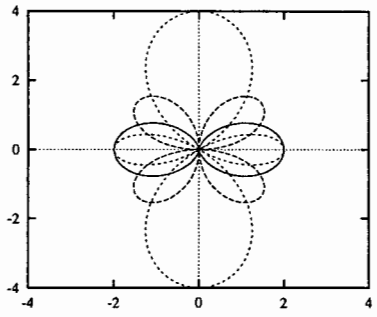

α	$\widehat{p_R}(\alpha)$	α	$\widehat{p_R}(\alpha)$
0^o	4	180^o	4
45^o	1	225^o	1
90^o	-2	270^o	-2
135^o	1	315^o	1

Figure 5.7: Polar plot of $\widehat{d_R}(\alpha)$ (solid line), $\widehat{h_R}(\alpha)$ (dashed line) and $\widehat{p_R}(\alpha)$ (dotted line) and value table for $\widehat{p_R}(\alpha)$.

The graph of the functions $\widehat{d_R}(\alpha)$ and $\widehat{h_R}(\alpha)$ are discussed in more detail with regard to Figure 4.7.

Now substituting the distance components into the caustic curve equations yield the curve:

$$\widehat{s_R}(\alpha) = 2\sin 2\alpha.\cos\alpha - 4\cos 2\alpha.\sin\alpha$$
$$\widehat{t_R}(\alpha) = -2\sin 2\alpha.\sin\alpha - 4\cos 2\alpha.\cos\alpha$$

These equations are rewritten in the following simplified form:

$$\widehat{\mathcal{C}_R}(\alpha) = [\widehat{s_R}(\alpha); \widehat{t_R}(\alpha)] = [4\sin^3\alpha; -4\cos^3\alpha]$$

The caustic curve for the refractive distance discrepancy function is plotted below in Figure 5.8, with the associated value table.

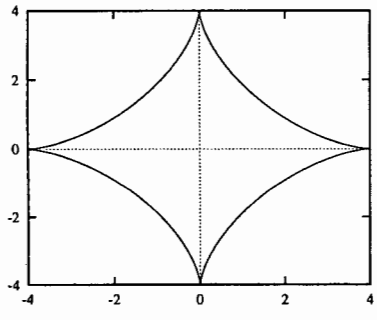

α	$(\widehat{s_R}; \widehat{t_R})$	α	$(\widehat{s_R}; \widehat{t_R})$
0^o	$0; -4$	180^o	$0; 4$
45^o	$\sqrt{2}; -\sqrt{2}$	225^o	$-\sqrt{2}; \sqrt{2}$
90^o	$4; 0$	270^o	$-4; 0$
135^o	$\sqrt{2}; \sqrt{2}$	315^o	$-\sqrt{2}; -\sqrt{2}$

Figure 5.8: Cartesian graph and value table of $\widehat{\mathcal{C}_R}(\alpha)$.

The graph of $\widehat{\mathcal{C}_R}(\alpha)$ is a four cusped hypocycloid, with cusps lying to the north, west, south and east. This graph appears to be the same as that of $\widehat{\mathcal{C}_G}(\alpha)$, which is not surprising since that graph (in Figure 5.6) demonstrates that the wavefront $\widehat{\mathcal{W}_{G-1}}(\alpha)$ (shown in Figure 4.6) has a caustic curve of this form and the wavefronts $\widehat{\mathcal{W}_{G-1}}(\alpha)$ and $\widehat{\mathcal{W}_R}(\alpha)$ have similar appearances, which are discussed with regard to Figure 4.8.

The octant table associated with $\widehat{\mathcal{C}_R}(\alpha)$ is provided below in Table 5.2 in order to clarify the differences between $\widehat{\mathcal{C}_G}(\alpha)$ and $\widehat{\mathcal{C}_R}(\alpha)$.

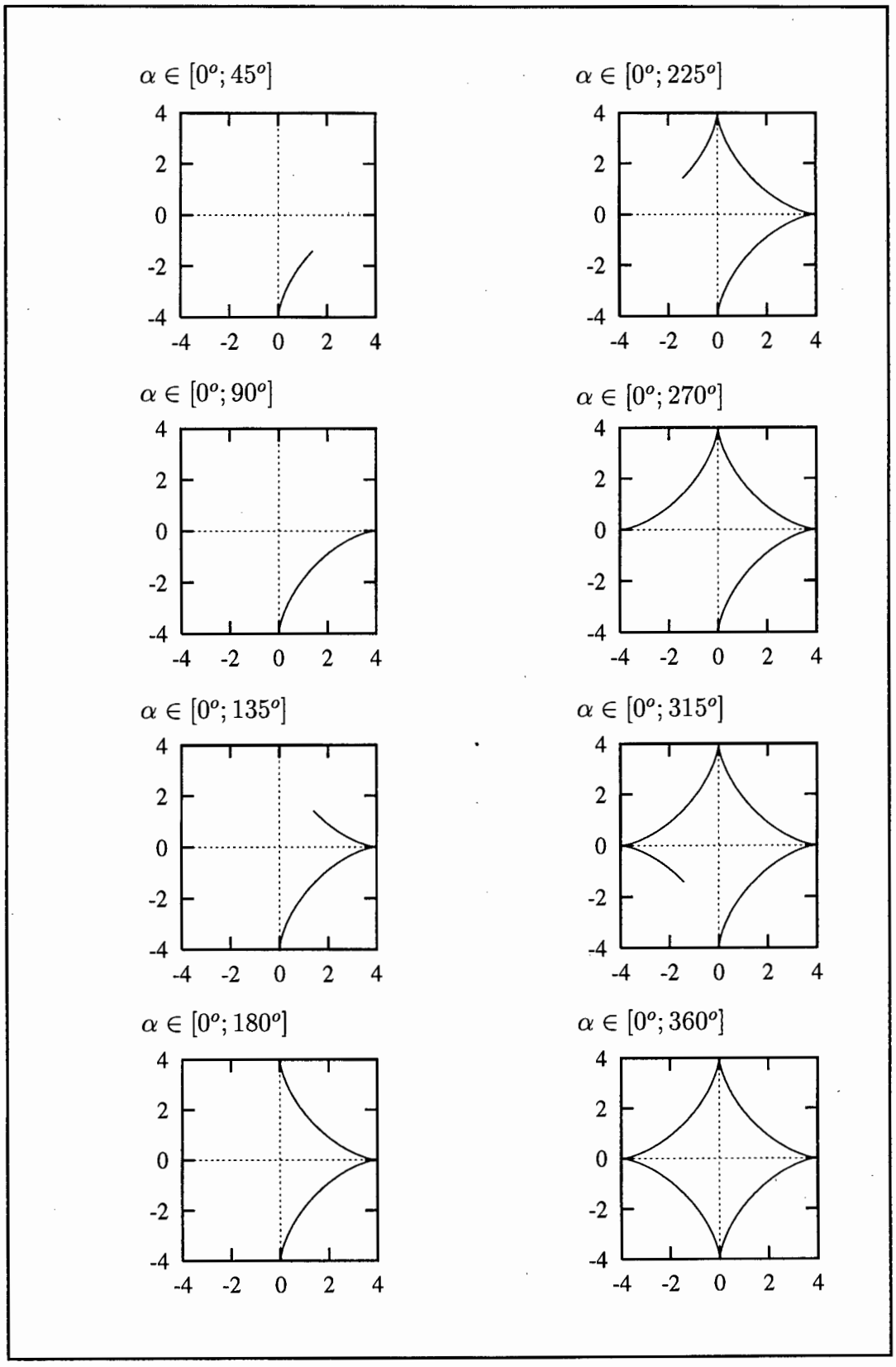

Table 5.2: Octant table for $\widehat{\mathcal{C}_R}(\alpha)$.

The graphs $\widehat{\mathcal{C}_R}(\alpha)$ and $\widehat{\mathcal{C}_G}(\alpha)$ appear to be the same, they have the same form and an anticlockwise orientation. However they do have different initial positions: $\widehat{\mathcal{C}_G}(0^o) = [0; 4]$ and $\widehat{\mathcal{C}_R}(0^o) = [0; -4]$.

The octant table, Table 4.2 and the octant table above indicate caustic curves with an anticlockwise orientation. However, the values of $\widehat{s_R}(\alpha)$ and $\widehat{t_R}(\alpha)$ are opposite in sign to those of $\widehat{s_G}(\alpha)$ and $\widehat{t_G}(\alpha)$, this is reflected in the relevant octant table, by the functions being 180^o out of phase from each other.

Chapter 6

Discussion

In this Chapter an overview of the results is presented, specifically with reference to the thesis objective. These results are then extended to present new ideas regarding antipodal receptions in global propagation studies and thus to contribute to the new scientific discipline of Global Acoustic Propagation.

In the first section a review of the thesis results is presented in order to place the discussion which follows in context. Thereafter, the thesis objective is reconsidered, specifically with regard to the thesis results. Final conclusions with regard to antipodal receptions are provided. With regard to the thesis objective the antipodal algorithm is reviewed and the results of the antipodal algorithm under the geometric assumption and the refractive assumption are considered in detail. Also, a comparative study between the geometric results and the refractive results is included, in order to demonstrate the effective contribution of each of these assumptions to the nature of the antipodal region. The refractive assumption is shown to dominate the geometric assumption and is then used in a case study regarding the ATOC source at Pioneer Seamount.

6.1 Review

In Chapter 1 the setting for this thesis was provided in the form of a historical review of previous global range underwater acoustic propagation studies, particularly to antipodal ranges. From the historical background it is quite clear that there are two major contributions, apart from bathymetric blocking, that are essential to the determination of the antipodal region. Firstly the contribution due to the form of the earth and secondly the contribution due to horizontal refraction within the world oceans.

By way of introduction to the thesis, the necessary acoustic theory was also provided in Chapter 1. This theory provides the background to the understanding of axial sound propagation in terms of ray tracing techniques and normal mode theory. In global propagation studies it is appropriate to consider axial sound propagation, since the vertical depth is negligible when considering the large horizontal ranges involved (Dworski and Mercer 1990). An additional section regarding the notation is included in Chapter 1 in order to provide the necessary background for the remainder of the thesis.

In Chapter 2 the effects due to the form of the earth and horizontal sound speed variability were considered in detail. Two assumptions were established: Firstly the geometric assumption, which refers to a more realistic spheroidal earth, as opposed to a sphere, in a range independent sound speed environment; and secondly a more realistic range dependent sound speed environment, imposed on

a spherical earth. The range dependent environment was included as a latitudinal model of sound slowness.

Chapters 3, 4 and 5 provided the antipodal algorithm, which begins with the development of the distance discrepancy function in Chapter 3. The distance discrepancy function was determined under both the geometric and the refractive assumptions. Both involve Fermat paths, the first in distance and the second in time. The two assumptions were considered separately, so that ultimately the effective contribution of both of these assumptions to the antipodal region can be determined. The sign of the distance discrepancy function was used in the following chapter to determine whether a wavefront is approaching or departing from the antipodal region.

In Chapter 4 the geometrical study of Longuet-Higgins (1990) was used to determine an analytical method for determining the wavefront family for a given distance discrepancy function. The wavefront was defined as that curve orthogonal to the approaching rays for the complete azimuthal range, at a particular time or distance from the source. The wavefronts associated with both the geometric and refractive assumptions were derived in terms of the analytical method. The wavefronts evolve as a sequence of delightful geometric curves containing elements of both convergence and divergence in their patterns. The results under the geometric assumption corresponded to those of Longuet-Higgins (1990) and thus verify the analytical approach.

The results of Chapter 4 indicated that under the geometric assumption, the wavefront sectors which approach from the poles reach the antipodal region prior to those sectors approaching along the equator, which have the further distance to travel. However, under the refractive assumption the polar paths propagate through slower waters than the warm equatorial waters and thus those wavefront sectors approaching antipodal region from the poles arrive after those approaching along the equator.

Chapter 5 continued with the development of the algorithm by determining the caustic curve equation for a given wave function, and hence for a given distance discrepancy function. The caustic curve refers to the ray envelope close to the antipodal region. From this definition, where rays are everywhere orthogonal to wavefronts, it is seen that any single member of the family of wavefronts is sufficient to provide the caustic curve associated with the entire family of wavefronts.

The caustic curve equations were determined under both the geometric and the refractive assumptions. Again the analytical derivation of the caustic curve with regard to the geometric assumption correspond well with Longuet-Higgins (1990) and thus verify the antipodal algorithm. The resulting caustic curves under both assumptions yield a four-cusped hypocycloid, with cusps aligned with the north-south and west-east axis. However the arcs of the caustic associated with rays from any particular direction differed between the two cases.

6.2 The Antipodal Algorithm

At this stage it is important to restate the objective of this thesis in order to discuss how the preceding results have achieved them. The principal objective of this thesis is to examine antipodal receptions in underwater acoustics and more specifically to develop a general algorithm to determine the nature of the antipodal region under certain physical assumptions. This is achieved in that an analytical antipodal algorithm is derived, using the methodology of Longuet-Higgins (1990).

The algorithm is provided here for completeness, aspects of it have been provided in the relevant preceding chapters. Beginning with a distance discrepancy function, $d(\alpha)$, specified for each approaching azimuthal angle, the corresponding wavefront, $\mathcal{W}(\alpha)$, is determined and in turn the corresponding caustic curve, $\mathcal{C}(\alpha)$ is established.

$$distance\ discrepancy\ function := d(\alpha)$$

$$\downarrow$$

$$\mathcal{W}(\alpha) := [d(\alpha).\sin\alpha + d'(\alpha).\cos\alpha; d(\alpha).\cos\alpha - d'(\alpha).\sin\alpha]$$

$$\downarrow$$

$$\widehat{\mathcal{C}_G}(\alpha) := [d'(\alpha).\cos\alpha - d''(\alpha).\sin\alpha; -d'(\alpha).\sin\alpha - d''(\alpha).\cos\alpha]$$

An important feature of the generalized algorithm is that calculations can be carried out, using realistic assumptions and their corresponding distance discrepancy functions, in order to determine the nature of the antipodal region for a number of scenarios.

In this study sound propagation along axial paths is examined. However, the refractive assumption could certainly be adapted to higher order normal modes, in the same way that first order propagation was considered here (Heaney, Kuperman, and McDonald 1991). A higher mode interpretation results in a different refractive distance discrepancy function which can be included into the generalized antipodal algorithm. The detail regarding higher order mode distance discrepancy functions is certainly different to the first order study done here, as would be the interpretation of the results. Even so, the generalized nature of the antipodal algorithm means that this extension does not involve new concepts.

Two model assumptions were considered in this thesis and included into the antipodal algorithm. Firstly the geometric assumption, which refers to a spheroidal earth and a range independent sound environment. This model is not new and has been examined previously in detail by Longuet-Higgins (1990). However the analytical approach for the antipodal algorithm provided a new analytical as opposed to geometrical methodology, and the results compared favorably with those of Longuet-Higgins (1990), thus verifying the algorithm.

The second assumption refers to the refractive assumption, which assumes a range dependent sound environment on a spherical earth. The range dependence is included as a sound slowness model, which is a function of latitude only. This assumption makes use of the methodology of the generalized antipodal algorithm and thus provides insights into the study of antipodal receptions.

The definition of the distance discrepancy function, $d_R(\alpha)$, in the refractive case shows its clear relation with the time delay ΔT. The value of ΔT varies from zero for the polar route and becomes more and more negative as the ray moves from high latitudes into the tropics. Thus, $d_R(\alpha)$ plotted in Figure 3.6, is zero for the polar route ($\alpha = 0^o$) and increases as α increases towards the tropical path ($\alpha = 90^o$).

There is a clear analogy between ΔT, and hence $d_R(\alpha)$, and the ray time delay or action, A, as defined by Munk, Worcester, and Wunsch (1995). For rays propagating in the vertical A will take on the value zero for a ray which follows the sound axis, and increase for more and more steeply angled rays. The action, A, plays a fundamental role in the description of ray propagation in the vertical plane in the same way that the distance discrepancy function is fundamental to the description of horizontal refraction into the antipodal region.

Steeply angled rays will sample much of the water column on either side of the sound channel axis and the action incorporates environmental information from this water column. So-called anomalous and normal stratification profiles are characterized by Munk, Worcester, and Wunsch (1995) in terms of the second derivative of the action:

$\frac{\partial^2 A}{\partial S^2} > 0$ normal sound channel (axial rays last)
$\frac{\partial^2 A}{\partial S^2} < 0$ abnormal sound channel

In an analogous way the second derivative of the distance discrepancy enters the distance function $p(\alpha) = d(\alpha) + d''(\alpha)$, which determines the convergence, $p(\alpha) < 0$, or divergence, $p(\alpha) > 0$, of the wavefront away from a caustic point.

6.3 The Caustic Dimensions

The actual dimensions of the antipodal regions under both the geometric and refractive assumptions, individually, can be obtained by reversing the earlier scaling. Thus a comparison is made regarding the effective contributions of each of the assumptions to the nature of the antipodal region.

The unscaled geometric distance discrepancy function is defined in Section 3.1 as:

$$d_G(s, \lambda, \alpha) = A_G(s, \lambda) + B_G(\lambda).\cos 2\alpha$$

This function is substituted into the caustic curve equations and after simplification can be written in the form:

$$\mathcal{C}_G(\lambda, \alpha) = [-4.B_G(\lambda).\sin^3\alpha; 4.B_G(\lambda).\cos^3\alpha]$$

Where: $B_G(\lambda) := \frac{\pi}{4}.f.a.\cos^2\lambda$. From Section 2.1, $a = 6\ 378\ 137\ m$ and $f = 0.003353$. Thus:

$$\mathcal{C}_G(\lambda, \alpha) = [-67\ 185.77\cos^2\lambda\sin^3\alpha; 67\ 185.77\cos^2\lambda\cos^3\alpha]$$

The largest outer radial distance for the hypocycloidal caustic in the case of an equatorial source is just over $67\ km$, in agreement with the results of Longuet-Higgins (1990).

Similarly, the unscaled refractive distance discrepancy function is defined in Section 3.2 as:

$$d_R(\lambda, \alpha) = A_R(\lambda) + B_R(\lambda).\cos 2\alpha$$

As in the geometric case, this function is substituted into the caustic curve equations and after simplification can be written in the form:

$$\mathcal{C}_R(\lambda, \alpha) = [4.B_R(\lambda).\sin^3\alpha; -4.B_R(\lambda).\cos^3\alpha]$$

Where: $B_R(\lambda) := \frac{\pi RA}{2S_o}\cos^2\lambda$. From Section 2.2, $\mathcal{A} = 10.3E-6$ and $S_o = 684.1E-6$. Also, the mean earth radius is defined as $R = 6.37E+6$ in Section 2.1. Thus:

$$\mathcal{C}_R(\lambda,\alpha) = [602\ 610.8\cos^2\lambda\sin^3\alpha; -602\ 610.8\cos^2\lambda\cos^3\alpha]$$

In this case the largest outer radial distance for the hypocycloidal caustic curve, in the case of an equatorial source is over $602\ km$.

Clearly the magnitude of the refractive caustic curve is far greater than that of the geometric caustic curve, in fact:

$$|\mathcal{C}_G| : |\mathcal{C}_R| \simeq |1 : 8.97|$$

Thus the antipodal region associated with the refractive distance discrepancy function is close to ten times that of the geometric distance discrepancy function. From this analysis it is clear that the refractive effect dominates the geometric effect. This indicates that, while the form of the earth is considered to be an important effect in the literature, the refractive effect on antipodal receptions is of far more concern.

6.4 Refractional Wavefronts

Clearly the details regarding the resulting refractive antipodal region should be considered in more detail than those for the geometrical antipodal region. The particulars regarding the geometric results are provided in detail in the relevant chapters. However under the refractive assumption only one member of the wavefront is derived. This is not a short fall in the study, rather the results associated with the refractive effect can be deduced by analogy with the results for the geometric effect.

In fact, under the geometric assumption a complete 'time-framework' for rays and thus wavefronts is provided. It is also shown in Chapter 5 that given any member of the relevant family of wavefronts the associated caustic curve can be determined. Thus under the refractive assumption where only one 'frame' in the total 'time-framework' is deduced the caustic curve is derived without difficulty.

It is important to notice that even though only one frame in the total 'time-framework' is available under the refractive assumption, the remaining 'time-framework' can be determined by analogy with the results under the geometric assumption.

The Cartesian graph including the family of wavefronts associated with the geometric assumption was included in Figure 4.6. The family of wavefronts associated with the refractive scenario is deduced by analogy from the family of wavefronts and is presented below in Figure 6.1.

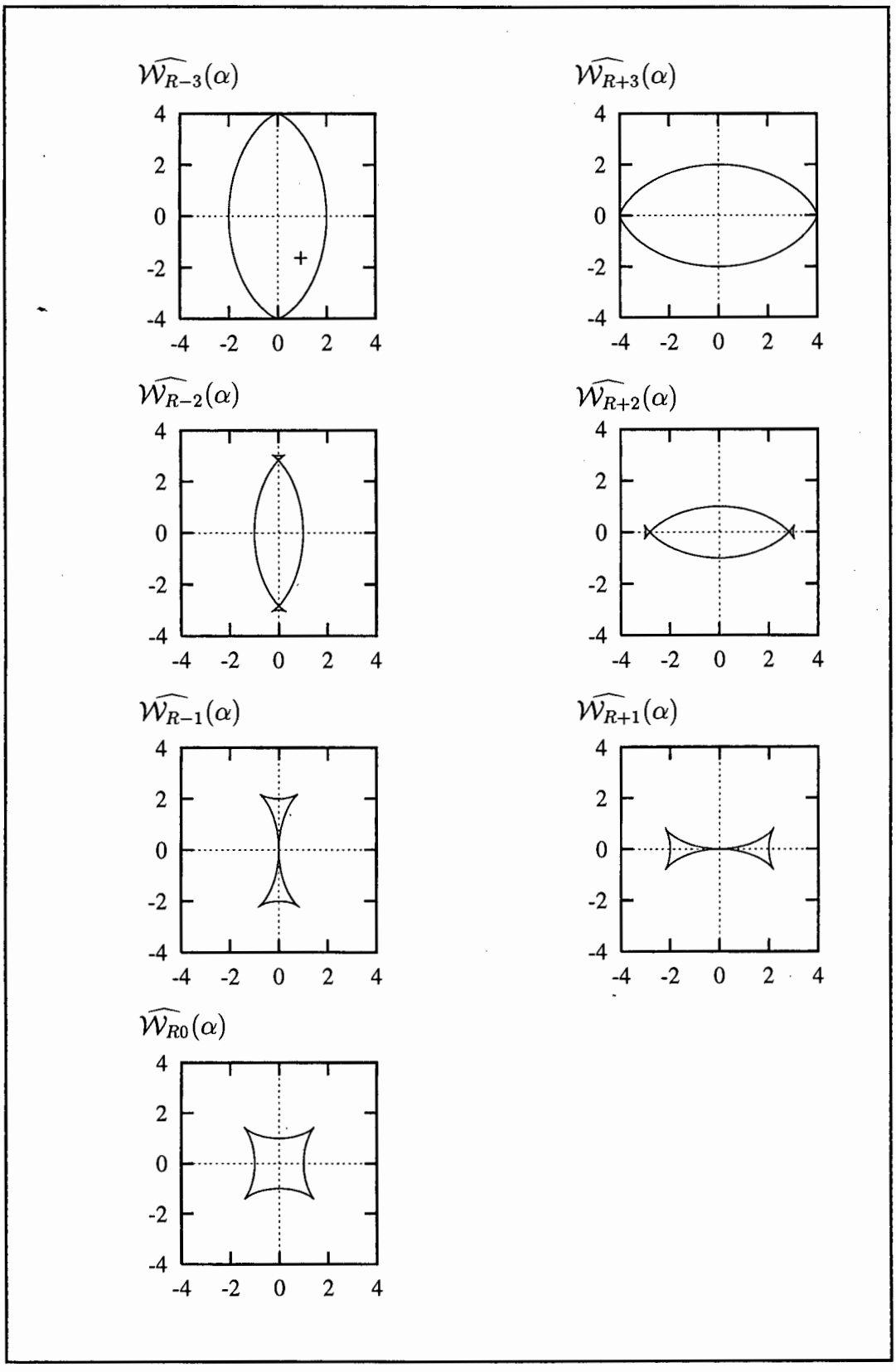

Figure 6.1: Cartesian graph of the $\widehat{\mathcal{W}_R}(\alpha)$ family.

The specific wave function, presented in Chapter 4 corresponds to the $\widehat{\mathcal{W}_{R+1}}(\alpha)$. The earliest wavefront $\widehat{\mathcal{W}_{R-3}}(\alpha)$ shows converging wavefronts from both sides with the tropics in advance of the polar sectors. Thereafter, the polar sectors begin to diverge (see $\widehat{\mathcal{W}_{R-2}}(\alpha)$ and $\widehat{\mathcal{W}_{R-1}}(\alpha)$ etc.) away from their caustic points. The tropical sectors continue to converge, even past the central point. $\widehat{\mathcal{W}_{R+3}}(\alpha)$ represents the wavefront at the time when the tropical sector reaches its caustic and the entire wavefront is diverging.

Longuet-Higgins (1990) describes the arrival structure of the rays both within and outside the antipodal region in detail for the geometric case. The arrival pattern for a point in the antipodal range for the refractive case can be determined from Figure 6.1. The procedure is illustrated for the point marked + in the second quadrant. The first arrival at this point occurs between $\widehat{\mathcal{W}_{R-2}}(\alpha)$ and $\widehat{\mathcal{W}_{R-1}}(\alpha)$ as the westward converging tropical wavefront passes the point. The second arrival is between $\widehat{\mathcal{W}_{R-1}}(\alpha)$ $\widehat{\mathcal{W}_{R0}}(\alpha)$ from the eastward converging tropical wavefront. The passage of the two diverging polar arcs of the wavefront occur in a northward direction between $\widehat{\mathcal{W}_{R0}}(\alpha)$ and $\widehat{\mathcal{W}_{R+1}}(\alpha)$ and from the southward wavefront between $\widehat{\mathcal{W}_{R+1}}(\alpha)$ and $\widehat{\mathcal{W}_{R+2}}(\alpha)$. It is likely that greater acoustic energy receptions will be associated with the converging arrivals than the diverging arrivals.

6.5 Caustic Receptions in Space and Time

At this stage there has been no observational evidence concerning the amplification of sound signals at antipodal receptions (Munk, Worcester, and Wunsch 1995), but acoustic intensities are expected to be high along the caustic curve and even higher at any of the four hypocycloidal cusps. The octant table, Table 5.2, of the refractive caustic curve, is repeated below in Table 6.1 in order to aid the discussion which follows.

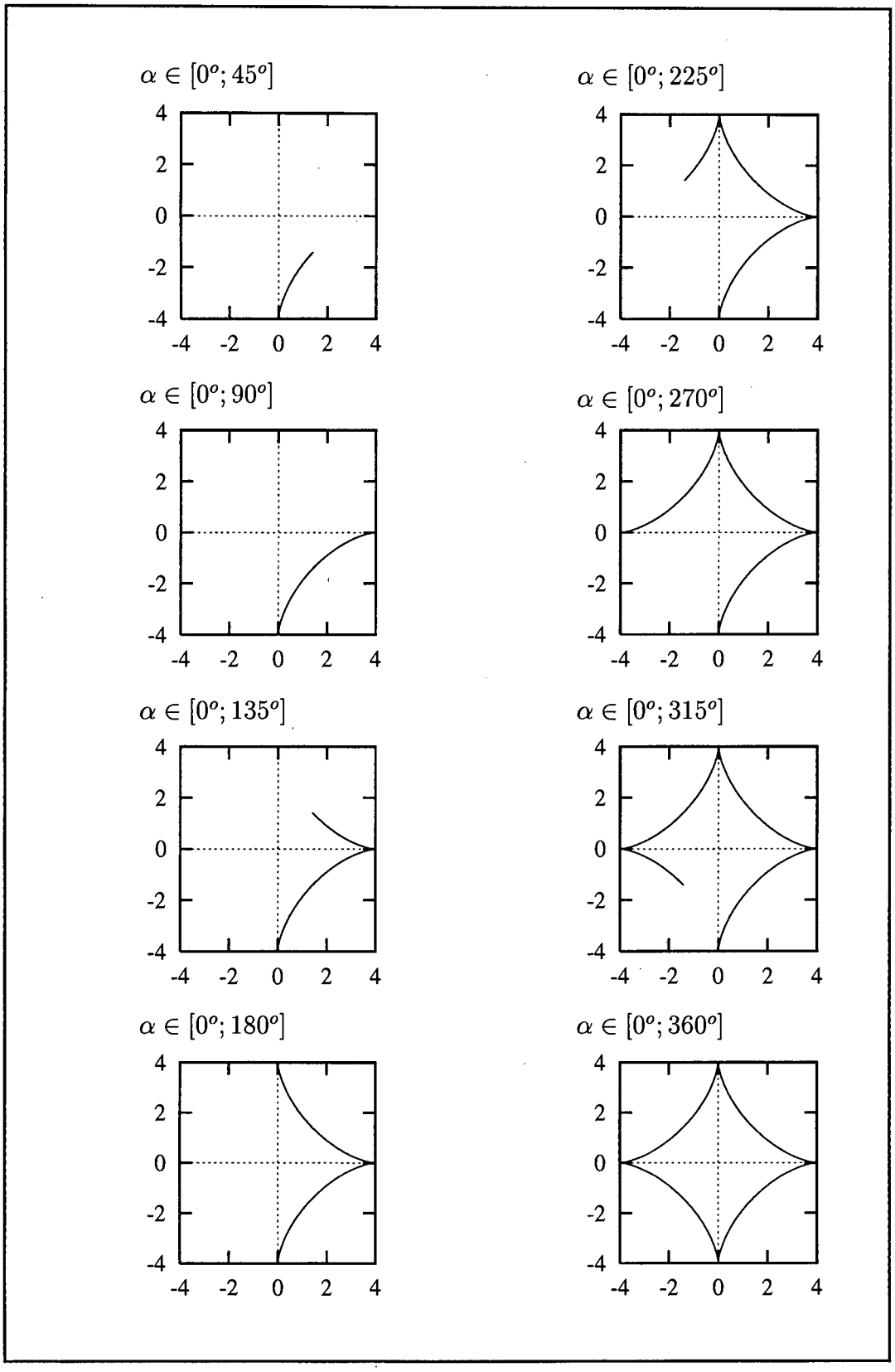

Table 6.1: Octant table for $\widehat{\mathcal{C}_R}(\alpha)$.

The time history of enhanced caustic arrivals is somewhat unexpected. A comparison between Table 6.1 and Figure 6.1 indicates that, in this scenario the earliest arrivals are at the poles, while the final arrivals

are associated with the tropical cusps.

6.6 An ATOC Example

The proposed international Acoustic Thermometry of Ocean Climate project, ATOC, focuses on the critical role of the ocean on global climate change and will measure temperature change in the ocean and, by inference, atmosphere and climate trends. The intention is to monitor the ocean on a global basis by installing acoustic sources and receivers at sites that provide adequate spatial sampling, which are technically, politically and logistically feasible. A proposed source site was installed on Pioneer Seamount during October and November 1995 (Howe 1996).

The usefulness of the antipodal algorithm is demonstrated by applying the antipodal algorithm to the existing source at the Pioneer Seamount off the west coast of California, U.S.A. The best estimate for the source is given in Howe (1996) as $37,34^{o}N$ and $123,45^{o}W$. The rays propagate southwards from the source, through the Pacific Ocean, passing New Zealand and Australia. They enter into the south eastern sector of the Southern Indian Ocean and continue to propagate westwards towards the antipodal region, which lies between the Kerguelen Island and Madagascar.

The dominant refractive assumption, using the sound slowness model determined in Section 2.2, is used to predict the antipodal region corresponding to the Pioneer Seamount source. The antipodal region is determined according to the refractive caustic curve derived above as:

$$\mathcal{C}_R(\lambda,\alpha) = [602\ 610.8\cos^2\lambda\sin^3\alpha; -602\ 610.8\cos^2\lambda\cos^3\alpha]$$

Substitution of $\lambda = 37,34^{o}$, yields an antipodal region of the form:

$$\mathcal{C}_R(\alpha) = [380913.2\sin^3\alpha; -380913.2\cos^3\alpha]$$

This curve describes a hypocycloid with an outer radius of $380\ 913,2\ m$, centered at $37,34^{o}S$ and $56,55^{o}E$, shown below in Figure 6.2.

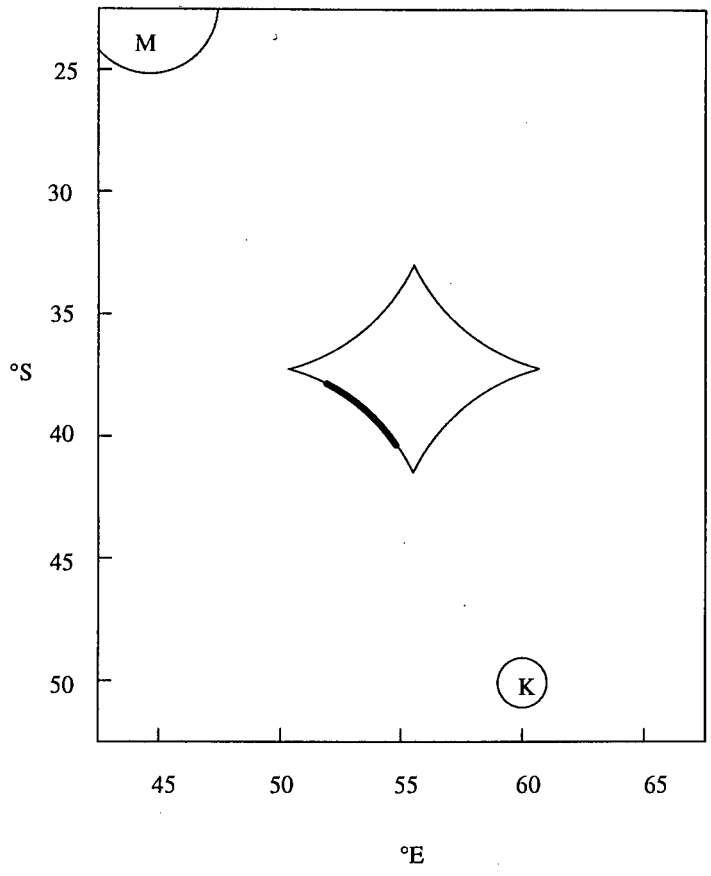

Figure 6.2: Schematic diagram of the derived antipodal region, for the Pioneer Seamount, between the islands of Kerguelen (K) and Madagascar (M).

This model result can be compared with Dworski (1993), who indicates that rays may reach this antipodal region through the relevant 'Tasman' and 'Polynesian' windows of opportunity have an azimuthal range of approximately $\alpha \in [300^o, 340^o]$. Thus the sector of the caustic curve that is reached by the 'allowable' ray tube is positioned in the south westerly sector of the antipodal region. It is thus along this section of the caustic (indicated in Figure 6.2) that enhanced receptions from the Pioneer Seamount source are expected.

In December 1995 acoustic transmissions commenced from the Pioneer Seamount Source and have continued throughout 1996 and 1997. At the time of writing this thesis there should be enhanced signals available for observation along the line of the antipodal caustic to the northwest of Kerguelen Island in the South Indian Ocean.

Bibliography

Apel, J. (1987). *Principles of Ocean Physics.* London: Academic Press Inc., pp.634.

Baggeroer, A. and W. Munk (1992, September). The Heard Island Feasibility Test. *Physics Today 45*, 22–30.

Baggeroer, A., B. Sperry, K. Lashkari, C. Chiu, J. Miller, P. Mikhalvsky, and K. von der Heydt (1994, October). Vertical Array Receptions of the Heard Island Transmissions. *Journal of the Acoustical Society of America 96*(4), 2395–2413.

Birdsall, T., K. Metzger, and M. Dzieciuch (1994, October). Signals, Signal Processing, and General Results. *JASA 96*(4), 2343–2352.

Bomford, G. (1980). *Geodesy* (fourth ed.). Oxford: Clarendon Press, pp.855.

Bryan, G., M. Truchan, and J. Ewing (1963, March). Long-Range SOFAR Studies in the South Atlantic Ocean. *JASA 35*(3), 273–278.

Do Carmo, M. (1976). *Differential Geometry of Curves and Surfaces.* U.S.A.: Prentice-Hall Inc., pp.503.

Dworski, J. (1993, October). Propagation Geometry for Pt.Sur–S.Africa ATOC Paths. Personal Communication.

Dworski, J. and J. Mercer (1990, December). Hamiltonian 3-D Ray Tracing in the Oceanic Waveguide on the Ellipsoidal Earth. Technical Report APL-UW 8929, Applied Physics Laboratory, University of Washington, Seattle.

Etter, P. (1991). *Underwater Acoustic Modeling: Principles, Techniques and Applications.* England: Elsevier, pp.305.

Ewing, M. and J. Worzel (1948, 15 October). Long-Range Sound Transmission. *Geological Society of America Memoirs 27*(111), 1–35.

Gerson, N., J. Hengen, R. Pipp, and J. Webster (1969). Radio-wave propagation to the antipode. *Canadian Journal of Physics 47*, 2143–2159.

Harrison, C. (1989). Ocean propagation models. *Applied Acoustics 27*, 163–201.

Heaney, K., W. Kuperman, and B. McDonald (1991, November). Perth-Bermuda sound propagation (1960): Adiabatic mode interpretation. *Journal of the Acoustical Society of America 90*(5), 2586–2594.

Howe, B. (1996, April). Acoustic Thermometry of Ocean Climate (ATOC): Pioneer Seamount Source Installation. Technical Report Technical Memorandum: APL-UW TM 3-96, Applied Physics Laboratory, University of Washington, Seattle, Washington.

Jensen, F., W. Kuperman, M. Porter, and H. Schmidt (1994). *Computational Ocean Acoustics.* New York: American Institute of Physics, pp.612.

Kaula, W. (1967). *The Earth in Space (Odishaw, H.(ed.))*, Chapter 13: The Earth from Space. Routledge and Kegan Paul Ltd, pp.126–135.

Koenderink, J. (1990). *Solid Shape*. U.S.A.: Massachusetts Institute of Technology, pp.699.

Lighthill, J. (1978). *Waves in Fluids*. University Press, pp.504.

Lockwood, E. (1961). *A Book of Curves*. Great Britain: Cambridge at the University Press, pp.199.

Longuet-Higgins, M. (1990). Ray paths and caustics on a slightly oblate ellipsoid. *Proceedings of the Royal Society of London 428*(A), 283–290.

Munk, W. and A. Forbes (1989, November). Global ocean warming: An acoustic measure? *Journal of Physical Oceanography 19*, 1765–1778.

Munk, W., W. O'Reilly, and J. Reid (1988, December). Australia-Bermuda sound transmission experiment (1960) revisited. *Journal of Physical Oceanography 18*, 1876–1898.

Munk, W., R. Spindel, A. Baggeroer, and T. Birdsall (1994, October). The Heard Island Feasibility Test. *Journal of the Acoustical Society of America 96*(4), 2330–2342.

Munk, W., P. Worcester, and C. Wunsch (1995). *Ocean Acoustic Tomography*. U.S.A.: Cambridge University Press, pp.433.

Munk, W. and C. Wunsch (1993, May). Ocean acoustic tomography: Rays and modes. *Review of Geophysics and Space Physics 21*(4), 777–793.

Parker, S. (Ed.) (1994). *McGraw-Hill Dictionary of Scientific and Technical Terms (International Edition)* (Fifth ed.). U.S.A.: McGraw-Hill, Inc., pp.2242.

Pearson, F. (1990). *Map Projections: theory and applications*. Florida, U.S.A.: CRC Press Inc, pp.372.

Shockley, R., J. Northrop, P. Hansen, and C. Hartdegen (1982, January). SOFAR Propagation Paths from Australia to Bermuda: Comparison of Signal Speed Algorithms and Experiments. *Journal of the Acoustical Society of America 71*(1), 51–60.

Simkin, T. and R. Fiske (1983). *Krakatau 1883 - The Volcanic Eruption and Its Effects*. Washington, D.C.: Smithsonian Institute Press, pp.332.

Spiegel, M. (1968). *Schaum's Outline Series: Mathematical Handbook of Formulas and Tables*. New York, U.S.A.: McGraw-Hill Book Company, pp.271.

Strahler, A. (1975). *Physical Geography* (4 ed.). U.S.A.: John Wiley and Sons Inc., pp.643.

Torge, T. (1980). *Geodesy*. Berlin: Walter De Gruyter & Co., pp.254.

Urick, R. (1982). *Sound Propagation in the Sea*. California: Peninsula Publishing, pp.149.